

University Mohamed Khider -Biskra

Faculty of Exact Sciences and Science
of Nature and Life

Department of Material Sciences

Ref :.....



جامعة محمد خيضر بسكرة

كلية العلوم الدقيقة وعلوم الطبيعة والحياة

قسم علوم المادة

المرجع:.....

Thesis presented for the degree of
LMD Doctorate: Physics

Speciality (Option) : Physics

Entitled
Design of a photodiode based on NiO/ZnO
heterojunction

Presented by :

Hakkoum Hadjer

Public defense on 06/03/2022

The jury composed of:

Pr. Meftah Amjad	Professor	President	Biskra University
Pr. Tibermacine Toufik	Professor	Supervisor	Biskra University
Pr. Sengouga Nouredine	Professor	Co-Supervisor	Biskra University
DR. Oussalah Slimane	Research Director	Examiner	CDTA research center Algiers
Pr. Elisabetta Comini	Professor	Examiner	Brescia University

ACKNOWLEDGEMENT

First and foremost, I would like to thank ALLAH for his helping me in making this quest for knowledge possible. Apart from my efforts, the success of this work depends largely on the encouragement and support of many others. I take this opportunity to express my gratitude to the people who have been instrumental in the successful completion of this project. Initially, I would like to acknowledge my heartfelt gratitude to my supervisors, Pr. Tibermacine Toufik and Pr. Sengouga Nourdine. Their willingness to motivate me contributed tremendously to my research work. Without their insightful guidance and persistent help, this thesis would never have been accomplished. I am thankful for the guidance, enthusiastic encouragement, valuable suggestions and useful critiques they gave me during the course of this research work.

I am grateful to the SENSOR laboratory for helping me with this project. I would like to thank Pr. Elisabetta Comini and Dr. Abderrahim Moumen for providing me with invaluable guidance and insight in developing the research and honing the analysis.

I express my sincere gratitude and appreciation to my reading committee members, Pr. Meftah Amjad, DR. Oussalah Slimane, and Pr. Elisabetta Comini for their precious time to read my thesis and for accepting to judge it.

I would like to extend my special thanks to Dr. Gougali Mabrouk and for helping me especially at the beginning of this research. Finally, my special thanks to my beloved parents, brothers and sisters for their prayers unending love, sacrifice, encouragement and support. The same goes to my friends, colleagues for their unreserved support, love, and patience towards the success of this thesis.

DEDICATION

To my dear parents, my lovely family and my friends.

Abstract

The recent interest in applications of ultraviolet photodiodes based on Nickel Oxide/ Zinc Oxide (NiO/ZnO) heterojunction heightens the need for more developments. One of the greatest challenges was to indicate which factors control the performance of these devices. Therefore, this research is based on three studies. In the first study, we managed to get the effect of the source solution quantity on structural and optical characteristics of ZnO and NiO thin films grown by spray pyrolysis for the design of NiO/ ZnO photodiodes. We assumed that increasing the film thickness reduces the defects and results in less recombination through higher crystallinity which enhances the photodetection. In the second study, we fabricated a NiO/ZnO junction by spray pyrolysis with optimum conditions. We performed a simulation to clarify the effects of heterojunction behavior and interface trap on the performance of NiO/ZnO photodiodes. The origin of current has been attributed to the tunneling, thermionic emission in the interface and due interface traps SRH generation and recombination controlling the carrier transport at the heterojunction. As a third study, the radio frequency sputtering technique was used to deposit NiO and ZnO thin films to form NiO/ZnO heterojunction in oxygen flow absence conditions. We found that the NiO/ZnO heterojunction has a semi-transparency in the visible range which makes this heterojunction suitable for broadband photodetection applications. This study demonstrates that NiO/ZnO heterojunction could play an important role in many applications such as broadband photodetection (ultraviolet and visible ranges), partial transparent optoelectronic devices and solar cells. These studies imply that using the crystal structure as desired has always been the key to designing and targeting high-quality heterojunctions. These results have allowed us to identify key parameters useful for the optimization of NiO/ZnO photodiodes, as well as to give realistic estimates of the performances of such UV devices.

Résumé

L'intérêt récent pour les applications des photodiodes ultraviolettes basées sur l'hétérojonction oxyde de nickel/oxyde de zinc (NiO/ZnO) renforce le besoin de développements supplémentaires. L'un des plus grands défis était d'indiquer quels facteurs contrôlaient les performances de ces dispositifs. Par conséquent, cette recherche a été établie et basée sur trois études. Dans la première étude, nous avons réussi à obtenir l'effet de la quantité de solution sur les caractéristiques structurales et optiques des couches minces de ZnO et NiO déposées par le procédé pyrolyse de pulvérisation pour la conception de photodiodes NiO/ZnO. Nous avons supposé que l'augmentation de l'épaisseur de couche réduit les défauts et entraîne moins de recombinaison grâce à une cristallinité plus élevée, ce qui améliore la photodétection. Dans la deuxième étude, nous avons fabriqué une jonction NiO/ZnO par pyrolyse en spray dans des conditions optimales. Nous avons effectué une simulation pour clarifier les effets du comportement de l'hétérojonction et du piège d'interface sur les performances des photodiodes NiO/ZnO. L'origine du courant a été attribuée à l'effet tunnel, à l'émission thermoionique dans l'interface et aux pièges d'interface causant la génération/recombinaison de Shockley-Read-Hall qui contrôle le transport des porteurs à l'hétérojonction. Dans une troisième étude, la technique de pulvérisation par radiofréquence a été utilisée pour déposer des couches minces de NiO et de ZnO afin de former une hétérojonction NiO/ZnO dans des conditions d'absence de flux d'oxygène. Nous avons constaté que l'hétérojonction NiO/ZnO présente une semi-transparence dans le domaine visible, ce qui la rend adaptée aux applications de photodétection à large bande. Cette étude démontre que l'hétérojonction NiO/ZnO pourrait jouer un rôle important dans de nombreuses applications telles que la photodétection à large bande (ultraviolet et visible), les dispositifs optoélectroniques partiellement transparents et les cellules solaires. Ces études impliquent que l'utilisation de la structure cristalline comme souhaitée a toujours été la clé pour concevoir et cibler des hétérojonctions de haute qualité. Ces résultats nous ont permis d'identifier les paramètres clés utiles à l'optimisation des photodiodes NiO/ZnO, ainsi que de donner des estimations réalistes des performances de ces dispositifs.

الملخص

الأهمية المولدة مؤخرًا لتطبيقات الكاشف الضوئي للأشعة فوق البنفسجية القائم على الوصلة غير المتجانسة بين أكسيد النيكل وأكسيد الزنك يزيد من الحاجة إلى مزيد من تطوير هذه الأجهزة. من أكبر التحديات هو تحديد العوامل التي تتحكم في أداء هذه الكواشف ولذلك اعتمد هذا البحث على ثلاث دراسات. في الدراسة الأولى تمكنا من مناقشة مدى تأثير كمية المحلول خلال توضع أكسيد النيكل و أكسيد الزنك على الخصائص البنيوية و الضوئية لهذه الأغشية الرقيقة باستعمال تقنية رذاذ الانحلال الحراري لتصميم الكاشف الضوئي. كما بينا أن زيادة سمك الأغشية يقلل من العيوب ويقلل من إعادة التركيب من خلال زيادة التبلور مما يحسن من خصائص الجهاز. في الدراسة الثانية و باستعمال نفس التقنية تم تصنيع الوصلة من أكسيد النيكل وأكسيد الزنك. أجرينا محاكاة لتوضيح تأثيرات سلوك الوصلة غير المتجانسة ومصيدة الواجهة على أداء الكاشف الضوئي. لقد وجدنا أن أصل التيار في غياب الضوء يعود إلى كل من آلية النفق والانبعاث الحراري في الواجهة، في حين أن مصائد الواجهة التي يسببها عدم التطابق تؤدي إلى تحكم في نقل عند الواجهة أيضا عن طريق توليد وإعادة تركيب الحاملات. يمكن أن تساهم هذه النتائج في فهم أعمق لآليات النقل في هذه الكواشف الضوئية. كدراسة ثالثة، تم استخدام تقنية تردد الراديو الأخرق لتصنيع أغشية رقيقة من أكسيد النيكل و أكسيد الزنك في حالة عدم تدفق الأكسجين. تبين أن الوصلة الغير المتجانسة تتميز بشفافية جزئية مما يجعلها مناسبة لتطبيقات الكاشف الضوئي ذات النطاق العريض أي للنطاق المرئي وفوق البنفسجي. توضح هذه الدراسة أن الوصلة أكسيد النيكل وأكسيد الزنك الغير المتجانسة يمكن أن تلعب دورًا مهمًا في العديد من التطبيقات مثل الكاشف الضوئي للنطاق العريض والأجهزة الإلكترونية الضوئية جزئية الشفافية والخلايا الشمسية. تشير هذه الدراسات إلى أن الحصول على البنية البلورية الحيدة للمواد كان دائمًا هو المفتاح لتصميم واستهداف وصلات غير متجانسة عالية الجودة. سمحت لنا هذه النتائج بتحديد المعاملات الرئيسية المفيدة لتحسين الكواشف الضوئية وكذلك لإعطاء تقديرات واقعية لأدائها.

CONTENTS

Acknowledgement	ii
Dedication	iii
Abstract	iv
Résumé	v
ملخص	vi
List of Figures	xi
List of Tables	xv
INTRODUCTION	1
1 An overview of Nickel oxide and Zinc oxide	5
1.1 Introduction	6
1.2 Presentation of TCOs studied	6
1.3 Nickel oxide thin film	7
1.3.1 NiO properties	7
1.3.1.1 Structural properties	8
1.3.1.2 Optical properties	8
1.3.2 Doping of NiO	10
1.4 Zinc oxide thin film	11
1.4.1 ZnO properties	11
1.4.1.1 Structural properties	11
1.4.1.2 Optical properties	12
1.4.2 Doping of ZnO	13

2	Fundamentals of photodiode	15
2.1	Introduction	16
2.2	History of photodiode	16
2.3	Photodiode operation principle	18
2.4	Types of photodiode	18
2.4.1	PN junction photodiode	19
2.4.2	PIN junction photodiode	19
2.4.3	Schottky photodiode	20
2.4.4	Avalanche photodiode	21
2.5	Characteristics of photodiode	21
2.5.1	Current versus Voltage Characteristics	21
2.5.2	Quantum efficiency	23
2.5.3	Responsivity	23
2.5.4	Spectral Response	24
2.5.5	Response Time	24
2.6	Application of photodiode	25
3	NiO/ZnO Heterojunction Photodiode	26
3.1	Introduction	27
3.2	Heterojunction types	27
3.3	NiO/ZnO band diagram	28
3.4	Application of NiO/ZnO heterojunctions	30
3.5	Review of NiO/ZnO heterojunction photodiodes	31
4	Experimental Details	39
4.1	Introduction	40
4.2	Deposition Techniques	40
4.2.1	Spray pyrolysis	40
4.2.2	Sputtering	43
4.3	Characterization techniques	45
4.3.1	Raman Spectroscopy	45
4.3.2	X-ray diffraction	46
4.3.3	Scanning Electron Microscope	47
4.3.4	UV-VIS spectroscopy	48

5	Simulation details	50
5.1	Introduction	51
5.2	ATLAS commands	51
5.3	Model description	52
5.3.1	Basic carrier transport equations	52
5.3.2	Carrier recombination	53
5.3.3	Thermionic emission and tunneling transport models	56
5.4	Carrier generation	56
5.5	Design process of NiO/ZnO heterojunction photodiode	57
6	Results and discussion	58
6.1	Introduction	59
6.2	Effect of the source solution quantity on ZnO and NiO thin films	59
6.2.1	Structural properties of NiO and ZnO thin films	60
6.2.2	Optical properties	62
6.2.2.1	Transmittance	62
6.2.2.2	Reflectance	62
6.2.2.3	Absorption coefficient	63
6.2.2.4	Extraction of optical bandgap	64
6.2.2.5	Refractive Index and Extinction coefficient	65
6.3	Effect of material properties on design of a NiO/ZnO heterojunction photodiode	67
6.3.1	Device structure	67
6.3.2	Electrical characteristics	68
6.3.3	Optical response characteristics	69
6.3.4	Simulation of the effects of ZnO and NiO defects on the performance of NiO/ ZnO photodetectors	71
6.3.4.1	Defects in NiO bulk	72
6.3.4.2	Defects in ZnO bulk	74
6.4	NiO/ZnO heterojunction fabrication and characterization	75
6.4.1	Structural properties	76
6.4.2	Optical properties	77
6.4.3	Morphology properties	78
6.5	Study of NiO/ZnO heterojunction interface	79
6.5.1	NiO/ZnO heterojunction behavior	80

6.5.2	Modeling J-V characteristics of the photodiode	83
6.5.2.1	Photocurrent modeling	84
6.5.3	Modeling of the interface traps parameters effect	85
6.5.3.1	Trap density	85
6.5.3.2	Electron cross-section	88
6.5.3.3	Acceptor trap density	89
6.5.3.4	Donor trap density	91
6.6	Semi-transparent NiO/ZnO heterojunction growth and characterization	93
6.6.1	Structural properties	93
6.6.2	Morphology properties	95
6.6.3	Optical properties	96
6.6.4	Influence of oxygen flow on optical properties of NiO thin film	97
6.7	Discussion	100
	Conclusion	106
	Bibliography	110
	A Publications and Conferences	122

LIST OF FIGURES

1.1	Crystal structure of NiO.	8
1.2	Formation energy for anion and cation vacancies in NiO. Solid lines represent formation energy of the lowest-energy charged state of vacancy at O-rich (Ni-poor) conditions whereas dashed lines are for O-poor (Ni-rich) conditions (Zhang et al., 2008).	9
1.3	Hexagonal crystal structure of ZnO (Samanta et al., 2011).	12
1.4	Schematics of energy levels for ZnO (the figure is redrawn from (Shimada et al., 2012)).	13
2.1	Definition of the operation of a photodiode.	18
2.2	Device structure of the p-n junction photodetector.	19
2.3	Schematic drawings of a PIN photodiode.	20
2.4	Schematic drawings of in a Schottky photodiode, light is absorbed in the depletion region of an n-type semiconductor after passing through a semitransparent metallic film (Quimby, 2006).	20
2.5	Photograph of 3 mm and 5 mm APDs. Cross-section of an ITE APD structure (Campbell, 2016).	21
2.6	Characteristic I-V curve of a photodiode in linear and logarithmic scale.	22
2.7	Spectral responsivity characteristics of UV photodetectors.	24
3.1	Schematic energy band diagram of three types of semiconductor heterojunctions.	28
3.2	Energy-band diagram for p-NiO/n-ZnO heterojunction under zero bias (Jlassi et al., 2014).	29
3.3	Schematic diagram of the device structure (Shen et al., 2015).	31
3.4	J-V characteristics of NiO/ZnO bipolar heterostructure (Grundmann et al., 2014).	32
3.5	Schematic and illustration of the developed transparent NiO/ZnO heterojunction UV photodetector (Patel et al., 2015).	33
3.6	Current–density voltage relations of a ZnO/eclipse-NiO heterojunction under dark and UV illumination for different intensities (Karsthof et al., 2016).	34
3.7	Measured I-V characteristics of samples (Mohammadi et al., 2017).	35

3.8	The structures and energy band diagrams of NiO/ZnO (a) before and (b) after contact (Wei et al., 2020).	37
4.1	Schematic sketch of the chemical spray pyrolysis process.	42
4.2	Scheme of major advantages of spray pyrolysis techniques for thin film deposition.	42
4.3	Schematic diagram of the sputtering chamber (Schuler, 2008).	43
4.4	Sputtering is used in this work.	43
4.5	Sputtering detailed which used in this work.	44
4.6	Schematic showing how the sputtering deposition works.	44
4.7	RAMAN -characterization technique.	46
4.8	XRD -characterization technique.	47
4.9	SEM -characterization technique	48
4.10	UV-VIS -characterization technique.	49
5.1	ATLAS command groups.	52
5.2	Schematic recombination transition.	55
6.1	The preparation procedure of NiO thin films by spray pyrolysis deposition.	60
6.2	XRD patterns of (a) NiO and (b) ZnO thin films using different quantities of solution.	61
6.3	Transmittance spectra of (a) NiO and (b) ZnO thin films at different quantities of solution.	62
6.4	Reflectance spectra of deposited (a) NiO and (b) ZnO thin films for different quantities of solution.	63
6.5	Absorption coefficient of deposited (a) NiO and (b) ZnO thin films for different quantities of solution.	64
6.6	Variation of $(\alpha h\nu)^2$ versus photon energy of deposited (a) NiO and (b) ZnO thin film for different quantities of solution showing the extracted energy gap.	65
6.7	The extracted optical parameters of NiO and ZnO, (a) and (b) refractive index (n) and (c) and (d) extinction coefficient (k) for different quantities of solution.	66
6.8	Simulated NiO/ZnO heterojunction photodiode structure.	67
6.9	Dark and light I–V characteristics of NiO/ZnO heterojunction photodiode for different solutions of (a) NiO, (b) ZnO, and (c) NiO and ZnO together.	68
6.10	Responsivity of NiO/ZnO heterojunction photodiode for different quantities of solution of (a) NiO, (b) ZnO and (c) that of NiO and ZnO together.	69

6.11	Acceptor and donor Tail States and Gaussian Distributions function energy for (a) NiO and (b)ZnO.	71
6.12	(a) Dark current and photocurrent and (b) Responsivity of the NiO/ZnO heterojunction under different tail densities in NiO bulk.	72
6.13	(a) Dark current and photocurrent and (b) Responsivity of the NiO/ZnO heterojunction under different Gaussian densities in NiO bulk.	73
6.14	(a) J-V characteristics and (b) Responsivity of the NiO/ZnO photodiode under different ZnO tail defects.	74
6.15	(a) J-V characteristics and (b) Responsivity of the NiO/ZnO photodiode under different ZnO gaussian defects.	75
6.16	Fabrication process of NiO/ZnO heterojunction deposited by spray pyrolysis.	75
6.17	XRD patterns of NiO/ZnO heterostructure.	76
6.18	Raman spectra of NiO/ZnO heterostructure.	76
6.19	Transmittance spectra of ZnO, NiO thin films and ZnO/NiO heterojunction.	77
6.20	SEM images of (a) and (b) ZnO thin films with different magnifications. (c) and (d) NiO with different magnifications and (e), (f) and (g) Cross-sectional visualizing the NiO/ZnO heterostructure with different magnifications.	78
6.21	NiO/ZnO heterojunction photodiode structure.	80
6.22	Energy band diagram of the NiO/ZnO heterojunction before contact.	80
6.23	band levels at the external bias of 1.1V.	81
6.24	Simulated potential of the NiO/ZnO heterojunction under different applied voltages.	82
6.25	Simulated electric field of the NiO/ZnO heterojunction.	82
6.26	(a) Energy band diagram (b) Potential of the NiO/ZnO heterojunction without and with using tunneling model (c) Dark current considering the contributions of SRH, thermionic emission and band to band tunneling under reverse bias. (d) J-V characteristics for NiO/ZnO heterojunction photodiode.	83
6.27	(a) Photogeneration rate (b) Photon absorption rate at the NiO/ZnO heterojunction photodiode.	85
6.28	(a) Simulated energy band diagram and (b) Simulated potential of the NiO/ZnO heterojunction under different interface trap density (-0.5V).	86
6.29	(a) Trap recombination rate (-0.5V), (b) Dark current, (c) Photocurrent and (d) Responsivity of the NiO/ZnO heterojunction under different interface trap density.	87
6.30	(a) Dark current,(b) Responsivity, (c) Photocurrent of the NiO/ZnO heterojunction under different electron capture cross-sections of interface traps.	88

6.31	(a) Band diagram (-0.5V), (b) J-V dark, (c) J-V light characteristics and (d) Responsivity of the designed NiO/ZnO photodiode under different acceptor interface trap density.	90
6.32	(a) Band diagram (-0.5V), (b) Dark current, (c) Photocurrent and (d) Responsivity of the NiO/ZnO heterojunction under different donor interface trap density.	91
6.33	XRD spectra of (a) NiO (b) ZnO thin film and (c) NiO/ZnO heterojunction.	94
6.34	SEM images of (a) and (b) NiO thin films with different magnifications. (c) and (d) ZnO with different magnifications and (e), (f) (g) Cross-sectional visualizing the NiO/ZnO heterostructure with different magnifications.	95
6.35	(a) Optical transmittances and (b) absorbance spectra of NiO, ZnO thin films, and NiO/ZnO heterojunction.	96
6.36	(a) Absorption coefficient (α) (b) $(\alpha h\nu)^2$ and energy $h\nu$ (c) The extracted refractive index and (d) the extinction coefficient of NiO and ZnO films deposited by RF sputtering.	97
6.37	Transmittance spectra of NiO thin films at different oxygen flow.	98

LIST OF TABLES

1.1	Fundamental physical properties of some important metal-oxides.	6
1.2	The basic properties of nickel oxide (Khan, 2016; Soleimanpour, 2013).	7
1.3	Comparison of different elements used for doping NiO.	10
1.4	The basic properties of Zinc Oxide (Khan, 2016; Chu, 2011).	11
1.5	Comparison of different elements and methods used for doping ZnO.	14
2.1	History of photodiode developments (Renker, 2006).	16
2.2	New type of advanced photodiode (Zou et al., 2018; Husain et al., 2018).	17
3.1	Review most common previous works which focus on the development of UV photodetectors based on metal oxides materials.	38
4.1	Various stages of nucleation and growth of thin films Jilani et al. (2017).	41
5.1	Simulators of ATLAS are used for simulation.	52
5.2	Basic steps to design a NiO/ZnO heterojunction photodiode with the simulator ATLAS.	57
6.1	Spray pyrolysis deposition conditions for the preparation of NiO and ZnO thin films.	60
6.2	Microstructural parameters of NiO and ZnO thin films.	62
6.3	The thickness as a function of quantities of solution for NiO and ZnO thin films	64
6.4	Basic structure design parameters (Elseman et al., 2018; Chala et al., 2018).	67
6.5	Comparative responsivity of different structures to NiO/ZnO heterostructure photodiode.	70
6.6	The parameters of the DOS used to simulate the NiO and ZnO bulk of the NiO/ZnO photodiode (Elseman et al., 2018; Chala et al., 2018).	72
6.7	Comparative values for the valence and conduction band offsets for NiO/ZnO heterojunction.	81
6.8	The light and dark current constitution under reverse bias 0.8V.	84
6.9	Extracted parameters were used to describe carrier transport mechanisms at the NiO/ZnO interface under different interface trap densities (-0.5V).	86

6.10 Extracted parameters were used to describe carrier transport mechanisms at the NiO/ZnO interface under different electron capture cross-sections of interface traps (-0.5V). 89

6.11 Extracted parameters were used to describe carrier transport mechanisms at the NiO/ZnO interface under different acceptor interface trap densities (-0.5V). 89

6.12 Extracted parameters were used to describe carrier transport mechanisms at the NiO/ZnO interface under different donor interface trap densities (-0.5V). 92

6.13 The experimental conditions for deposition of NiO/ZnO thin films. 93

6.14 Crystallite size, dislocation density and microstrain of NiO and ZnO thin films extracted from XRD analysis. 93

6.15 Comparative studies of the experimental results of NiO with previous findings. 99

INTRODUCTION

INTRODUCTION

It can be argued that modern research and technology development should go on new ultraviolet (UV) protection devices products or improvements on these devices. The amount of UV radiation received at Earth's surface has important implications for human health (Armstrong et al., 2017).

Much has been learned and many advancements have been made in UV devices, especially dealing with electronics and semiconductor devices. However, recently, UV protection research has more attention, Especially UV photodiodes, UV LEDs and UV solar panels. UV photodiodes can be designed by combining p- and n-type layers to form p-n junctions. A conducting anode, a semiconductor p-n junction, and a conducting cathode achieve rectifying current-voltage characteristics (Yu et al., 2016). The most common materials in this research are wide bandgap materials to detect UV radiation. Metal oxides (MOs) are the most abundant materials in the Earth's crust and are ingredients in traditional ceramics. Researchers continuing to flesh out materials principles that have yet to be understood in totality. Recently, zinc oxide (ZnO) has attracted a great deal of attention due to its wide direct band gap (3.37 eV) and relatively large exciton binding energy (60 meV), and because of these unique properties, ZnO has been recognized as a promising material for optoelectronic devices (Echresh et al., 2014). Nickel oxide (NiO) has attracted widespread attention due to its diverse range of applications, e.g., in catalysis, battery cathodes, gas sensors, electrochromic films, and magnetic materials Arfan et al. (2018). From these points, the research looked at how compatible these two materials are to form NiO/ZnO heterojunction and especially for design a UV photodiode.

Low-cost NiO/ZnO devices are getting thinner and larger for better performance in terms of responsivity, and high operation along with the technological developments. These devices have gained much attention due to the demand from the research to have faster and more responsive devices for vast applications. The downside of this heterojunction photodiode based on NiO and ZnO materials, however, is the reduction of the UV absorption for photodiodes, comparing to a conventional device. Furthermore, the interface alignment has limited the photodetection process (Fallahpour et al., 2017). All these points return on how accurate is of the design process. The key photodiode parameters such as photo/dark current are related to the complex relationship between light absorption, charge

transport, and free-carrier losses and extraction. Such physical processes are still under debate depending on the material structure and the morphology of the bulk-heterojunction, and the operation mode/condition of the device .

Several studies on fabrication and characterization of NiO/ZnO heterojunction photodiodes using different deposition techniques have been reported (Klochko et al., 2018; Hasan et al., 2015; Echresh et al., 2015; Patel et al., 2017). But still, the performance with different parameter variations needs to be studied and analyzed. It is desirable to study the electrical and optical properties of NiO/ZnO heterojunction photodiode before their adoption in the fabrication of micro/nanoscale optoelectronics.

Our work presents a qualitative study to identify the most important reasons for the degradation in device operation. Where emphasis was placed on answering the extent to which material properties and heterojunction design affect NiO/ZnO photodiode performance. First, we studied the effect of source solution quantity (5, 10 and 15 ml) on structural and optical characteristics of ZnO and NiO thin films growth by spray pyrolysis for the design of NiO/ZnO photodetectors. We performed numerical simulation with the use of SILVACO ATLAS software to simulate the device variation different NiO and ZnO parameters and defects values. The second study, we have fabricated the NiO/ZnO heterojunction with 15 ml quantity of solution conditions. Structural, morphological and optical characterizations are investigated. The extracted experimental parameters are used for the design and modeling of NiO/ZnO heterojunction photodiode to obtain information about the device behavior, dark current transport mechanism and how traps controlling the quality of the device. Analysis of the structure design and the interface between its components are expected to have a dominant role in photodetector optimization. As a third study, we have prepared NiO, ZnO, NiO/ZnO heterojunction by using radio frequency sputtering method under vacuum (0 % oxygen flow). Structural, morphological and optical properties are analysed.

To facilitate understanding of these objectives, the thesis is organized as follows: We give a brief theoretical background in chapter 1. An overview of thin films and transparent conduction oxides is provided. Then, the basic properties of NiO and ZnO thin films and their applications are presented. In chapter 2, we continue the brief theoretical background with the basic semiconductor physics and the principles of the PN photodiodes are covered. In chapter 3, we present an overview of the NiO/ZnO heterojunction interface first, then a review of NiO/ZnO photodiodes. The experimental techniques (for deposition thin films spray pyrolysis and RF sputtering besides characterization machines) are provided in chapter 4. Concerning simulation tools we present Silvaco TCAD for design

and characterization of the photodiode in chapter 5. We present our results on design of UV NiO/ZnO photodetector in chapter 6. Finally, we give our final remarks and possible future directions of this study in conclusion.

CHAPTER 1

AN OVERVIEW OF NICKEL OXIDE AND ZINC OXIDE

1.1 Introduction

The field of material science and the engineering community's ability to conceive novel materials with an extraordinary combination of chemical, physical and mechanical properties has changed modern society. There is increasing technological progress. Modern technology requires thin films for different applications (AL-Rashdi et al., 2016). In this chapter, an overview of thin films, transparent conduction oxides are provided. Then, the basic properties of NiO and ZnO thin films and their dopants are presented.

1.2 Presentation of TCOs studied

Metal oxides are very attractive materials for the fabrication of gas sensors (Galstyan et al., 2019), photodetector (Patel et al., 2017) solar cells Chala et al. (2018), Diodes (Huang et al., 2013a), due to their ability to interact with different gaseous compounds. Several metal oxides have been studied like ZnO (Khan et al., 2017), NiO (Patel et al., 2017), SnO_2 (Patil et al., 2012), Cu_2O (Choudhary et al., 2016), $\beta - Ga_2O_3$ (Hao et al., 2019), CdO (Vadgama et al., 2017) , and TiO_2 (Rao et al., 2014). Table 1.1 presented an overview of some metal oxide properties.

Table 1.1: Fundamental physical properties of some important metal-oxides.

Metal oxide	Structure	Type	Bandgap (eV)	Sensing light	Ref
NiO	Cubic	P	3.6	UV	(Patel et al., 2017)
ZnO	Hexagonal	N	3.37	UV	(Khan et al., 2017)
SnO_2	Tetragonal	N	3.6	UV	(Patil et al., 2012)
Cu_2O	Cubic	P	2.1	Visible	(Choudhary et al., 2016)
$\beta - Ga_2O_3$	Monoclinic	N	4.9	UV	(Hao et al., 2019)
$\alpha - Fe_2O_3$	Rhombohedral	N	2.1	Visible	(Farahmandjou et al., 2015)
In_2O_3	Cubic	N	3.2	UV	(Nagaraju et al., 2014)
CdO	Cubic	N	2.2 (direct) 1.36(indirect)	Visible/IR	(Vadgama et al., 2017)
CeO_2	Cubic	N	3.2	UV	(Phokha et al., 2012)
TiO_2	Monoclinic	N	3.2	UV	(Rao et al., 2014)

1.3 Nickel oxide thin film

The prospects for using wide-bandgap materials in a number of applications are being widely researched today across multiple domains such as biology, physics, chemistry, cosmetics, optical components, pharmaceutical drug manufacture, polymer science, mechanical engineering, and toxicology. In recent years, wide bandgap materials have received steadily growing attention as a result of their peculiar and fascinating properties and applications. Among the various nano-materials, metal oxides (with NiO inclusive) have attracted increasing technological and industrial interest. This interest has mainly to do with their properties (optical, magnetic, electrical, and catalytic properties) associated with general characteristics such as mechanical hardness, thermal stability, or chemical passivity. Nickel oxide is a prominent example of metal oxides.

1.3.1 NiO properties

The structural, electrical, optical and thermal properties of the material are often important when material selection and processing decisions are being made during the design of a device. As shown in Table 1.2 the basic properties clarify the identity of NiO.

Table 1.2: The basic properties of nickel oxide (Khan, 2016; Soleimanpour, 2013).

Type of properties	Items	NiO
Physical properties	Density	6.97 g /cm ³
	Molar mass	74.69 g/mol
Optical properties	Bandgap	2-4.3 eV
	Refractive index (n)	2.18
Electrical properties	Resistance	10 ⁹ – 10 ¹¹ Ω.cm
	Dielectric constant	10
	Carrier type (undoped)	p-type
Thermal properties	Thermal conductivity	~5 W/m K
	Melting point	1957 °C
Descriptive Properties	Color	green
	Crystal Structure	cubic /rock sal structure

1.3.1.1 Structural properties

NiO adopts the NaCl structure, with octahedral Ni(II) and O^{-2} sites as shown in Figure 1.1 from (Magyari-Köpe et al., 2012). The conceptually simple structure is commonly known as the rock salt structure. Like many other binary metal oxides, NiO is often non-stoichiometric. In nickel oxide, this non-stoichiometry is accompanied by a color change, with the stoichiometrically correct NiO being green and the non-stoichiometric NiO being black (Patnaik, 2003).

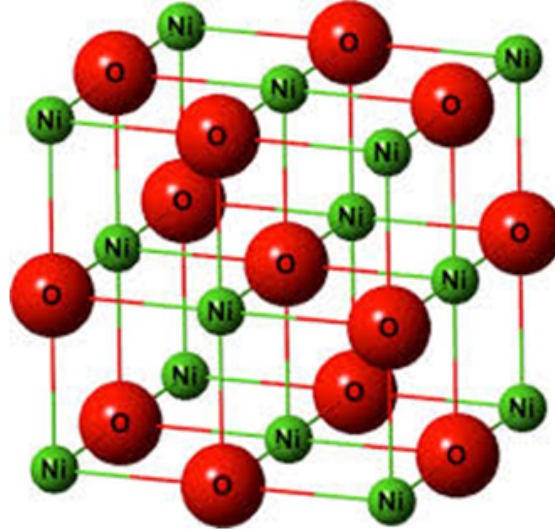


Figure 1.1: Crystal structure of NiO.

1.3.1.2 Optical properties

The material nickel oxide from the transparent conductive oxides (TCO) which have high conductivity and lighting gap energy directly. The bandgap of NiO thin films changes with the deposition technique in between 3.6 and 4 eV. Nickel(II) oxide has a bandgap of around 3.7 eV, depending on the preparation conditions of the sample which makes it suitable for visibly transparent applications. Pure, stoichiometric NiO is a Mott insulator, but in the presence of excess oxygen during growth it possesses the tendency to form a high concentration of nickel vacancies due to the low formation energy of V_{Ni} under these conditions. In a perfect NiO crystal with a rocksalt structure, the Ni ions occupy octahedrally coordinated lattice sites and exhibit a valency of 2. Upon the formation of a Ni vacancy, two holes are released that transform two nearby Ni^{2+} into Ni^{3+} . This leads to a local distortion of the lattice (formation of small polarons). For this reason, the holes are localized, and conduction can only take place by means of a thermally activated hopping process which is the reason for low hole mobility. The presence of Ni^{3+} ions also leads to a reduced transmittance of metal-deficient NiO films in the visible range, since these ions act as color centers (Ghoughali, 2019). The

Ni vacancy forms a shallow acceptor, suggesting the native p-type conductivity originates from the cation vacancy. In addition, after introducing a Ni vacancy, a half-metallic antiferromagnet or half-metallic ferromagnet can form according to the different ionization states of cation vacancy (Zhang et al., 2008). Figure 1.2 shows formation energies of vacancies in NiO as a function of the Fermi level under O-poor and O-rich conditions. Only the lowest-energy charged state of different vacancies at given E_f is shown. Because NiO belongs to densely packed structures, the formation energies of interstitials are rather high and this kind of interstitial is difficult to form spontaneously.

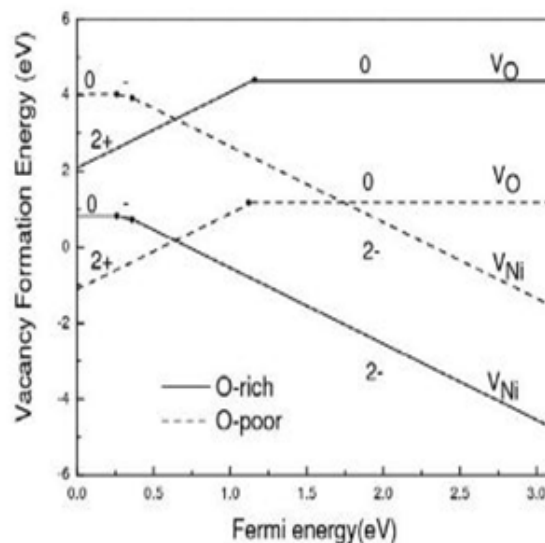


Figure 1.2: Formation energy for anion and cation vacancies in NiO. Solid lines represent formation energy of the lowest-energy charged state of vacancy at O-rich (Ni-poor) conditions whereas dashed lines are for O-poor (Ni-rich) conditions (Zhang et al., 2008).

The formation energy of the neutral O interstitial is 8.68 eV under O-poor conditions, compared with the neutral nickel and oxygen vacancy of 4.03 eV and 1.17 eV. Under O-rich growth conditions, the Ni vacancies are found to be the predominant defect and the stable charged state of Ni vacancies varies with different Fermi energy. When E_f is near conduction-band minimum (CBM), the most stable defects are V_{Ni}^{2-} in a wide range of E_f . V_{Ni}^0 , V_{Ni}^- are the stable defect states for $E_f \leq E_v + 0.26 eV$ and $E_f \leq E_v + 0.37 eV$, respectively. In contrast, under O-poor conditions, with different Fermi energy, the V_{Ni}^{2-} , V_O^0 , V_O^{+2} are most stable vacancy defects in the corresponding energy region. The influence of O_2 partial pressure and temperature is believed to have a very important role in the stability of defect structure.

1.3.2 Doping of NiO

Doping in metal oxide materials is the result of the addition of the dopant atom sites in place of one of the constituent atoms in the bulk, In p-type doping, the dopant atom causes an electronic deficiency in the ionic bonding, thus creating an empty acceptor energy level just above the valence band, which can accept an electron from that valence band, and leaves behind a positive (hole). This allows conduction via doping species to a bulk semiconducting or insulating lattice structure. Extrinsic doping is done by changing the original ions Ni^{2+} or oxygen ions O^{2-} (anions) with ions having respectively a higher or lower valence, the charge carriers concentration can be increased. This increase leads to shifting in the Fermi level within the conduction band, if the opposite occurs, the Fermi level shifting within the valence band (Ghougali, 2019). The introduction of impurities into the crystal lattice creates energy levels in the gap and either donors or acceptors, which are responsible for changing the optical and electrical properties. Table 1.3 shows some elements that can be used for NiO doping.

Table 1.3: Comparison of different elements used for doping NiO.

Element	Chemical formula	Doping content	Temperature	Methods	Application	Ref
Li	Li_xNiO_{1-x}	x = 0, 0.006, 0.03, 0.06, 0.09	500 °C	Pulsed laser deposition	Hole transport layer	(Zhang et al., 2018) (Firat
Cu	Cu:NiO	from 9 % to 18 %	300 °C	Electrode position process	Electrochromic applications	and Peksoz, 2019)
Zn	Zn- NiO	10% and 20 %	-	Hydrothermal route	Electrochemical water splitting applications	(Rani et al., 2019) (Mrabet
La	LaNiO3 (LNO)	0%, 1%, 2%, 3% and 4%	450 °C	Spray pyrolysis	Optoelectronic and sensor applications	et al., 2016) (Hu
Y	Y-NiO	3%,5%, 7%, and 10%	500 °C	Sol-gel	HTL-based PSC devices outperformed	et al., 2018)

1.4 Zinc oxide thin film

In recent years, there is a large volume of published studies describing the ZnO material properties and applications such as in pharmaceutical, cosmetic, food, rubber, commodity chemical, painting, ceramic, and glass industries. However, all the previous ZnO research was central in material design and characterization, most researchers investigating ZnO have focused on the role of the material in several applications and how affects the material growth on the device design.

1.4.1 ZnO properties

Table 1.4 presented an overview of The structural, electrical, optical, thermal and descriptive properties of the ZnO material.

Table 1.4: The basic properties of Zinc Oxide (Khan, 2016; Chu, 2011).

Type of properties	Items	ZnO
Physical properties	Density	5.606 g/cm ³
	(a) lattice constant	0.32469 Å°
	(c) lattice constant	0.52069 Å°
	Molar mass	81.4084 g/mol
Optical properties	Bandgap	3.2-3.3 eV
	Refractive index (n)	2-2.5
Electrical properties	Dielectric constant	9
	Hole Mobility	5-50 cm ² /V.s
	Carrier type (undoped)	n-type
Thermal properties	Thermal conductivity	~1.2 W/mK
	Melting point	1975 °C
Descriptive Properties	Color	White
	Crystal Structure	Hexagonal /wurtzite

1.4.1.1 Structural properties

ZnO has different kinds of crystal structures -NaCl rocksalt, zinc blende and wurtzite. The zinc atom is surrounded by four oxygen atoms located at the corners of a tetrahedron and vice versa. In ZnO crystal, Zn²⁺ and O²⁻ planes are formed alternately along the c-axis (the [001] direction). - The zinc-blende ZnO structure is stabilized by growth on cubic substrates only, whereas the rocksalt

structure can be obtained at relatively high pressures. The wurtzite crystal structure represents the most commonly observed phase in ZnO thin films and nanostructures (Özgür et al., 2005). This dissertation focuses on the wurtzite (hexagonal) crystal structure. A schematic illustration of the ZnO wurtzite crystal structure is shown in Figure 1.3.

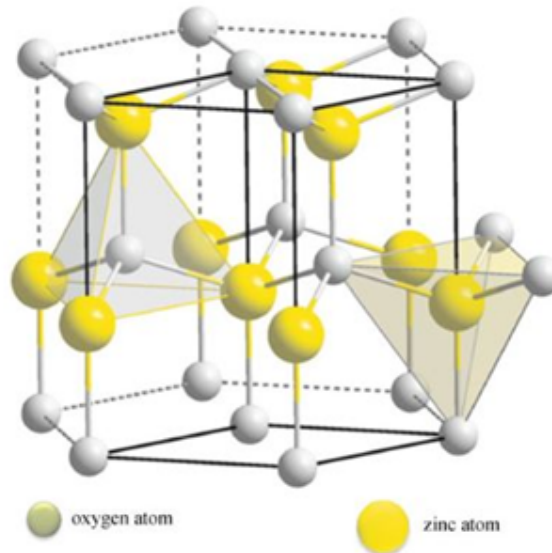


Figure 1.3: Hexagonal crystal structure of ZnO (Samanta et al., 2011).

1.4.1.2 Optical properties

The ZnO emission spectrum is characterized by near-band edge emission (NBE). The NBE consists of a sharp UV emission peak centered at $\sim 367\text{nm}$ ($\sim 3.37\text{eV}$) at 4 K, which is due to the band-to-band transition (the electrons in the conduction band and the holes in the valence band). The NBE peak also consists of excitons (electron-hole pairs) emission that can be free to move through the crystal as well as bound exciton emission that can be bound to donors or acceptors (in both neutral or charged states) (Meyer et al., 2004). The broad emission band located in the visible region (400 -600 nm) is attributed to the presence of intrinsic and/or extrinsic defect states located at a deep level as shown in Figure 1.4 The optical and electrical properties of ZnO can be altered due to the changes in these deep level defects in the crystal structure of ZnO. The point defects, which play an important role in the optical properties of ZnO, strongly depend on the growth conditions and methods. Several research groups have proposed different origins for these deep level defects, such as oxygen vacancies (V_O), interstitial oxygen (O_i), zinc vacancies (V_{Zn}), interstitial zinc (Zn_i), oxygen anti-site (O_{Zn}) and zinc anti-site (Zn_O).

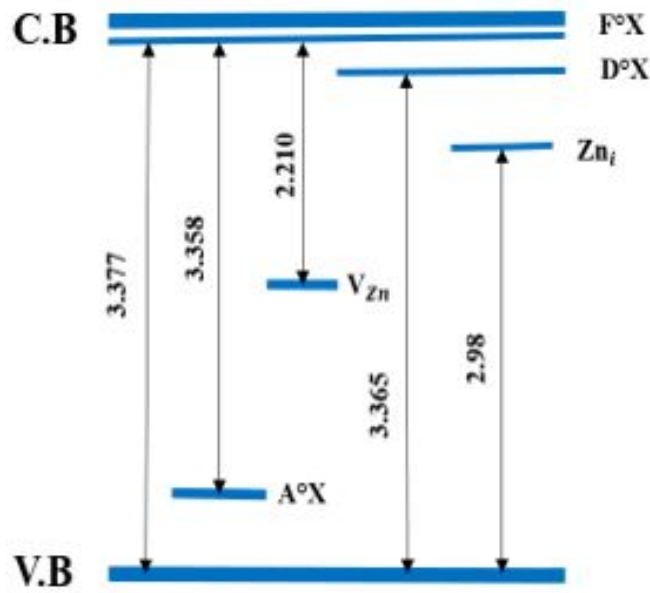


Figure 1.4: Schematics of energy levels for ZnO (the figure is redrawn from (Shimada et al., 2012)).

1.4.2 Doping of ZnO

Dopants are responsible for the electrical properties of ZnO. The main problem for the application of ZnO as a material for electro-optic devices is ambipolar doping. Undoped ZnO is n-type because of the intrinsic shallow donors such as Zn interstitial (Zn_i), Zn_i -related complexes, hydrogen (H), and H-related complexes inside ZnO. Furthermore, it has been theoretically calculated that the formation energy of the intrinsic donors in ZnO, reliable p-type ZnO is difficult to be achieved due to this asymmetrical formation energy between the intrinsic donors and acceptors and the forementioned intrinsic shallow donors in ZnO (Yang, 2009), although researchers have been putting their efforts on the p-type ZnO for many years. Different dopants have been tried to achieve p-type ZnO materials. Although p-type doping has attracted more recent attention in ZnO research, n-type materials with high crystallinity and controllable electron carrier concentration are also indispensable for optoelectronic and spintronic applications. The attainment of intentional n-type doping of ZnO is relatively easy compared to p-type doping. Table 1.5 shows some elements that can be used for ZnO doping.

Table 1.5: Comparison of different elements and methods used for doping ZnO.

Element	Chemical formula	Doping content	Temperature	Methods	Application	Ref
Al	Al-ZnO (AZO)	2%	400°C.	Sol- Gel Spray pyrolysis and Dip- Coating	Optoelectronics and sensor applications	(Gungor et al., 2016)
Ni	Ni-ZnO	5 to 25 %	room temperature	electrochemical route	Electronics via ceramics to catalysts	(Bhuiyan et al., 2014)
Cd	Zn_{1-x} Cd_xO	x = 0, 0.03, 0.06, 0.09	50 °C	chemical co- precipitation method	Optoelectronic devices	(Kumar et al., 2017)
Cu	Cu- ZnO	0.25 to 0.75 %	-	Reflux method	Photocatalysis applications	(Kadam et al., 2017)
Mn	Mn-ZnO	3%	550 °C	electrospinning	Photocatalysis applications	(Wang et al., 2016)

CHAPTER 2

FUNDAMENTALS OF PHOTODIODE

2.1 Introduction

A photodiode is a device that consumes light energy to produce an electric current. It is also called a photodetector, a light detector, and a photo-sensor. Photodiodes are designed to work in reverse bias conditions. This chapter overviewed history, types, characteristics and applications of photodetectors. More recent attention has focused on the UV NiO/ZnO heterojunction photodiode.

2.2 History of photodiode

Photodetectors are devices that produce electrons from a photon flux or optical power by photoelectric conversion. They can be seen from the information in Table 2.1 and Table 2.2 that research into photodiode has a long history.

Table 2.1: History of photodiode developments (Renker, 2006).

Year	Development
1940	Photodiode technology developments came out of the basic developments of the PN junction diode.
1950	Photodiode technology was refined in the latter part of that decade, the PIN photodiode was developed.
1959	Light absorption in the wide depletion area of the PIN structure was first investigated in a paper published by Gartner.
1960	Pioneering work in the development of solid-state single photon detectors were done in the RCA company by McIntyre.
1962	Although silicon has been the favored material for photodiodes, germanium its use was first demonstrated by Riesz. The Schottky photodiode has been addressed.
1972	In Japan, a solid-state single-photon detector with a somewhat different design with a horizontal development of the avalanche was patented in 1972.
Recent years	Recent studies have been carried out using a new generation of photodiodes large area, wide bandgap nanotechnology materials, flexible, transparent, and self-powered.

Table 2.2: New type of advanced photodiode (Zou et al., 2018; Husain et al., 2018).

Type	Explanation
Nanostructure UV Detectors	Metal Oxide nanostructures are considered as most promising sensitive photodetection materials because they offer not only high photoconductive gain and the property benefits of 1D nanostructures but also the added benefit of multifunctional or new properties arising from the synergistic effects of combining heterojunction materials.
Transparent UV Detectors	In a transparent material, the energy gap of the electron is higher than the photons, so the electrons will not be able to use the photons' energy, and light will pass through, which will make the material translucent. This is the main characteristic of the solar cell, which is to absorb light.
Large area UV Detector	It can achieve large area detection.
Self-Powered UV Detectors	Self-powered photodetectors work at zero bias without consuming external power, hence they are more portable and adaptable conventional photodetectors. Generally, such self-powered photodetectors fall into two major classes according to energy conversion. One class is based on the photovoltaic effect, which can be directly driven by an optical signal, and convert light energy into electric energy through the photoelectron excitation process. The other class contains an integrated energy unit, which transforms UV radiation into electrical and chemical energy. These devices usually operate by a combination of the photoelectric and photoelectrochemical (PEC) effects. The photovoltaic effect has huge potential for exploitation in novel self-powered UV photodetectors containing p-n junctions, heterojunctions, or Schottky junctions.
Flexible UV Detectors	Recently, flexible devices have become more prevalent to develop portable, wearable, lightweight and implantable optoelectronic devices. This also offers numerous opportunities for the development of next-generation UV detectors.

2.3 Photodiode operation principle

The operation of photodetectors is based on photoconductive or photovoltaic effects (Xu, 2015). The absorption of photons may lead to electron excitation from the valence band to the conduction band. Figure 2.1 showed the operation steps from carrier generation to external current. The generates electron-hole pairs which increase the mobile charge carriers. This can increase the conductivity of the material (which is the photoconductive effect), or it can induce a current by accelerating the electron-hole pair by the built-in electric field (which is the photovoltaic effect). In both cases, since this produces a current in the external circuit that is proportional to photon flux, such devices are used to detect the presence of light. Furthermore, In the photovoltaic mode, the diode is not connected to the power source we do not bias the diode. which means no biased source. When the light falls in such condition on the photodiode, it excites the electrons to a higher energy state and results in electrons moving towards the cathode terminal and holes towards the anode terminal. This process creates a potential difference between the two terminals. In photoconductive mode, the diode is connected to the power source and we reverse biased the diode. When the light falls on the photodiode, it creates a pair of electrons and holes and moves towards the opposite direction due to biased voltage.

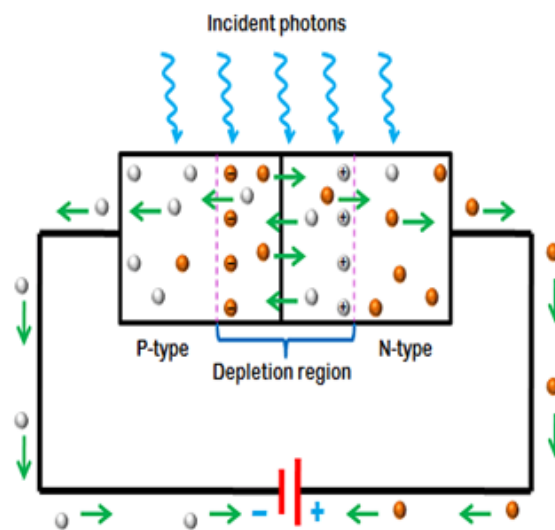


Figure 2.1: Definition of the operation of a photodiode.

2.4 Types of photodiode

Although the term photodiode is widely used, there are several different types of photodiode technology that can be used. As they offer different properties, the different photodiode technologies are used in different areas.

2.4.1 PN junction photodiode

PN junction photodiodes are the first form of photodiodes. Figure 2.2 presented PN junction photodiode is also simply referred to as a photodiode. In photodiodes, most of the electric current is carried by the charge carriers generated in the depletion region because the charge carriers in the depletion region have high drift velocity and low recombination rate whereas the charge carriers in the n-side or p-side have low drift velocity and high recombination rate. In a p-n junction device, under irradiation, the photogenerated electron-hole pairs in the region will be separated by the built in field, and electrons (or holes) will be swept to the n-type material (or p-type material) side, resulting in a photocurrent in the device (sit, 2013a).

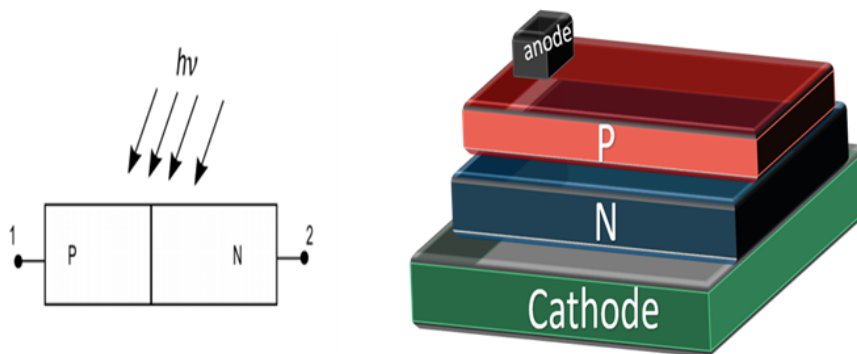


Figure 2.2: Device structure of the p-n junction photodetector.

2.4.2 PIN junction photodiode

A PIN photodiode is a photodiode with an intrinsic (undoped) region in between the n- and p-doped regions. Most of the photons are absorbed in the intrinsic region and carriers generated therein can efficiently contribute to the photocurrent. The benefits of PIN photodiode design. Most carriers are generated in the intrinsic region because that can be much thicker than the depletion region of a PN structure. Another effect of the thick intrinsic region can be the reduced capacitance, which allows for a higher detection bandwidth.

In Figure 2.3, the electrodes are shown in black: the cathode is a flat electrode, whereas the anode has the form of a ring (of which two opposite parts are seen in the shown cross-section). The positive pole of the (reverse) bias voltage is connected to the cathode. On top of the p region, there is an anti-reflection coating (sit, 2013b) .

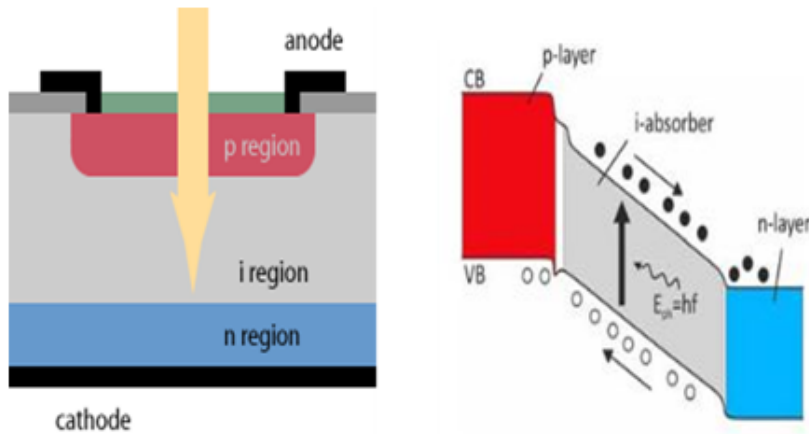


Figure 2.3: Schematic drawings of a PIN photodiode.

2.4.3 Schottky photodiode

The Schottky photodiode utilizes a metal-semiconductor junction to separate and collect the photo-generated charge carriers. Photons pass through a partially transparent metallic layer (often gold) and are absorbed in the n-type semiconductor. Charge carriers generated within the depletion region are efficiently swept out by the built-in electric field giving rise to a photocurrent. Schottky photodiodes are primarily used for detecting blue or UV wavelengths or in high-speed applications where some loss in efficiency can be tolerated. (Quimby, 2006).

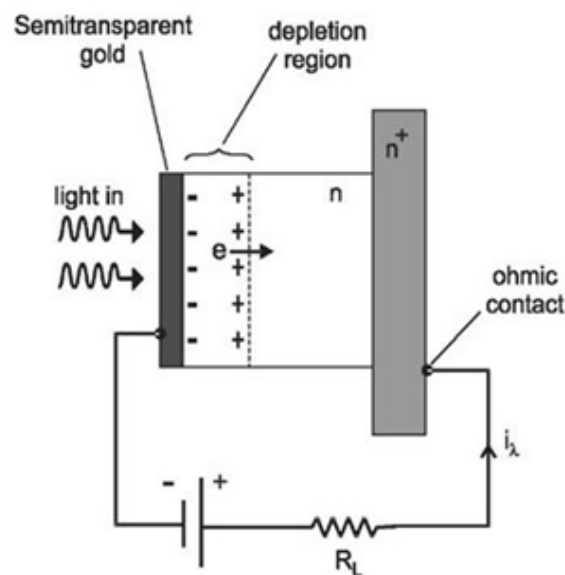


Figure 2.4: Schematic drawings of in a Schottky photodiode, light is absorbed in the depletion region of an n-type semiconductor after passing through a semitransparent metallic film (Quimby, 2006).

2.4.4 Avalanche photodiode

An avalanche photodiode (APD) as shown in Figure 2.5 as a cross-section of which is indispensable for the detection of very weak and fast-changing optical signals. An avalanche photodiode (APD) is indispensable for the detection of very weak and fast-changing optical signals. Detection in APDs takes advantage of the internal photoelectric effect as well as the phenomenon of avalanche multiplication of carriers in a reverse-biased silicon p-n junction. APDs find application in many fields of science and technology, among the others in automation techniques, medicine, environment protection, geodesy and military techniques (Campbell, 2016).

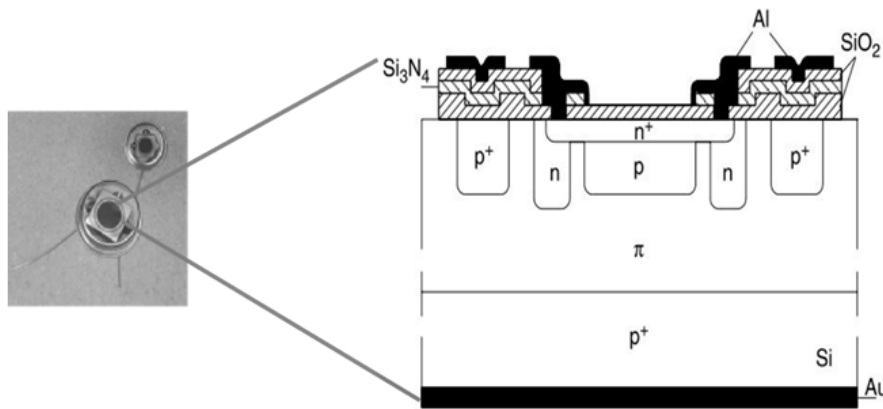


Figure 2.5: Photograph of 3 mm and 5 mm APDs. Cross-section of an ITE APD structure (Campbell, 2016).

2.5 Characteristics of photodiode

2.5.1 Current versus Voltage Characteristics

The ideal current-voltage characteristics are based on the following four assumptions: (1) the abrupt depletion-layer approximation; that is, the built-in potential and applied voltages, are supported by a dipole layer with abrupt boundaries, and outside the boundaries the semiconductor is assumed to be neutral; (2) the Boltzmann approximation, generally, the Fermi level lies at least $3k_B T$ from the bandgap edge; (3) the low injection assumption; that is, the injected minority carrier densities are small compared with the majority carrier densities; (4) no generation current exists in the depletion layer, and the electron and hole currents are constant through the depletion layer. Using these assumptions, after some derivation work, one can end up with the Shockley equation (Xu, 2015).

$$J = J_0 \left[e^{\frac{qV}{K_B T}} - 1 \right] \quad (2.1)$$

where J_0 is the saturation current density. One model for photodiode analysis is proposed based on the the Shockley diode model. The Shockley equation relates the current and voltage in dark conditions by:

$$I_D = I_0 \left[e^{\frac{qV}{K_B T}} - 1 \right] \quad (2.2)$$

An illuminated photodiode has reverse photocurrent I_{ph} which is proportional to the incident optical power and is therefore modeled by:

$$I = I_0 \left[e^{\frac{qV}{nK_B T}} - 1 \right] - I_{ph} \quad (2.3)$$

where n is the ideality factor which is defined as how closely a diode follows the ideal diode equations.

The characteristic I-V curve is obtained under dark and illumination conditions as shown in Figure 2.6. The regime when the applied voltage is greater than zero ($V_{bias} > 0$), is called forward bias, here the current increases exponentially, because the polarity conditions of the electrodes are favorable for the generation of photocurrent, as where the anode becomes more positive and the cathode more negative. On the contrary, under reverse bias ($V_{bias} < 0$), the measured current is saturated and it is extremely low because the anode becomes more negative and the cathode more positive, creating an energy barrier for the carriers to be injected from the electrodes to the film.

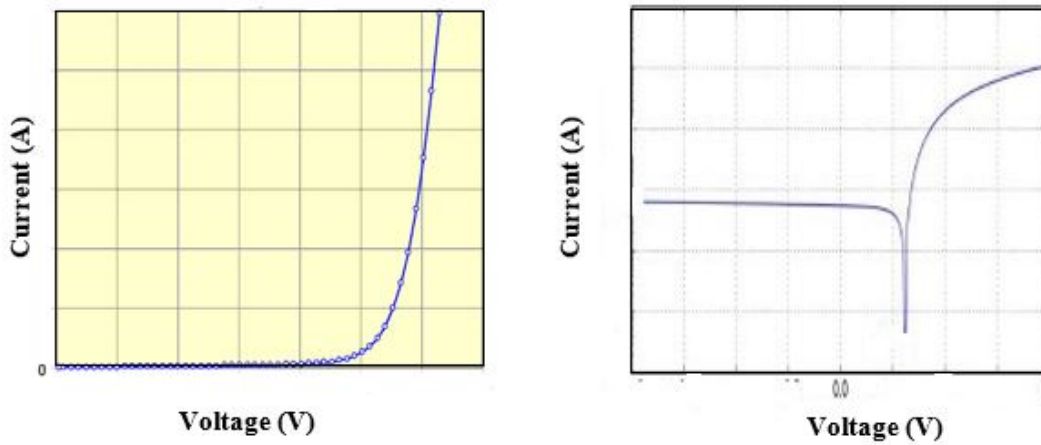


Figure 2.6: Characteristic I-V curve of a photodiode in linear and logarithmic scale.

Dark current (without light) is equivalent to the noise source and will weaken the signal to noise ratio.

In photodiodes and other detectors with some PN or PIN junction, it is often caused by thermal excitation (generation) of carriers not necessarily directly from valence to conduction band, but possibly through defect states related to crystal defects or impurities. The rate of such thermal processes depends not only on the active area, but also critically on the temperature and on the bandgap energy of the material, and also on the operation voltage (particularly near the breakdown voltage, where impact ionization can occur). At high voltages, tunneling through the depletion region may also contribute.

2.5.2 Quantum efficiency

Every incident UV photon will try to produce an electron-hole pair however, the number of created electron and hole pairs is usually less than the number of photons as defined in Equation 2.4. Quantum efficiency as shown in Equation 2.5 refers to the fraction of the fractional number of carriers generated per incident photon.

$$\Phi = \frac{P_{opt}}{h\nu} \quad (2.4)$$

$$\eta = \frac{\frac{I_{ph}}{e}}{\frac{P}{h\nu}} \quad (2.5)$$

Which $0 < \eta < 1$.

Φ : Photo flux.

I_{ph}/e is the number of carriers generated Carrier flux generated which contribute to photocurrent.

$P/h\nu$ is the number of photons photon flux os number of photons incident per unit time.

2.5.3 Responsivity

The responsivity of a photodetector is the electrical current divided by the incident optical power. The unit for responsivity is the amperes per watt. Assuming all photons are converted to electron-hole pairs. The responsivity defined as Equation 2.6.

$$R = \frac{I_{ph}}{P} \quad (2.6)$$

Where I_{ph} is photocurrent, and P is the optical intensity (or light intensity).

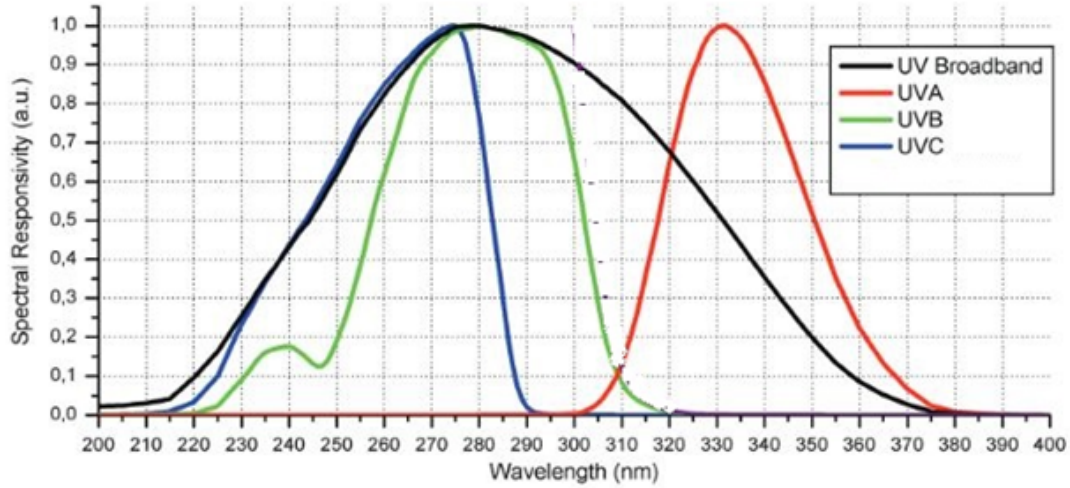


Figure 2.7: Spectral responsivity characteristics of UV photodetectors.

Cut-off Wavelength is the longest wavelength that a UV detector can detect, it can be measured by absorption and transmittance Spectrum.

2.5.4 Spectral Response

The spectral response of a photodetector is the range of optical wavelengths or frequencies in which the detector has a significant responsivity. It is primarily affected by the bandgap of materials, but it can also be controlled by the thickness of materials, impurity-doped region, and impurity concentration. The variation of the responsivity as a function of wavelength, $R(\lambda)$, is known as the spectral response of the photodetector.

2.5.5 Response Time

Time response: When the light turns on or off, the required time of the output value rises to become stable or decreases to the value before irradiation accordingly this implies the sensitivity of the device. It can be extracted from Equation 2.7.

$$\tau_{RC} = (R_L + R_S)C \quad (2.7)$$

Where C is the capacitance, the product RC is known as the time constant, τ :lifetime, R_L the load resistance, R_S resistance in series.

2.6 Application of photodiode

The various applications of photodiodes are: Photodiodes are used in medical applications such as computed tomography, instruments to analyze samples and pulse oximeters. Also photodiodes are used for optical communications and to measure extremely low light intensities measurement.

Photodiodes majorly find their use in counters and switching circuits. Logic circuits and encoders also make use of photodiode. It is widely used in burglary alarm systems. In such alarm systems, until radiation exposure is not interrupted, the current flows. As the light energy fails to fall on the device, it sounds like an alarm.

CHAPTER 3

NiO/ZnO Heterojunction Photodiode

3.1 Introduction

The role of NiO/ ZnO heterojunction has received increased attention across several disciplines in recent years. One of the most significant current discussions is the fundamentals NiO/ZnO interface which is presented in this chapter and we summarized previous research studies about NiO/ZnO heterojunction devices.

3.2 Heterojunction types

In general, heterojunctions can be classified into type-I, type-II, and type-III heterojunctions based on their distinct band offsets. For the type-I heterojunctions, since the conduction band minimum (CBM) is higher and the valence band maximum (VBM) is lower than those in the other material, both the electrons and holes tend to transfer to the right for the arrangement depicted in Figure 3.1 (a) Therefore, type-I heterojunctions have been widely used in light-emitting devices such as LEDs and semiconductor lasers where the charge carrier recombination is required.

For a typical type-II heterojunction, the bandgaps from two semiconductors form a staggered alignment, in other words, the energies of the conduction and valence bands of one semiconductor are relatively higher than the other semiconductor. Thus, following the initial generation of charge carriers under the external stimulus, the electrons and/or holes tend to transfer through the interface towards the opposite direction, resulting in the spatial separation of charge carriers and subsequent built-in electric field. Such charge confinement is of great importance in certain optoelectronic devices especially with light absorption or emission involved, such as solar cells and photodetectors, since the efficient regulation of the carrier separation and transportation dominantly determines the performance of such devices. In addition, the interfacial transition may extend the spectral range to a significantly longer wavelength than that defined by the bandgap of any of the components. Type III of heterojunction (broken-gap)The band gaps do not overlap at all. The situation for carrier transfer is like type II, just more pronounced. (Zheng et al., 2020).

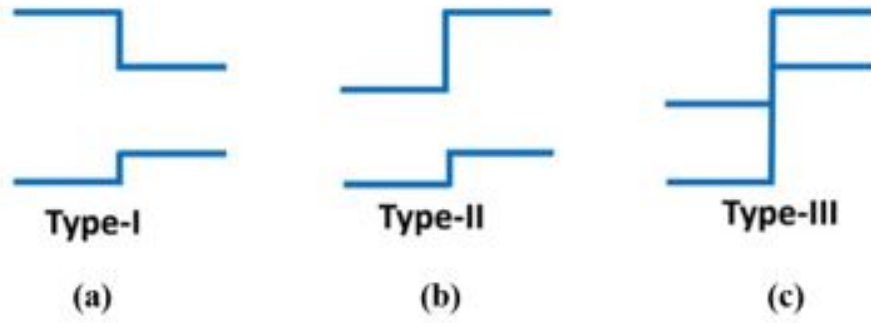


Figure 3.1: Schematic energy band diagram of three types of semiconductor heterojunctions.

Additionally, Based on the conductivity, heterojunctions can be classified into two types: isotype, where two semiconductors are both n-type or p-type, or anisotype, where two semiconductors form a p-n heterojunction. For anisotype type-II heterojunction, similar to that of the p-n homojunction, the band alignment under thermal equilibrium is due to the process of electron/hole diffusion in the interface. When a heterojunction is formed, the excess number of electrons in the n-type semiconductor would diffuse into the p-type semiconductor, and vice versa. As the electrons and holes diffuse, there will be positively charged donor atoms and negatively charged acceptor atoms left in the n-type and p-type semiconductors, respectively. As a result, the depletion regions are generated in both n-type and p-type semiconductors, with a net positive and a negative charge, respectively. Such net charges generate an electric field with the direction from the n-type semiconductor to the p-type semiconductor, which provides an opposite force to the charge diffusion. As the electric field increase to the exact value of the diffusion, the junction reaches thermal equilibrium. For the anisotype heterojunction, it behaves as a typical pen junction diode (Zheng et al., 2020).

3.3 NiO/ZnO band diagram

As with all semiconductor devices, the key to understanding the behavior of heterojunctions is the energy band profile which graphs the energy of the conduction and valence band edges versus position. The interface is between two regions of dissimilar metal oxide semiconductors ZnO and NiO.

The conduction band levels CB are then given by simply subtracting the specific materials' electron affinity from the vacuum level. The valence band levels V B can be calculated by subtracting the bandgap energy from the conduction band levels. Band discontinuities result at the interface from the change of the crystal background field between the two materials, which is very abrupt if compared to the built-in potential caused by a usual charge distribution.

Thus, the energy of the carriers at least one of the band edges must change as those carriers pass

through the heterojunction. Most often, there will be discontinuities in both the conduction and valence band. These discontinuities are the origin of most of the useful properties of heterojunctions. The behavior of a semiconductor junction depends crucially on the alignment of the energy bands at the interface. Figure 3.2 describes the band alignment. How the discontinuities are distributed between the valence and conduction bands is the major question to be answered by theory and experiment. Band offset or potential discontinuity plays a crucial role in building devices.

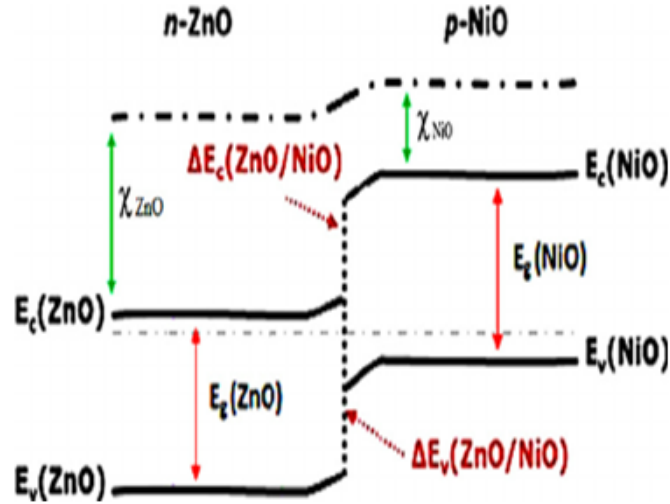


Figure 3.2: Energy-band diagram for p-NiO/n-ZnO heterojunction under zero bias (Jlassi et al., 2014).

Electron affinity rule, The oldest rule is that given by Anderson which is defined using Equations 3.1, 3.2 and 3.3 according to this rule, the discontinuity in the conduction band edges is the difference of the electron affinities for the constituents, the conduction band offset (ΔE_C):

$$\Delta E_C = x_2 - x_1 \quad (3.1)$$

where x_1 and x_2 are the electron affinities of material 1 and 2 constituting the heterojunction. bandgap discontinuity (ΔE_g):

$$\Delta E_g = E_{g2} - E_{g1} \quad (3.2)$$

And the valence band offset (ΔE_V):

$$\Delta E_V = \Delta E_C + \Delta E_g \quad (3.3)$$

Yang et al. (2011) reported the valence-band offset ΔE_V is determined to be 1.47 eV. According to the bandgap of 3.7 eV for NiO and 3.37 eV for ZnO, the conduction-band offset ΔE_C in the structure was calculated to be 1.8 eV, and it has a type-II band alignment. Type II: (staggered) The bandgaps

overlap, but one ΔE_C , ΔE_V changes sign. $E_{V_1} > E_{V_2}$ but E_{g_2} is not necessarily smaller than E_{g_1} . In the ultrathin geometry, understanding and control of interface electronic structure and chemical reactions at the NiO/ZnO interface are critical to functionality, as oxygen atoms are shared at the interface of the dissimilar materials (Karsthof et al., 2020). NiO tends to form contacts with other materials exhibiting large band offsets in both valence and conduction bands because of its low electron affinity of 1.46 eV. In most cases, this will lead to a so-called type-II band alignment where two materials share a gap of reduced size at the interface ('staggered gap'). Such a situation is sometimes considered undesirable because it invokes electron-hole recombination at the heterointerface. For that reason, there have only been few attempts to develop a theory that describes the current transport mechanism in a type-II system (Dolega, 1963), the high band offsets act as barriers for minority carrier reinjection which overall benefits the device performance. Interface recombination limited transport in type-II heterojunctions. That the defect properties of the interface have a pivotal role in determining the parameters of the current-voltage relationship (Karsthof et al., 2020). As with many electronic devices, the interfacial electronic and chemical structure is expected to be important. In the case of ultrathin junctions needed for recombination, interfacial chemistry will be critical as one or both oxide layers may be fully depleted of their majority charge carrier. The interface quality has an impact on the behavior of the device. the highest fraction of interfacial electronic states and the lowest band offset (ΔE) between the ZnO conduction band (ECB) and the NiO valence band (EVB). This interface showed the largest reverse current, indicating free carriers could readily leak across the interface, even under low internal electric fields the lowest fraction of interface states and largest ΔE . This interface also demonstrated the highest rectification, with decreased reverse bias and increased breakdown voltage in forwarding bias (Steirer et al., 2017).

3.4 Application of NiO/ZnO heterojunctions

Elementally abundant, low-cost metal NiO/ZnO heterojunctions are of interest for UV optical sensing, gas sensing, photocatalysis, charge confinement layers, piezoelectric nanogenerators, and flash memory devices. These heterojunctions can also be used as current rectifiers and potentially as recombination layers in tandem photovoltaic stacks by making the two oxide layers ultrathin. An optimally designed NiO/ZnO thin film heterojunction could potentially be used as a recombination layer in a tandem cell; however, careful control of band edge energetics would be required to guide interface-free carrier transport. In the case of UV photodetection, the oxide/oxide junction should be highly rectifying, whereas, in the case of a tandem photovoltaic cell, the oxide/oxide heterojunction should promote recombination (Steirer et al., 2017).

3.5 Review of NiO/ZnO heterojunction photodiodes

Several studies have reported in investigations into NiO/ZnO heterojunction photodiode:

The fabrication and characterization of an optically transparent p–n heterojunction device consisting of p-NiO and n- ZnO are presented by Tsai et al. (2011). Emphasizing the device performance including the current-voltage characteristics of the photodiode under illumination and spectral response measurements. However, during I–V measurements, no luminescence was observed under the forward bias because of the high density of interface traps between the n-ZnO and p-NiO film. Furthermore, the ratios of photocurrent to dark current contrast for p-NiO/n-ZnO heterojunction can be determined by measuring dark currents and photocurrents. A low current contrast ratio is possibly due to imperfections of the heterojunction interface traps between the ZnO and NiO films which provide current tunneling paths under reverse current.

Shen et al. (2015) fabricated a p-NiO/n-ZnO nanorod array, as presented in Figure 3.3 based UV detector using an all solution process method and studied its self-powered detection performance under a nominal zero bias. The structural properties, photoelectric response properties, and the self-powered mechanism of the devices were investigated. The measurable photovoltaic effect existed under UV illumination, which was responsible for the self-powered performance of the fabricated ZnO/NiO UV detectors. Specifically, a proper built-in electric field between ZnO and NiO. It arising from the devices' well-aligned energy band structure could separate efficiently the photogenerated electron-hole pairs in ZnO at the heterojunction interface. To help the charge carriers transport to corresponding electrodes, resulting in photocurrent.

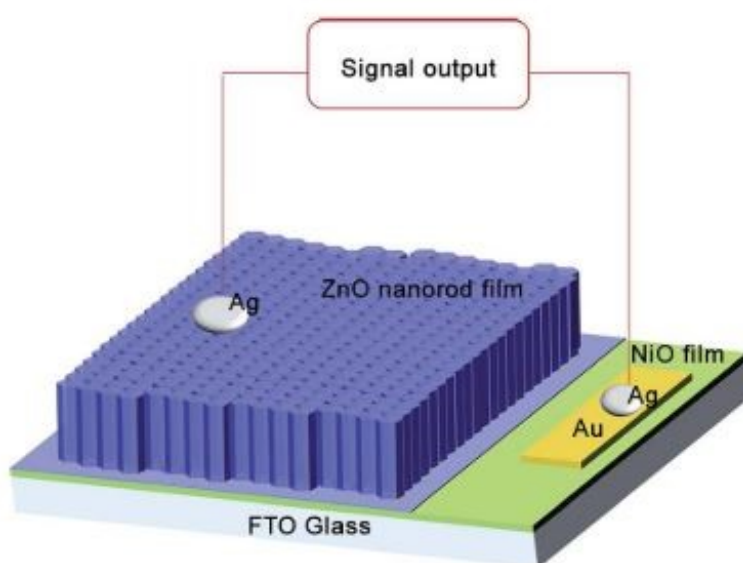


Figure 3.3: Schematic diagram of the device structure (Shen et al., 2015).

Grundmann et al. (2014) reported that wide-gap semiconductors are often unipolar and can form type II bipolar heterostructures with large band discontinuities. They present such diodes with very high rectification. The I-V characteristics of NiO/ZnO bipolar heterostructure are shown in Figure 3.4. The current is assumed to be entirely due to interface recombination. They derive the ideality factor for both symmetric and asymmetric diodes and find it close to 2 in agreement with experimental data from NiO/ZnO and CuI/ZnO type II diodes. The comparison with experimental results showed that the actual interface recombination rate is orders of magnitude smaller than its possible maximum value. Such a diode exhibits interface recombination as the dominant current transfer mechanism across the interface because the large conduction and valence band offsets block thermal currents. Then the diode current is purely a recombination current via traps at the interface. They assume a very thin layer at the interface with traps leading to an interface recombination current density.

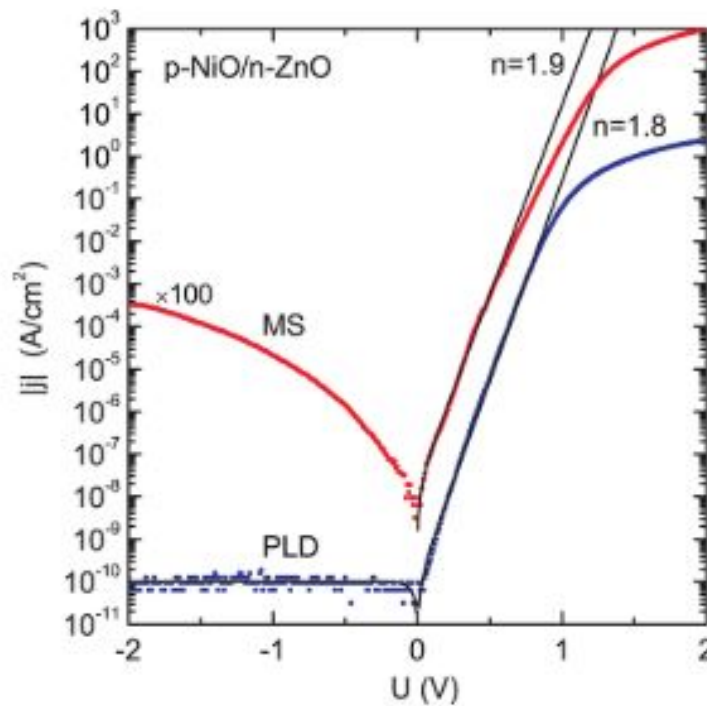


Figure 3.4: J-V characteristics of NiO/ZnO bipolar heterostructure (Grundmann et al., 2014).

Patel et al. (2015) fabricated a UV detector using large energy bandgap materials. A transparent UV detector was achieved using p-type NiO and n-type ZnO heterojunction formation as shown in Figure 3.5, using sputtering method was applied to deposit ZnO and NiO layers. With noticing p-NiO and n-ZnO photodetector can work well without an external metal electrode. Mott-Schottky analyses are applied to develop the interface of NiO and ZnO by establishing energy diagrams. Defects inside the nanocrystalline NiO film enhance the UV detection defect-assisted carrier transportation. The results provide a solid manipulation of NiO defects for functional photoelectric device applica-

tions. Moreover, the existence of defects in the nanocrystalline NiO significantly enhances the drift transport of the carriers, allowing them to reach the ZnO layer through a defect-assisted carrier transport mechanism. This systematic investigation of defect engineering of nanocrystalline NiO showed a high possibility of being an effective design scheme for large bandgap materials and functional applications.

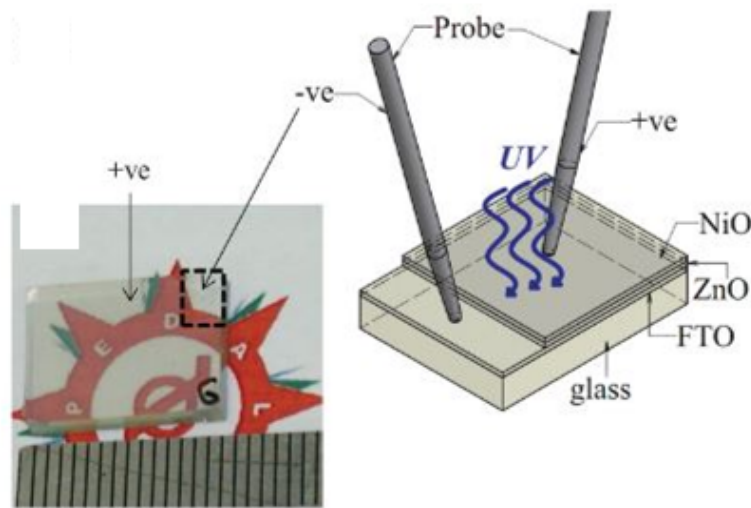


Figure 3.5: Schematic and illustration of the developed transparent NiO/ZnO heterojunction UV photodetector (Patel et al., 2015).

Karsthof et al. (2016) used a model that considers recombination losses at the NiO/ZnO interface as well as within the electric field region, yielding a high hole interface recombination and collection efficiency is strongly deteriorated by recombination velocity. They conclude that the carrier losses at the NiO/ZnO interface, causing a strong bending of the J-V characteristics under illumination (presented in Figure 3.6). Moreover, the recombination velocity extracted from this analysis is much larger than that obtained for holes from the J-V characterization in the dark state. A possible explanation is that the illumination with sunlight creates a completely different situation with regard to the ability of interface states to act as recombination centers when compared to the dark state. As already stated above, the illumination might lead to optical emission of trapped charge carriers from the interface states, thereby strongly increasing the recombination probability for both injected and photogenerated carriers. In order to increase the fill factors of the solar cells, it might be necessary to improve the NiO/ZnO hetero-interface, i.e., reduce the density of interface defects, for example, by the introduction of buffer layers or a specific passivation treatment of the ZnO surface prior to NiO deposition.

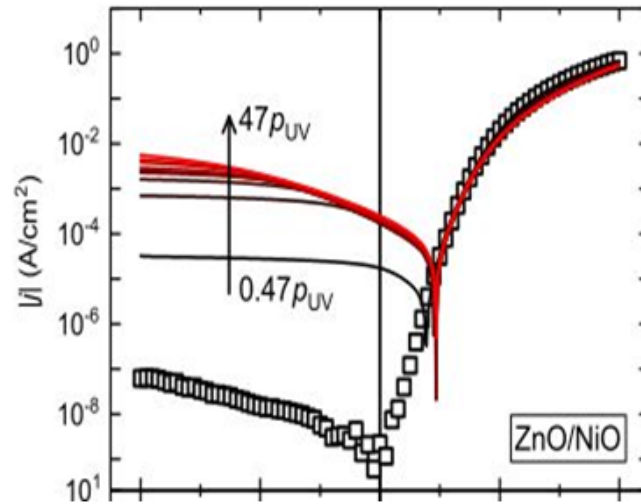


Figure 3.6: Current–density voltage relations of a ZnO/eclipse-NiO heterojunction under dark and UV illumination for different intensities (Karsthof et al., 2016).

The effect of the oxidation temperature was studied by Luo et al. (2016). Ni film was deposited on the sapphire by thermal evaporation. The ZnO nanorod arrays were grown on the NiO thin film by hydrothermal method. A seed layer of ZnO was prepared by room temperature radio frequency magnetron sputtering. By comparing the photoresponse properties of the UV photodetector oxidized at different temperatures, the authors suggested that the oxidation temperatures influence the defect density of NiO films, thereby influencing the rise time and decay time. The defect density affects the photoresponse characteristics that the decay time decreases with the decreasing of defect density as the NiO oxidation temperature increases. The photon-desorption of oxygen at the PN interface modifies the density of defects states, and hence alters the PN interface. Both of the two processes may lower the height and narrow the width of the PN, thus electrons may transit over the lowered height of the PN or tunnel through the narrowed width of the PN interface.

Steirer et al. (2017) controlled of surface hydroxyl driven chemistry in ultrathin NiO/ZnO heterojunctions can significantly affect the ZnO electronic structure and performance of the heterojunction. A combined analysis of chemical and electronic features enables a closer and more accurate look at the details of these nanoscale heterojunctions, wherein the interface properties manifest in systematic changes in rectification ratios and leakage currents, with implications on device durability. The critical feature of the interface states is that the apparent magnitude of the states is chemically controllable through the basicity of the underlying substrate. This finding is especially important as traditional p-n junctions typically have depletion widths that can span up to micrometers whereas, in nanoscale devices, one or both oxide layers may be fully depleted. The results suggest that hydroxyl

control of functional ultrathin oxide-oxide heterojunctions is likely to have a significant impact on the electronic properties. Applications can be found in sensing, catalytic, and photocatalytic systems where nanometer-scale interfaces often dominate key functional properties.

Mohammadi et al. (2017) presented the fabrication and characterization of an optically transparent p–n heterojunction device consisting of n-ZnO and p-NiO(CuO) layers using Chemical bath deposition (CBD) method. Three different structures are studied. Since the NiO and CuO layers are intrinsically p-type, we utilize these layers to fabricate a ZnO/CuO, ZnO/NiO, and ZnO/CuO/NiO heterojunctions emphasizing the device performance, including the current-voltage characteristics of the photodiode under illumination (as shown in Figure 3.7), and spectral response measurements. They found UV photodetection of devices however for ZnO/CuO/NiO heterostructure there is a considerable difference between dark and photocurrent. Because of the wider bandgap of both layers in ZnO/NiO, the absorption of UV light has a larger portion and hence this type of detector responds better.

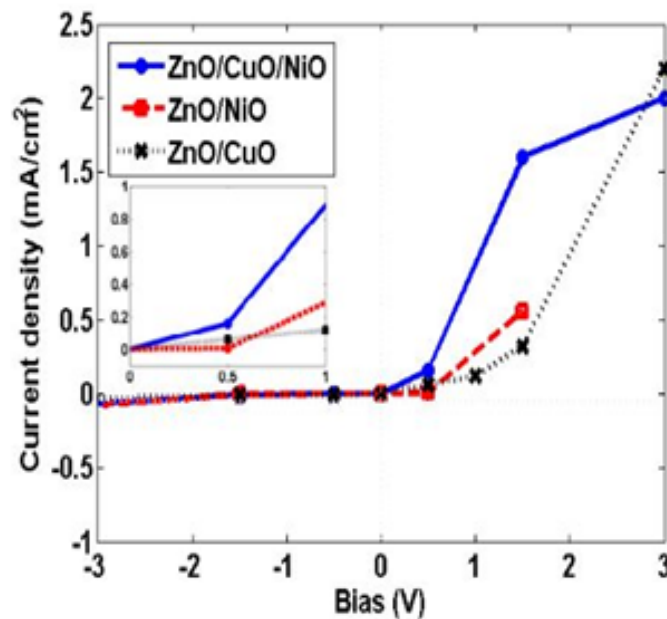


Figure 3.7: Measured I-V characteristics of samples (Mohammadi et al., 2017).

Patel et al. (2017) fabricated NiO/ZnO/ITO/PET photodetector where showed excellent photodetection properties, and a specific bias mode can be purposely selected for enhancing performances. This lightweight and high-performing UV photodetector would benefit from UV-related sensors, including the cockpit's window for missile defense. The colorless photoelectric devices were demonstrated for high-performing transparent photodetectors. The all-transparent ZnO/ NiO heterojunction was achieved by large available sputtering methods for the consecutive solid-state deposition schemes.

The extreme UV photodetector was achieved by remarkable photoresponse as fast as 19 ms due to the merit of excitonic absorption. By active utilization of the exciton, the ZnO/NiO heterojunction can be applied as the visible electronic devices and solar cells with features of the perfect UV absorption, all-transparency and fast photoresponses.

Sultan et al. (2017) reported the growth and functionality of a NiO/ZnO nanostructured p-n heterojunction fully prepared by solution method. Structural, and morphological characterizations suggest hexagonal (002) plane dominated ZnO nanorods that are covered by NiO nanostructures. Optical characterization showed that the device is partially transparent. The XPS measurements were used for band alignment studies which reveal type-II band alignment of the junction. Temperature-dependent electrical properties of the heterostructures were analyzed to extract ideality factor, series resistance and rectification ratio. These properties were compared with previously reported values for similar devices prepared by physical deposition techniques and that for organic-inorganic heterojunction devices. Hybrid NiO-ZnO showed some absorbance in the visible range as compared to pure ZnO and NiO. They conclude that the reason for the improved absorbance of the hybrid NiO-ZnO could be the intrinsic defects (V_{Ni}) in NiO or the formation of oxygen vacancies in ZnO nanorods and NiO/ZnO interface which result in the improved absorbance. They conclude that inexpensive heterostructures chemically processed at low temperatures are viable for electronic device applications with comparable properties to the high-temperature processed counterparts.

Klochko et al. (2018) presented metal oxide heterojunction p-NiO/ n-ZnO prepared by two low-temperature solution growth techniques (cathodic electrochemical deposition and Ionic Layer Adsorption and Reaction (SILAR) method). The important results As the NiO thickness increases, the transparency decreases regularly. All as-deposited NiO films have a brownish color, partly losing the visible transparency and enhancing reflectance. The systematic investigation of defect engineering of nanoscale NiO, the control of defects of the metal oxides and the improvement of the NiO/ZnO heterostructure design will provide a strong potential for photovoltaic applications.

Hwang et al. (2019) assumed that the photodetector (PD) without the PVK insertion layer demonstrates poor rectifying behavior due to a large barrier existing at the p-NiO/n-ZnO interface. They observed that the insertion of the organic PVK layer in p-NiO/n-ZnO heterojunction PDs largely improved carrier transport and thus enabled superior rectifying characteristics compared to the PD without PVK. The insertion of PVK also reduces the visible response and increases the UV response. The PD without PVK showed poor rectifying behavior due to the large barrier existing at the p-NiO/n-ZnO interface. The interface itself has many defects, which causes a tunneling current and thus linear I-V dependence in forwarding bias. After inserting the PVK layer, the large barrier height at the p-NiO/n-ZnO interface was split into two small barriers and the tunneling current is suppressed; hence,

the carriers can easily transport in the PD and possess superior rectifying characteristics. The PD without PVK demonstrates a large visible response due to the thermally generated carriers; however, these carriers are trapped by PVK, reducing the visible response by approximately two orders.

Karsthof et al. (2020) have investigated two types of heterojunctions comprising p-type NiO, both characterized by large band offsets toward the second oxide. In the first case, ZnO was the n-type partner, forming a type-II band alignment with NiO. The electrical current through such a configuration is determined by the rate at which electrons and holes recombine at the interface. They have developed a simplified framework to model the parameters of the current-voltage relationship and have demonstrated the critical impact of the interface quality in terms of defect population. A method to reduce the amount of interface defects introduced during NiO growth was given. The ZnO/NiO contacts can be employed as UV-converting solar cells with record efficiency; however, they presented evidence for a recombination process triggered by UV light, which we attribute to the previously identified recombination center NiZn that forms by in diffusion of Ni into the topmost layers of ZnO.

The NiO/ZnO heterojunction photodetectors were fabricated by CBD method. The self-powered photoresponse performance was investigated by Wei et al. (2020). The crystal quality, optical and electronic properties of ZnO NRs were modified by the Al^{3+} ions additions in the precursor solution. The heterojunction devices exhibit the photoresponse performance with UV spectral selectivity without an external electric field. The good photoresponse properties of the devices are correlated with ZnO NRs with good crystal quality, few surface defect states, high carrier concentration and high EF value. The larger built-in electric field formed in the interface of NiO nanoflakes and ZnO with 0.5% Al^{3+} ions additions facilitates the separation and transport of photogenerated carriers, as well as reduces the carrier recombination, and then improves the performance for the devices such as photocurrent, signal-to-noise ratio, photoresponsivity and detectivity.

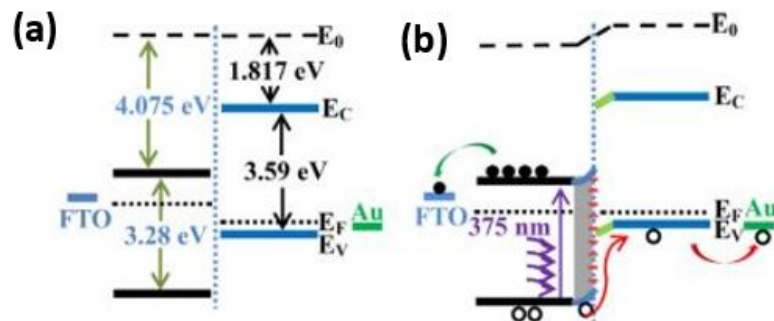


Figure 3.8: The structures and energy band diagrams of NiO/ZnO (a) before and (b) after contact (Wei et al., 2020).

Table 3.1: Review most common previous works which focus on the development of UV photodetectors based on metal oxides materials.

Device structure	Bias (v)	Wavelength λ (nm)	Responsivity		Detectivity D(Jones)	EQE		Rise time		Fall time τ_f (s)	Ref
			R(A/W)	R(μA/W)		D(Jones)	EQE	τ_r (s)	τ_f (s)		
NiO /ZnO/ITO	0	365	20 μ A/W		7.2×10^{11}	-	41 μ	71 μ	(Patel et al., 2017)		
Ti-Au /ZnO/NiO /ITO	-1.2	370	Top illumination		2.9×10^{12}	45%	-	-	(Hasan et al., 2015)		
			0.14								
			Bottom illumination								
			0.19		3.8×10^{12}	63%					
Ag/ZnO/Ag	5	365	788 mA/W		-	-	16	18	(Inamdar et al., 2014)		
Pd/ZnONRs/Pd	1.8	-	0.199		-	-	-	-	(Pardakhty et al., 2017)		
Ni/NiO/ZnO /FTO	-5	400	3.85		9.6×10^{13}	-	24.2 ms	212 ms	(Karsthof et al., 2020)		
Ti- Au/ZnO/NiO/FTO	1	365	0.28		6.31011	93%	0.28	5.8	(Debnath et al., 2015)		
Ag/Si/ NiO/Ag	-2	600	0.43		-	89.5 %	-	-	(Ko et al., 2015)		
	0									-	1.5×10^{10}

CHAPTER 4

EXPERIMENTAL DETAILS

4.1 Introduction

In this chapter different aspects of the experimental techniques are employed in the present work. At the outset, an introduction to the basic aspects of the thin film growth processes and deposition technique is provided. Afterward, the characterization techniques like X-ray diffraction (XRD), scanning electron microscopy (SEM), RAMAN spectroscopy and Ultraviolet-visible spectroscopy are discussed.

4.2 Deposition Techniques

Growth techniques do play a solid role in the physical and chemical characteristics of thin films as well as NiO and ZnO metal oxide semiconductors. The structural, electrical, and optical properties of thin films are found to be highly sensitive to the technique adopted and deposition conditions. The appropriate choice of an experimental technique thereby helps in tailoring a material with controlled, reproducible, and well-defined properties to suit a technological application.

4.2.1 Spray pyrolysis

The spray pyrolysis technique has been extensively used to synthesize materials for a wide variety of applications. Spray pyrolysis technique is a low-cost, non-vacuum-required, way to synthesize materials in the form of powders and films.

In the case of films, they are usually deposited over a wide variety of substrates that can be easily adapted for large area deposition and industrial production processes (Falcony et al., 2018). After that, many research articles and review articles (Studenikin et al., 1998; Ukoba et al., 2018) were related to spray pyrolysis processing and the range of thin films (growth of thin-film summarized in table 4.1) deposited by this method for various applications have appeared in the literature.

Table 4.1: Various stages of nucleation and growth of thin films Jilani et al. (2017).

Step	Image
<p>1 Nucleation stage, randomly distributed, three-dimensional nuclei are first formed if the supersaturation condition is fulfilled. These nuclei then grow to form observable islands.</p>	
<p>2 Further deposition increases the size of the islands and often has tendencies to develop crystallographic facets during the early stage of their growth.</p>	
<p>3 When the island distribution reaches a critical state, a rapid large-scale coalescence of islands results. After reaching saturation, the island density decreases with increasing substrate temperature and with subsequent film growth.</p>	
<p>4 Continuous coalescence results in film channels in between. These channels need not remain void and soon some secondary nuclei start to grow within this void space in the channel.</p>	
<p>5 The final stage of growth is a slow process of filling the empty channels that requires a considerable amount of deposit. In an ideal film, there should not be any gap and this stage can be attained when the film has a certain average thickness. The minimum film thickness for the continuous stage is also dependent on the nature of the deposits, deposition parameters.</p>	 

Spray pyrolysis technique (SPT) set-up consists of an atomizer, precursor solution, substrate heater, temperature controller, air compressor, or other sources of carrier gas. Thin-film deposition, using the SPT, involves spraying a metal salt solution (precursor solution) onto a preheated substrate. Droplet's impact on the substrate surface spread into a disk-shaped structure and undergoes thermal decomposition. The shape and size of the disk depend on the momentum and volume of the droplet, as well as the substrate temperature. Consequently, the film is usually composed of overlapping disks of metal salt being converted into oxides on the heated substrate. The surface of the substrate must be

sufficiently hot to initiate a chemical reaction between the precursors in the droplet solution. Specifically, the droplet must still contain enough reactants in solution after reaching the substrate Figure 4.1 showed the schematic representation of a spray set-up which is generally used. Influence of some main spray pyrolysis parameters (temperature - precursor solution-substrate distance on the quality of the deposited films in other words on properties of the deposited films (Barir et al., 2017).

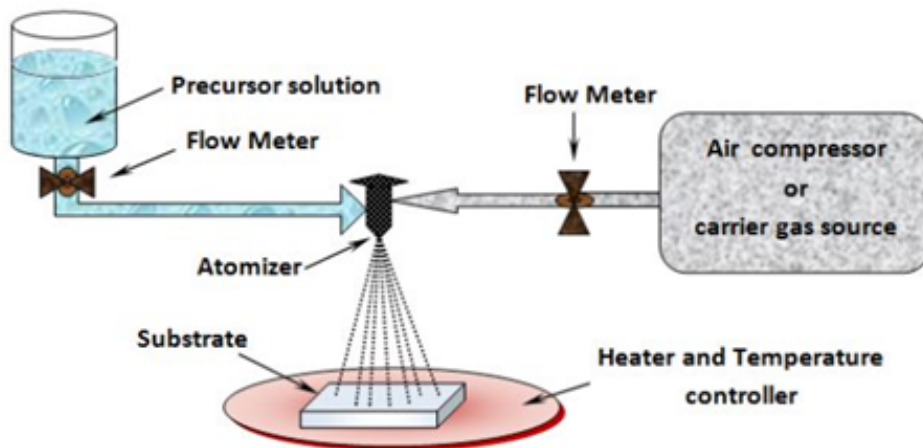


Figure 4.1: Schematic sketch of the chemical spray pyrolysis process.

The spray pyrolysis is useful for the production of thin films of simple oxides and mixed oxides and it has advantages presented in Figure 4.2 . From these, thin films the metal oxide materials prepared by the spray pyrolysis technique have matching properties for a wide variety of potential applications (Ghougali, 2019).

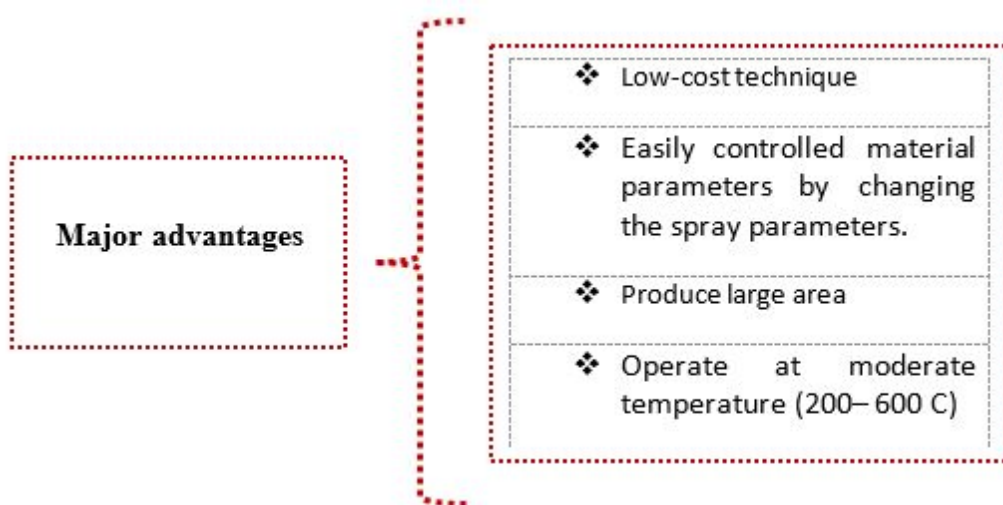


Figure 4.2: Scheme of major advantages of spray pyrolysis techniques for thin film deposition.

4.2.2 Sputtering

Sputtering is a well-established process and can be easily scaled up. The thickness of the coatings can range from nanometres to micrometers and the area is scalable up to a sample size of meters (i.e. for coating of architectural glass) (Schuler, 2008). As shown in Figure 4.3 the sputter target of the material to be sputtered is the cathode of the system and the substrate/substrate holder the anode, which is grounded. Once the vacuum chamber is evacuated to the desired level, a sputtering gas (usually Argon) is introduced.

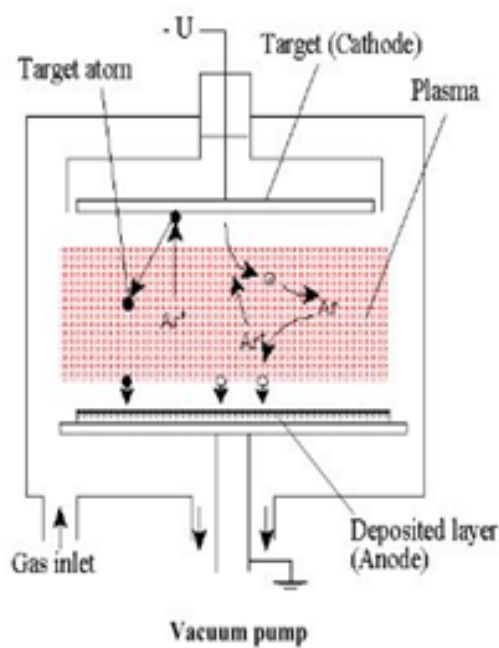


Figure 4.3: Schematic diagram of the sputtering chamber (Schuler, 2008).

The sputtering used in this work is shown in Figures 4.4 and 4.5.



Figure 4.4: Sputtering is used in this work.



Figure 4.5: Sputtering detailed which used in this work.

Reactive sputtering is achieved by adding O_2 to form oxides, H_2 to form hydrogenated material or N_2 to form nitrides. The stoichiometry of the sputtered film can be set by varying the ratio of the introduced gases. Figure 4.6 summarizes how the sputtering deposition works.

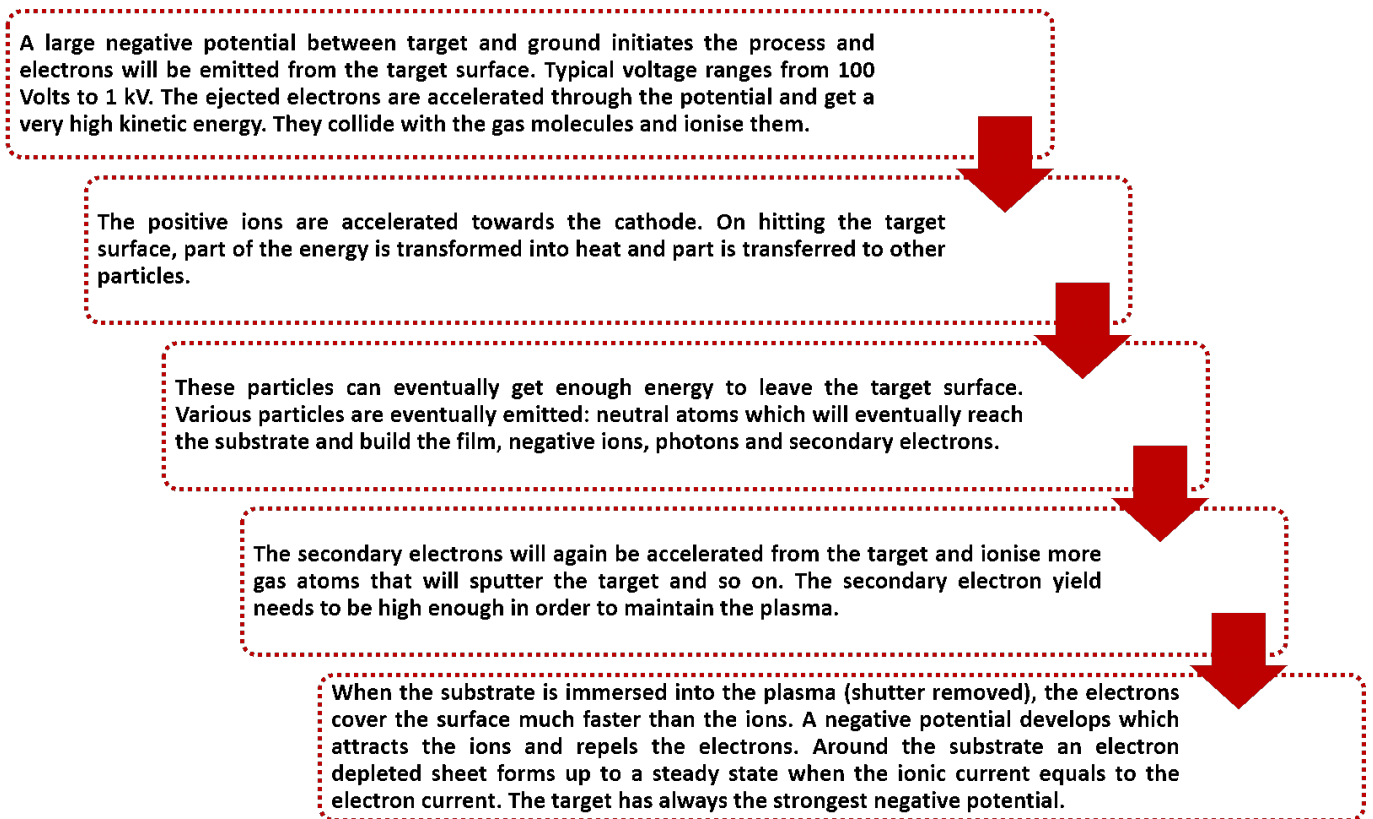


Figure 4.6: Schematic showing how the sputtering deposition works.

The bombardment is a key parameter in the sputtering deposition. It has at least three major effects. It heats the substrate. The temperature of a substrate immersed in plasma will rise to 150 °C (Singh et al., 2007; Anderson et al., 1982). This thermal energy enhances the surface mobility of the atoms and influences the growth of the film. The energy of a bombarding particle can be directly transferred to an atom of the surface through momentum transfer in a collision. It will also increase its mobility, which can lead to sputtering of the atom from the surface (Kappertz et al., 2005). If the energy of the bombarding particle is too high, it can damage the film by the creation of defects during its implantation in the film. The bombardment is also influenced by the nature and pressure of the sputtering gas, the sputtering distance and the sputtering angle. Today most commercial sputtering systems use planar magnetron targets. This technology uses powerful magnets to confine the “glow discharge” plasma to the region closest to the target plate. That vastly improves the deposition rate by maintaining a higher density of ions, which makes the electron/gas molecule collision process much more efficient.

4.3 Characterization techniques

Once the films are grown, the structural, morphological and optical analytical tools give a better understanding of the film behavior and characteristics. On the reverse, these characterization techniques help in optimizing the growth conditions to get device quality films.

4.3.1 Raman Spectroscopy

Raman spectroscopy is a powerful technique in materials research. Material properties can be characterized by using Raman spectroscopy without damaging the sample. Information such as atomic structure, number of layers, type of edge and type of disorder.



Figure 4.7: RAMAN -characterization technique.

4.3.2 X-ray diffraction

XRD is the science of determining the arrangement of the atoms within a crystal from how a beam of X-rays is scattered from the electrons within the crystal. X-ray diffraction (XRD) is a versatile, non-destructive technique used for qualitative and quantitative analysis of crystalline materials. This experimental technique has been used to determine the overall structure of bulk solids, including lattice constants, identification of unknown materials, the orientation of single crystals, the orientation of polycrystalline, stress, strain, texture, films thickness, etc. XRD analysis can provide the crystalline quality and dominant crystallographic planes of the given material. In addition, the diffraction spectrum also provides information regarding the types of phases present in the material and can be used to calculate the approximate average grain size using Scherrer's equation (For more details review this reference (Ungula, 2015)).

In this work, the structural identification of NiO and ZnO is realized by a BRUKER-AXS-8D diffractometer with Cu $K\alpha$ radiation operated at 40 kV and 40 mA in the scanning range of (2θ) between 20° and 80° .

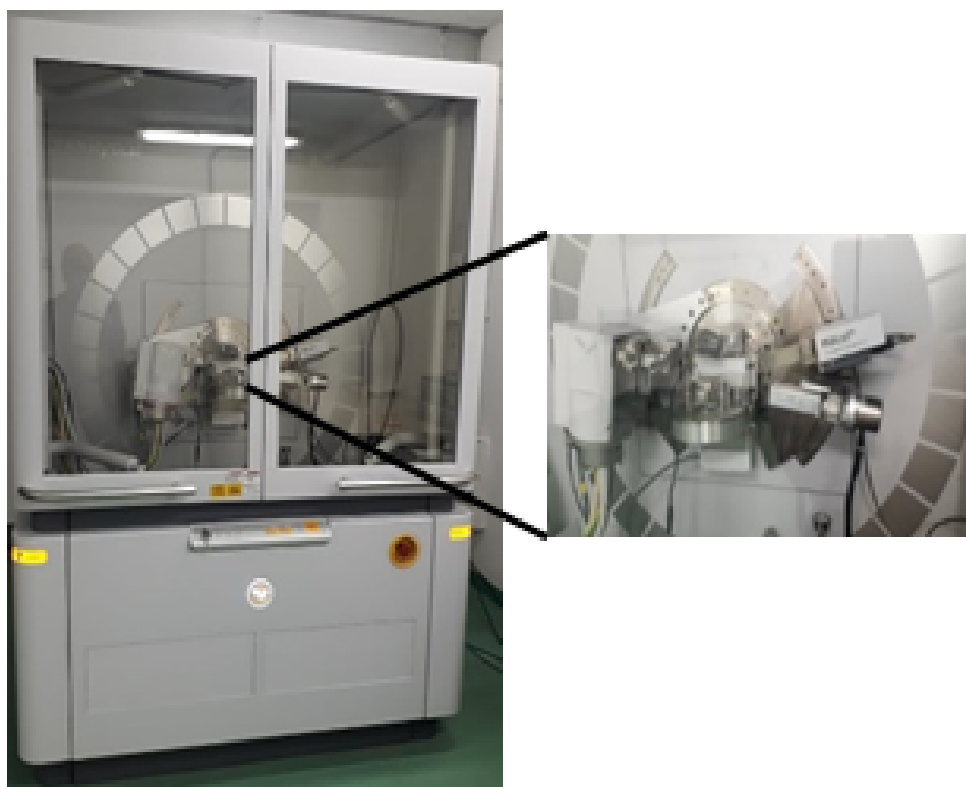


Figure 4.8: XRD -characterization technique.

4.3.3 Scanning Electron Microscope

The shape and morphology of particles are studied by Scanning Electron Microscope (SEM). SEM uses a focused beam of high-energy electrons to generate a variety of signals at the surface of solid specimens. The signals that derive from electrons reveal information about the sample including external morphology (texture), chemical composition and crystalline structure and orientation of materials making up the sample. The beam of electrons is produced and accelerated from an electron source and passed through a series of condenser and objective lenses which focus on the electron beam. A scanning coil moves the beam across the specimen surface. Accelerated electrons carry significant amounts of kinetic energy, and this energy is dissipated as a variety of signals produced by electron-sample interactions when the incident electrons are decelerated in the solid sample equation (For more details review this reference (Ungula, 2015)).

In this work, the surface morphology of the deposited NiO and ZnO thin films was examined using a field emission scanning electron microscopy FE-SEM (Zeiss, Leo1525 Gemini model; Carl Zeiss AG, Oberkochen, Germany) operated at 3-5 kV.

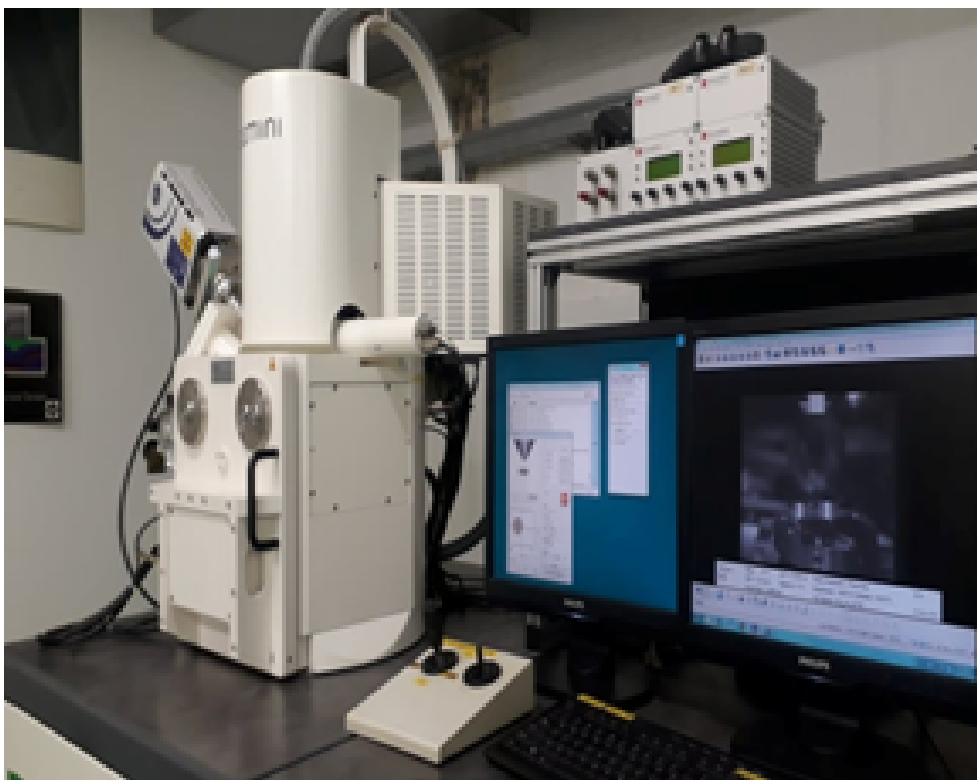


Figure 4.9: SEM -characterization technique

4.3.4 UV-VIS spectroscopy

An instrument used in ultraviolet-visible spectroscopy is called UV/VIS spectrophotometer. The wavelength of UV is shorter than the visible light. It ranges from 100 to 400 nm. In a standard UV-V is a spectrophotometer, a beam of light is split; one half of the beam (the sample beam) is directed through a transparent cell containing a solution of the compound being analyzed, and one half (the reference beam) is directed through an identical cell that does not contain the compound but contains the solvent. The instrument is designed so that it can make a comparison of the intensities of the two beams as it scans over the desired region of the wavelengths. If the compound absorbs light at a particular wavelength, the intensity of the sample beam will be less than that of the reference beam. Absorption of radiation by a sample is measured at various wavelengths and plotted by a recorder to give the spectrum which is a plot of the wavelength of the entire region versus the absorption (A) of light at each wavelength. The bandgap of the sample can be obtained by plotting the graph between (αhv vs hv) and extrapolating it along the x-axis. Ultraviolet and visible spectrometry is almost entirely used for quantitative analysis; that is, the estimation of the amount of a compound known to be present in the sample. The sample is usually examined in solution (For more details review this reference (Ungula, 2015)).

The bandgap was determined by extracting optical transmission and absorption by spectrophotometry using an ultraviolet-visible spectrophotometer (Perkin- Elmer Lambda 25). the UV-Vis system shown in Figure 4.10 was used in this research.



Figure 4.10: UV-VIS -characterization technique.

CHAPTER 5

SIMULATION DETAILS

5.1 Introduction

Silvaco (Silicon Valley Corporation) enables one to design and predict the performance of semiconductor devices based on physics-based simulation. This tool is helpful in modeling the semiconductor device initially before fabricating it. Many companies used Silvaco for many fields. Silvaco, a leading company in the TCAD (Computer-Aided Design) products, has included new physical models which use efficient numerical methods and algorithms, new meshing techniques, optimized linear solvers, etc., which helps in getting the simulation results very close to the practical results. The Thesis considers the Design of a photodiode based on NiO/ZnO heterojunction, we simulate the device in 2D. All along, the simulations are carried out using Silvaco Atlas. Chapter 5 briefly discusses the simulation process.

5.2 ATLAS commands

Simulation of a PV photodiode in ATLAS is made through a text input deck called DeckBuild, a runtime environment in which many different parameters of photodiode structure and composition must be defined. The structure definition comprises a cornerstone for the simulation since it does not only bear the physical dimensions and thicknesses of the different layers constituting the photodiode but also builds a mesh for the photodiode through its fine division. Its significance is that at the grid points, called nodes, a set of differential equations are solved to simulate the transport of the photodiode's carriers and enable the study of the behavior of the photodiode. The composition definition is also important since ATLAS is a physically-based device simulator. Once the physical structures are specified, composition and bias conditions statements lead ATLAS to make predictions of the electrical characteristics of the photodiode (Fotis, 2012).

The buildup consists of a well-defined mesh on which the photodiode is constructed. As shown in Figure 5.1. The simulation's resolution is determined by the density of the mesh's numerous triangles and designates the time needed for program iterations and the accuracy of cell representation. This triangulate mesh is then divided into regions, and different materials are assigned in each of those regions. Then, the electrodes to obtain the electrical characteristics for the device or any region required are assigned. Next, every defined material must be associated with doping, and, as much as possible, material properties must be declared for the most accurate simulation. The next step for the user is to choose among different models, finding which is most suitable for evaluating the structure, and achieving a better outline for the specific photodiode simulation. A specification of a light beam illuminates the photodiode as in real conditions, simulating different regions of the solar spectrum,

depending on the beam chosen. Also, the selection of a method, among the different offered by the ATLAS library, is needed for solving the differential equations through which the photodiode’s operating characteristics arise. These characteristics from the simulation can be saved in a log file and used to create plots using TONYPLOT, the interactive graphics, and the analysis package included in the program.

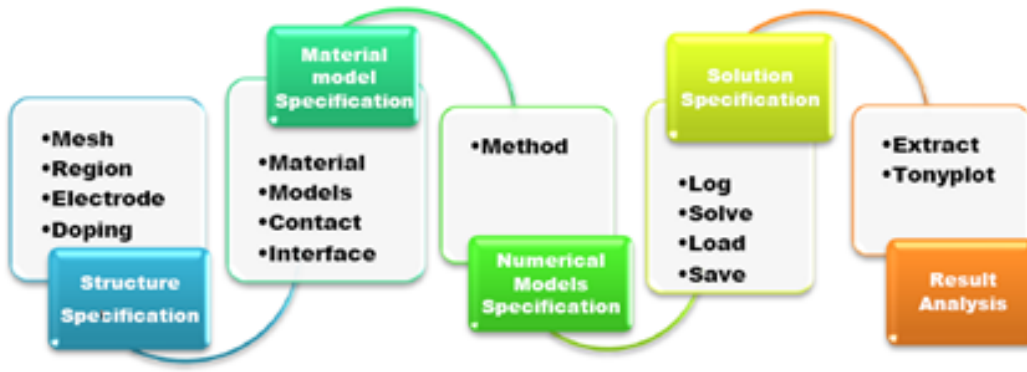


Figure 5.1: ATLAS command groups.

Atlas has several simulators like S-Pisces, Luminous, Mixed Mode, TFT, Laser, Blaze, etc. Virtual Wafer Fab to automate and emulate physical wafer manufacturing. In this project, the Device Simulation is carried out using the ATLAS simulators as shown in Table 5.1.

Table 5.1: Simulators of ATLAS are used for simulation.

Simulator	Using for	Presented as
Blaze	Compound materials	Starting module: BLAZE
TFT	Define defects	Starting module: TFT
Luminous	Illumination	Starting module: LUMINOUS

5.3 Model description

5.3.1 Basic carrier transport equations

Semiconductor equations are solved by the ATLAS simulator for the analysis of device performance. These equations which are solved by any general-purpose device simulator, have been derived from Maxwell’s laws and consist of Poisson’s equation, continuity equations, and the transport equations.

Poisson's equation relates variations in the electrostatic potential to local charge densities and the continuity and transport equations describe the electron and hole densities that evolve as a result of transport processes, generation processes, and recombination processes. Poisson's Equation relates the electrostatic potential to the space charge density:

$$\text{div}(\varepsilon \nabla \psi) = -\rho \quad (5.1)$$

The continuity equations for electrons and holes are defined as:

$$\frac{\partial n}{\partial t} = \frac{1}{q} \text{div} \vec{j}_n + G_n - R_n \quad (5.2)$$

$$\frac{\partial p}{\partial t} = \frac{1}{q} \text{div} \vec{j}_p + G_p - R_p \quad (5.3)$$

where q is magnitude of the charge on an electron, n and p are electron and hole concentrations, respectively, J_n and J_p are electron and hole current densities, respectively, G_n and G_p are generation rate of electron and holes, respectively, R_n and R_p are recombination rates for electrons and holes, respectively.

Equations 5.1, 5.2 and 5.3 provide the general framework for device simulation. In addition, secondary equations are needed to specify particular physical models for J_n , J_p , G_n , R_n , G_p , and R_p . The current density equations, or charge transport models, are usually obtained by applying approximations and simplifications to the Boltzmann Transport Equation. Different transport models such as the drift-diffusion model, the energy balance model, or the hydrodynamic model have been developed due to these assumptions. The choice of the charge transport model will then have a major influence on the choice of generation and recombination models.

Drift diffusion is the simplest model and has the attractive feature that it does not introduce any independent variables in addition to ψ , n , and p . The drift-diffusion model was once adequate for nearly all devices that were technologically feasible. However, the drift-diffusion approximation becomes less accurate for smaller feature sizes.

5.3.2 Carrier recombination

Semiconductor materials exhibit crystal flaws, which can be caused by dangling bonds at interfaces or by the presence of impurities in the substrate. The presence of these defect centers, or traps, in semiconductor substrates may significantly influence the electrical characteristics of the device.

Recombination through defect levels in semiconductors is usually described by the Shockley–Read–Hall

theory.

$$\begin{aligned}
\int_a^b R_{n,p} = \int_{E_v}^{E_c} & \left(\frac{v \text{SIGTAE} \text{SIGTAH} (np - n^2) g_{TA}(E)}{v_n \text{SIGTAE} (n + n_i \exp[\frac{E - E_i}{KT}]) + v_p \text{SIGTAH} (p + n_i \exp[\frac{E_i - E}{KT}])} \right. \\
& + \frac{v_p v_n \text{SIGTAE} \text{SIGGAH} (np - n^2) g_{GA}(E)}{v_n \text{SIGTAE} n + n_i \exp[\frac{E - E_i}{KT}] + v_p \text{SIGTAH} (p + n_i \exp[\frac{E_i - E}{KT}])} \\
& + \frac{v_p v_n \text{SIGTDE} \text{SIGTDH} (np - n^2) g_{TD}(E)}{V_n \text{SIGTDE} (n + n_i \exp[\frac{E - E_i}{KT}]) + v_p \text{SIGTDH} (p + n_i [\frac{E_i - E}{KT}])} \\
& \left. + \frac{v_p v_n \text{SIGGDE} \text{SIGGDH} (np - n^2) g_{GD}(E)}{v_n \text{SIGGDE} (n + n_i \exp[\frac{E - E_i}{KT}]) + v_p \text{SIGGDH} (p + n_i \exp[\frac{E_i - E}{KT}])} \right) dE
\end{aligned} \tag{5.4}$$

where v_n is the electron thermal velocity and v_p is the hole thermal velocity, n_i is the intrinsic carrier concentration. SIGTAE and SIGGAE are the electron capture cross-section for the acceptor tail and Gaussian states respectively. SIGTAH and SIGGAH are the hole capture cross-sections for the acceptor tail and Gaussian states respectively and SIGTDE, SIGGDE, SIGGDH, and SIGGDH are the equivalents for donors states.

The density of states (DOS) is described by its conduction and valence band edge intercept densities tail bands (a donor-like valence band and an acceptor-like conduction band) (NTA and NTD), and by its characteristic decay energy (WTA and WTD). For Gaussian distributions, its total density of states deep level bands (one acceptor-like and the other donor-like) (NGA and NGD), its characteristic decay energy (WGA and WGD), and its peak energy distribution (EGA and EGD) which are modeled using a Gaussian distribution.

$$g(E) = g_{TA}(E) + g_{TD}(E) + g_{GA}(E) + g_{GD}(E) \tag{5.5}$$

$$g(E) = N_{TA} \exp\left(\frac{E - E_c}{WTA}\right) + N_{TD} \exp\left(\frac{E_v - E}{WTD}\right) + N_{GA} \exp\left(-\left(\frac{E_{GA} - E}{WGA}\right)^2\right) + N_{GD} \exp\left(-\left(\frac{E - E_{GD}}{WGD}\right)^2\right) \tag{5.6}$$

Here, E is the trap energy, EC is the conduction band energy, EV is the valence band energy and the subscripts (T, G,A, D) stand for tail, Gaussian (deep level), acceptor and donor states respectively.

Recombination through trap states is also known as the Shockley-Read-Hall recombination. Electrons are relaxing from the conduction band to trap levels in the bandgap and then to the valence band. This two-step transition involves a lower energy release than the direct transition. The excess energy is transferred to lattice vibrations (phonons). A large difference between band edges and the trap state level (E_t) leads to barely zero-emission of carriers.

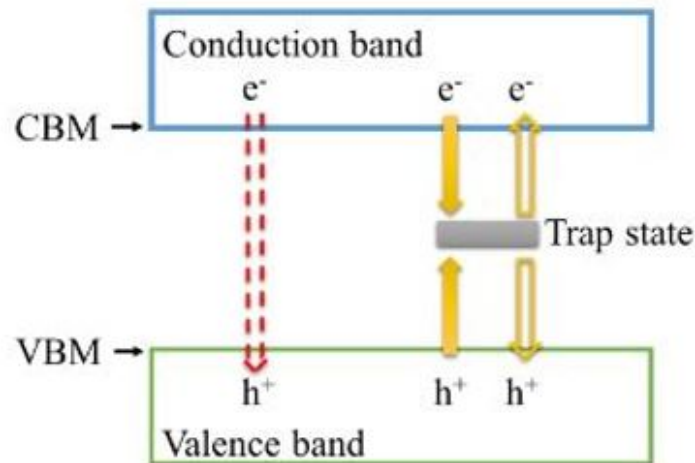


Figure 5.2: Schematic recombination transition.

Band to band radiative recombination is indicated by a red dash open arrow. The transitions related to carrier captured and emitted by trap states are indicated by gold solid and open arrows, respectively. CBM is a short name for conduction band minimum and VBM is a short name for valence band maximum (Huang, 2018). Trap centers, whose associated energy lies in a forbidden gap, exchange charge with the conduction and valence bands through the emission and capture of electrons. The trap centers influence the density of space charge in semiconductor bulk and the recombination statistics. Device physics has established the existence of three different mechanisms, which add to the space charge term in Poissons's equation in addition to the ionized donor and acceptor impurities. These are interface fixed charge, interface trap states and bulk trap states. Interface fixed charge is modeled as a sheet of charge at the interface and therefore is controlled by the interface boundary condition. Interface traps and bulk traps will add space charge directly into the right-hand side of Poisson's equation (Atlas, 2005).

A donor-type trap can be either positive or neutral like a donor dopant. An acceptor-type trap can be either negative or neutral like an acceptor dopant. A donor-like trap is positively charged (ionized) when empty and neutral when filled (with an electron). An empty donor type trap, which is positive, can capture an electron or emit a hole. A filled donor-type trap, which is neutral, can emit an electron or capture a hole. An acceptor-like trap is neutral when empty and negatively charged (ionized) when filled (with an electron). A filled acceptor-like trap can emit an electron or capture a hole. An empty acceptor-like trap can capture an electron or emit a hole. Unlike donors, donor-like traps usually lie near the valence band. Likewise, acceptor-like traps usually lie near the conduction band (Atlas, 2005).

5.3.3 Thermionic emission and tunneling transport models

Thermionic emission dominated current in abrupt heterojunctions. It applies only at the node points along with the interface of the heterojunction. To enable the thermionic transport model, you must specify THERMIONIC on the INTERFACE statement. You must also set the S.S parameter on the INTERFACE statement to indicate that the model applies to semiconductor-semiconductor interfaces (Atlas, 2005).

Extra carriers can be injected into the devices under bias. In the Silvaco code, the boundary conditions for the band alignment depend on the external bias (Huang, 2018).

5.4 Carrier generation

Extra carriers can be injected into the devices under bias. In the Silvaco code, the boundary conditions for the band alignment depend on the external bias. Above bandgap light shining on the surface of a semiconductor leads to the generation of electron-hole pairs, affecting strongly the minority carrier concentration and the band alignment (Huang, 2018). The optical properties are generally characterized by the absorption spectrum of the complex refractive index. One might notice that the absorption properties of a semiconductor critically affect the photodiode design, such as its thickness, the direction of illumination. In the Silvaco code, the photoinduced carrier generation is calculated according to the refractive index, which is important in the design of optical components for spectral dispersion applications. It reflects the crystallinity and optical quality of thin films. n and k represent the real and imaginary parts of the complex refractive index respectively.

TCAD device modelling and Simulation of Wide Bandgap NiO/ZnO heterojunctions Semiconductors details and conditions used in this work. and their parameters, creating the finite elements and geometry and simulation of device characteristics. The photodetectors have been obtained using BLAZE, TFT, LUMINOUS tool of ALTAS device simulator. Thermionic emission and tunneling dominated current in abrupt heterojunctions and to accurately model devices made of polycrystalline materials, use a continuous density of states. Due to lattice mismatch at the hetero-interface NiO/ZnO, trap states have formed that act as recombination centers for electrons and holes Furthermore There are not only the recombination at the bulk that is taken into consideration but also interface traps recombination is taken into consideration.

5.5 Design process of NiO/ZnO heterojunction photodiode

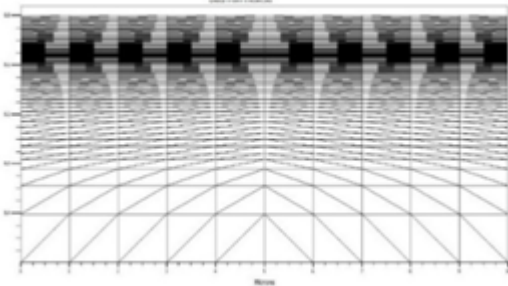
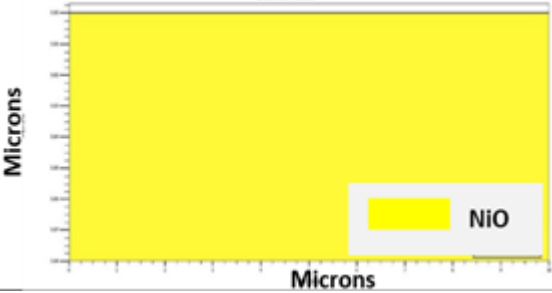
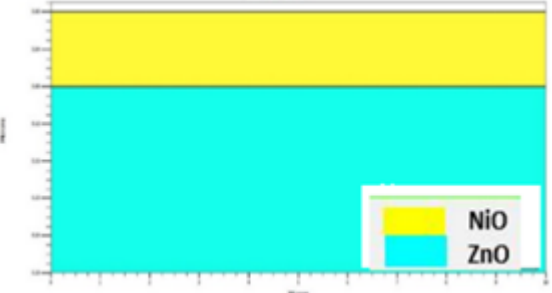
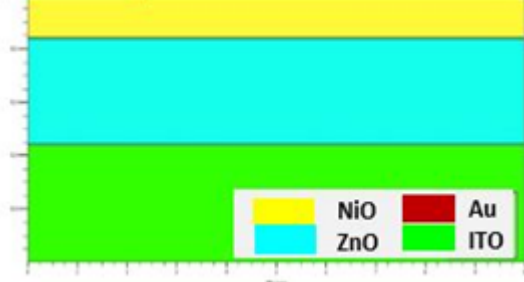
structure specification	Plot
<p>Mesh: At the horizontal or x-line, the line has been set up to be denser at the right of the structure with the space of 0.025 microns. This region will be the critical region of the device, where the flow of current is. At the vertical or y-line, almost an even mesh is created. A non-uniform mesh, where the grid is finer around the interface, was defined to obtain good accuracy with a reasonable calculation time.</p>	
<p>Region 1: To obtain the heterojunction; The NiO layer is used as the top and transparent layer. Here, a thin layer of NiO of thickness less than 84 nm is desired. “ region num=1 user.material=NiO y.min=0.00 y.max=0.084 ” Note that the NiO is definite a new material in SILVACO TCAD.</p>	
<p>Region 2 : The next step is to add the ZnO layer, “region num=2 material=ZnO y.min=0.084 y.max=0.294 “</p>	
<p>Electrodes : Use Gold and ITO as conductor layer by definite the work function of each one elec num=1 name=anode x.min=0 x.max=2 material=Gold elec num=2 name=cathode y.min=0.294 y.max=0.5 material=ITO.</p>	

Table 5.2: Basic steps to design a NiO/ZnO heterojunction photodiode with the simulator ATLAS.

CHAPTER 6

RESULTS AND DISCUSSION

6.1 Introduction

The past decade has seen significant progress toward understanding how the various material parameters and impact of the optoelectronic properties of ZnO and NiO materials and consequently device performance. Analysis of the structure design and the interface between its components also are expected to have a dominant role in photodetector optimization (Steirer et al., 2017). The NiO/ZnO heterojunction interface is a common condition that has a considerable impact on UV photodetection. Up to now, few studies have investigated the energy level alignment and the interface between the two different metal oxides. This chapter has three studies. First, we aim to study the effect of the source solution quantity on structural and optical characteristics of ZnO and NiO thin films grown by spray pyrolysis for the design of NiO/ ZnO photodiode. We performed numerical simulation with the use of Silvaco ATLAS software to simulate the NiO/ZnO photodiode and clarify the effects of different material parameters (tail and Gaussian states in NiO and ZnO thin films) on device performance. Secondly study based on a study of the NiO/ZnO heterojunction structural, morphological, optical properties. By using the experimental parameters in simulations, We have studied the effect of the traps at of NiO/ZnO hetero-interface. The performance of the NiO/ZnO heterojunction photodetector is very sensitive to interface traps. Therefore, understanding the role of the interface traps at the NiO/ZnO heterojunctions is useful to enhance the design of the photodiode. In third work, we have used RF sputtering to prepare NiO, ZnO thin films and NiO/ZnO heterojunction under vacuum conditions. We have used detailed structural, morphological analysis as well as optical measurements to characterize the thin films and the heterojunction.

6.2 Effect of the source solution quantity on ZnO and NiO thin films

In our work, chemical spray pyrolysis technique has been chosen for the preparation of NiO, ZnO thin films at different source solution quantities (5, 10 and 15 ml) deposited on glass substrates. Structural aspects of the deposited films were characterized using X-ray diffraction (XRD). The optical properties were characterized using a UV-Visible spectrometer by recording the transmittance and reflectance spectra.

Using Nickel nitrate hexahydrate 98% with different solution quantities. NiO solution was prepared by dissolving ($Ni(NO_3)_2 \cdot 6H_2O$) in the solvent containing equal volume of methanol solution (CH_3OH) (99.995%) purity. Then added a drop of chloride acid as a stabilizer. The mixture solution was stirred and heated at 60 °C for 2 h to yield a clear and transparent solution. Figure 6.1 showed the preparation procedure of NiO thin films.

Using zinc acetate dehydrate with different solution quantities. ZnO solution was prepared by dissolving ($Zn(CH_3COO)_2 \cdot 2H_2O$) in the solvent containing equal volume of methanol solution (CH_3OH) (99.995%) purity. Then added a drop of chloride acid as a stabilizer. The mixture solution was stirred and heated at 60 °C for 2 h to yield a clear and transparent solution. The glass substrates were cleaned by detergent and by alcohol mixed with deionized water.

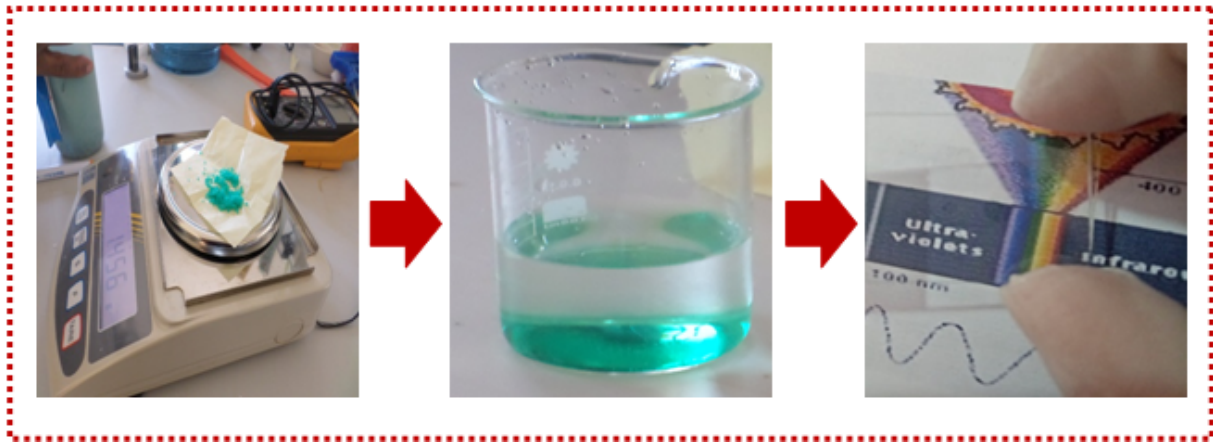


Figure 6.1: The preparation procedure of NiO thin films by spray pyrolysis deposition.

Table 6.1 summarized the pyrolysis deposition conditions for the preparation of NiO and ZnO thin films.

Table 6.1: Spray pyrolysis deposition conditions for the preparation of NiO and ZnO thin films.

Spray conditions	Values
Solution concentration	0.15 mol/l
Spray rate	1.5 ml/min
Nozzle to substrate distance	53 cm
Temperature substrate	350 °C
Three different quantities of solution	5 , 10 and 15 ml

6.2.1 Structural properties of NiO and ZnO thin films

The X-ray diffraction (XRD) technique was employed to illustrate the NiO and ZnO phases' appearance, and to determine the structural parameters such as crystallite size, dislocation density, and microstrain. Figure 6.2 shows the X-ray diffraction patterns of both ZnO and NiO thin films deposited on glass substrates using different quantities of solution.

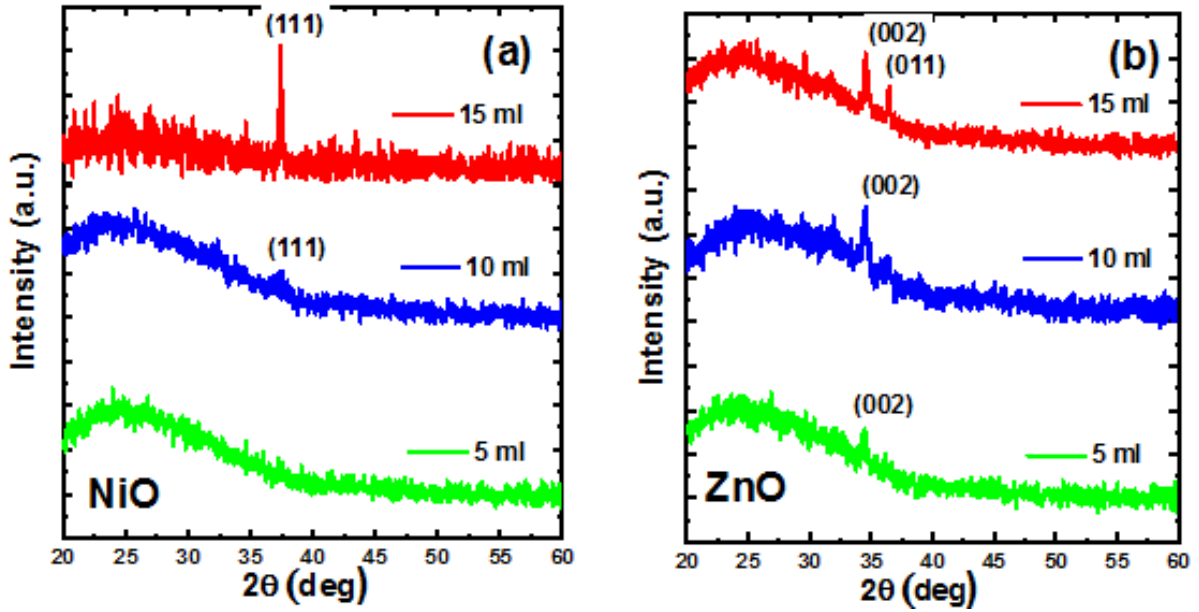


Figure 6.2: XRD patterns of (a) NiO and (b) ZnO thin films using different quantities of solution.

The patterns show clearly the impact of the quantity of solution on the crystalline behavior of the films. In fact, (5ml) poor crystallinity for ZnO and the formation of amorphous structure for NiO at low spray quantities. While the crystalline structure of both films has been improved at high quantity of solution (15ml) which indicates that the quality of the films has been enhanced by extending the crystallinity. The peaks that appeared of the deposited films match exactly the standards JCPDS (98-008-1558) and JCPDS (No.04-0835) of ZnO and NiO, respectively. They represent pure ZnO and NiO without impurities belong to the ZnO hexagonal wurtzite and cubic structures, respectively. The ZnO patterns show the polycrystalline structure due to the presence of peaks such as (002) and (101) situated at 34.57 and 36.44 °, respectively. While only one most intense peak (111) was observed for NiO. From both patterns, we can indicate that plan (002) is the most intense plan for ZnO and (111) for NiO, which indicates that most crystallites are preferably oriented towards those plans. Microstructural parameters such as crystallite size (D) dislocation density (δ) and microstrain (ε) were calculated using Equations 6.1, 6.2 and 6.3 (see Table 6.2).

$$D = \frac{0.94\lambda}{\beta \cos \theta} \quad (6.1)$$

$$\delta = \frac{1}{D^2} \quad (6.2)$$

$$\varepsilon = \frac{\beta \cos \theta}{4} \quad (6.3)$$

Where θ is Bragg's angle, β is the Full Width at Half-Maximum intensity (FWHM) and λ (1.5406 Å) is the wavelength of the x-ray diffractometer.

Table 6.2: Microstructural parameters of NiO and ZnO thin films.

Material	(hkl)	2theta (degree)	Crystallite size (nm)	Dislocation density ($10^{14}/m^2$)	Micro strain (10^{-2})
NiO	(111)	31.78	43,81	5.21	4.73
ZnO	(002)	34.57	31.05	1.03	6.68
	(011)	36.44	72.82	1.91	2.84

6.2.2 Optical properties

6.2.2.1 Transmittance

Figure 6.3 presented the optical transmission of (a) NiO and (b) ZnO thin films as a function of the wavelength in the 250–900 nm range for different sprayed solution quantities 5,10 and 15 ml.

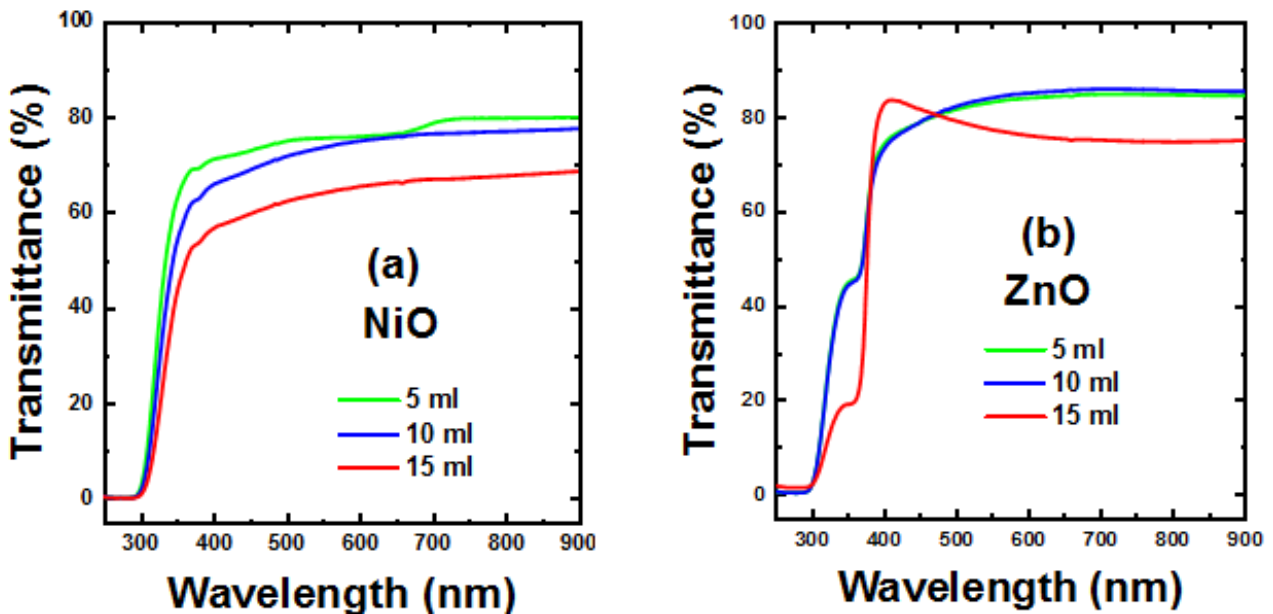


Figure 6.3: Transmittance spectra of (a) NiO and (b) ZnO thin films at different quantities of solution.

NiO shows good transmittance in the visible region. When it is rich 79%, 5 ml and 10 ml do not show a big difference While 15 ml Shows dropping in transmittance, were decreased by 18% compared to previous NiO thin films. On the other hand, ZnO shows high transparency in the visible region. The transmission is over 85% for ZnO of 5 and 10 ml approximately equal and decreases by 9% for 15ml.

6.2.2.2 Reflectance

The reflection of light at a surface is an important factor to know the absorption of photons in semiconductor materials. The reflectance curves are is presented in Figure 6.4 for (a) NiO and (b) ZnO as

a function of the wavelength in 250–900 nm range for different sprayed solution quantities.

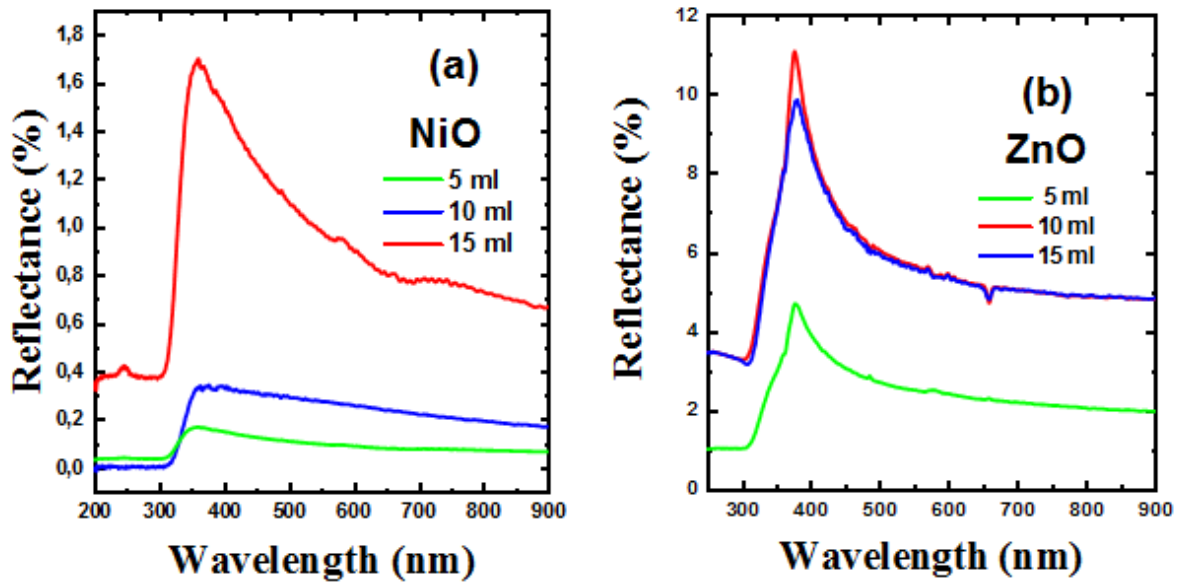


Figure 6.4: Reflectance spectra of deposited (a) NiO and (b) ZnO thin films for different quantities of solution.

NiO is more affected than ZnO with the increased quantities of solution. As we can see in Figure 6.4, NiO shows low reflectance. For 5, and 10 ml do not show a big difference which the values is over 0.3 % and 0.6 % respectively, while 15 ml Shows rising in reflectance, were increased three times more than 5 and 10 ml thin films. The reflectance of ZnO is over 4.8 % for 5 ml, while 10 and 15 ml do not show a difference in reflectance.

6.2.2.3 Absorption coefficient

The absorption coefficient $\alpha(\lambda)$ spectra can be used to estimate the optical bandgap of the deposited thin films. It is calculated by Equation 6.4, (Chala et al., 2018).

$$\alpha(\lambda) = -\frac{1}{d} \ln \left[\frac{T(\lambda)}{(1 - R(\lambda))^2} \right] \quad (6.4)$$

where d is the sample thickness, T and R are the transmittance and reflectance respectively. The thicknesses of NiO and ZnO films were estimated. The values, listed in Table 6.3, show the increment of the film's thickness with the elevation of quantity of solution as expected.

Table 6.3: The thickness as a function of quantities of solution for NiO and ZnO thin films

Quantities of solution(ml)	Thickness (nm)	
	NiO	ZnO
5	30	75
10	60	130
15	84	210

The evaluated $\alpha(\lambda)$ is shown in Figure 6.5 for (a) NiO and (b) ZnO films for different quantities of solution.

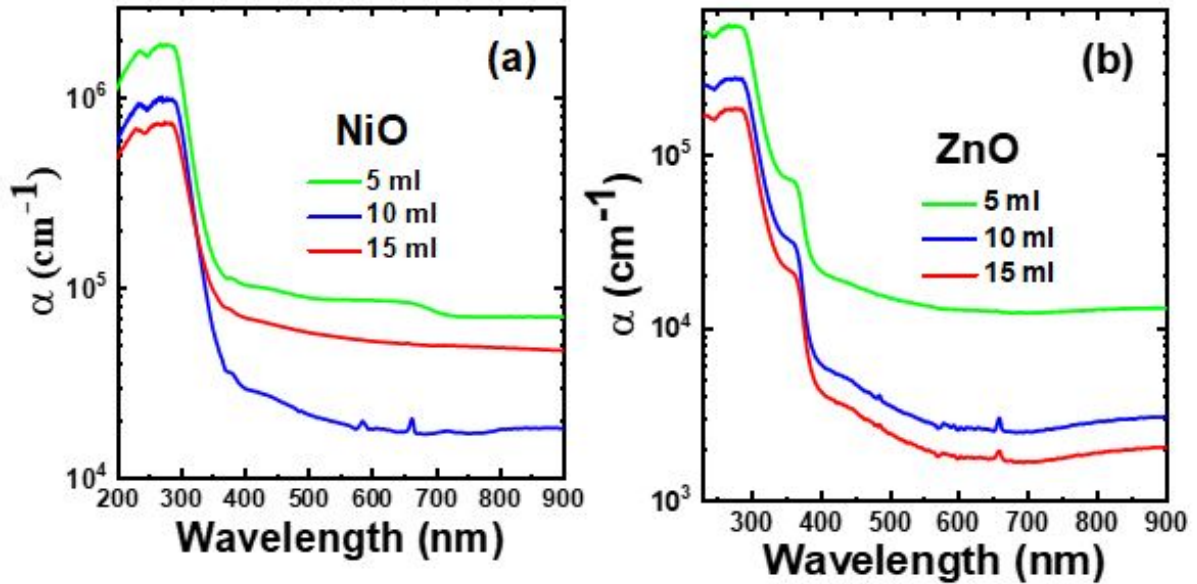


Figure 6.5: Absorption coefficient of deposited (a) NiO and (b) ZnO thin films for different quantities of solution.

The absorption coefficients of ZnO and NiO films decrease monotonically when the wavelength increases, the absorption decreasing with the increase in quantities of solution. However, NiO and ZnO at 15 ml show a high absorption coefficient in the UV range.

6.2.2.4 Extraction of optical bandgap

The optical band gap (E_g) of the films was estimated from the plots of $(\alpha h\nu)^2$ versus photon energy ($h\nu$) using Tauc's relation. According to Tauc's formula for direct bandgap semiconductor as (Hwang et al., 2017):

$$(\alpha h\nu)^2 = A(h\nu - E_g) \quad (6.5)$$

Where A is a constant, h is plank's constant, ν is the incident photon frequency, E_g is the energy bandgap and α is the absorption coefficient.

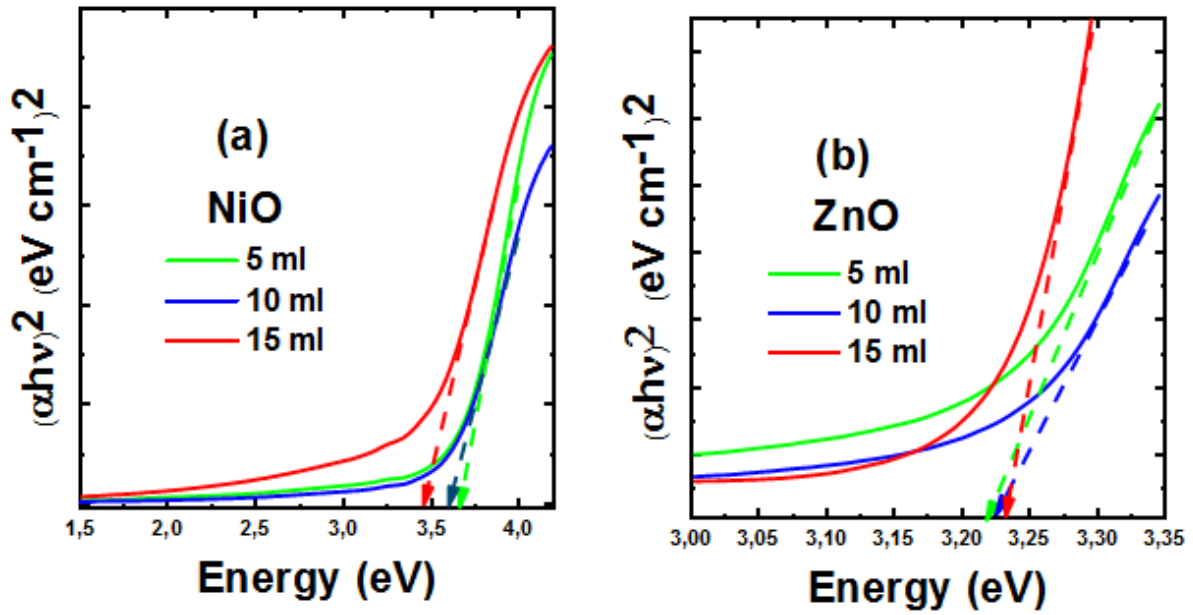


Figure 6.6: Variation of $(\alpha h\nu)^2$ versus photon energy of deposited (a) NiO and (b) ZnO thin film for different quantities of solution showing the extracted energy gap.

As shown in Figure 6.6, the bandgap of NiO thin films decreases as the quantities of solution increase from 3.66, 3.6 to 3.45 eV. Concerning ZnO films, as solution quantities increase, the optical bandgap increases marginally from 3.21, 3.22 to 3.23 eV.

6.2.2.5 Refractive Index and Extinction coefficient

The refractive index of the film has significant importance in the design of optical components for spectral dispersion applications. It reflects the crystallinity and optical quality of thin films. Refractive index (n) and extinction coefficient (k) represent the real and imaginary parts of the complex refractive index respectively. The extracted n and k are presented in Figure 6.7 for NiO and ZnO films. They were calculated by using Equation 6.5, 6.6 and 6.7 (Chala et al., 2018):

$$k(\lambda) = \frac{\alpha(\lambda)\lambda}{4\pi} \quad (6.6)$$

$$n(\lambda) = \frac{(1 - R(\lambda))}{(1 + R(\lambda))} + \sqrt{\frac{4R(\lambda)}{1 - R(\lambda)^2} - k(\lambda)^2} \quad (6.7)$$

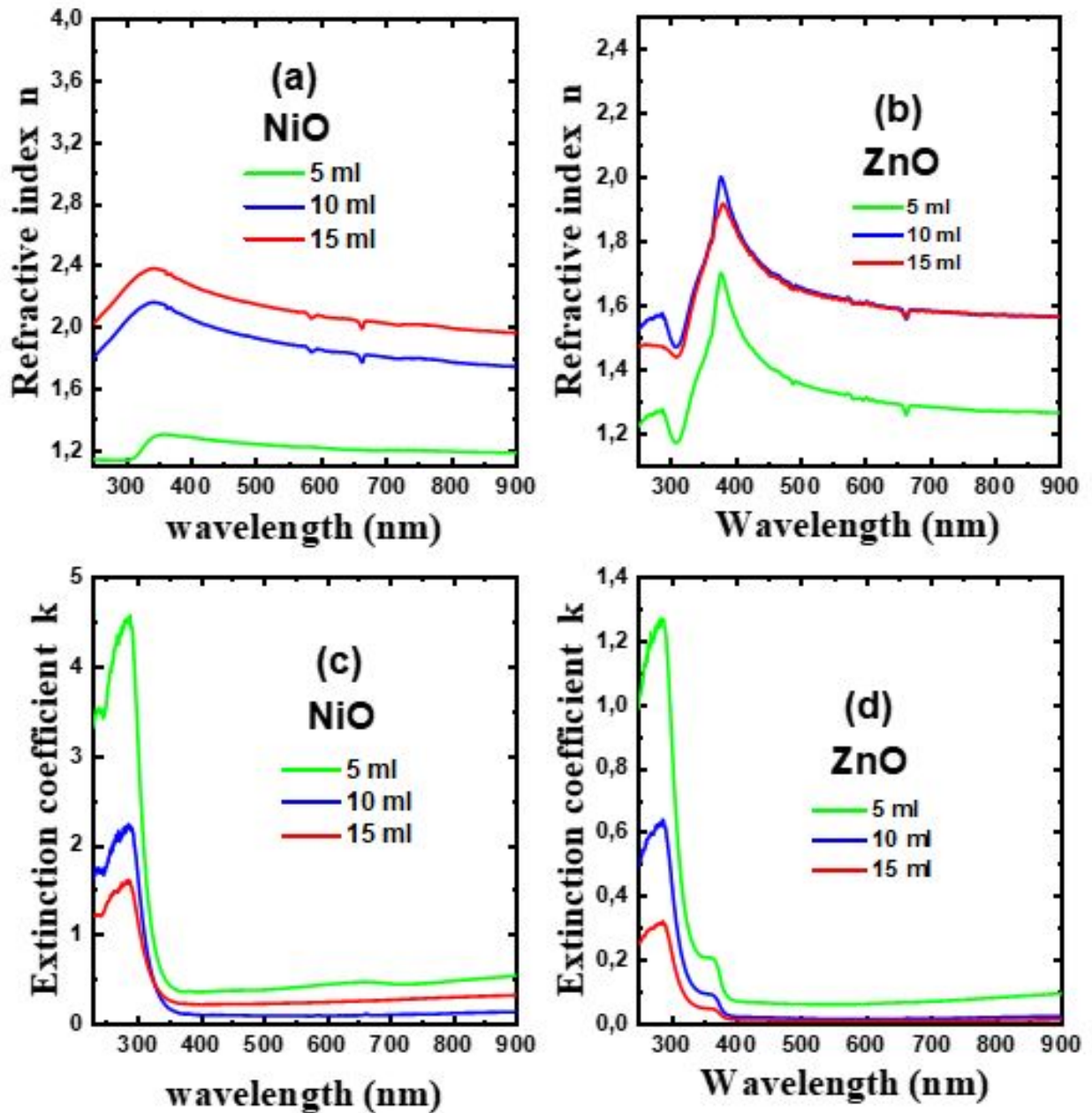


Figure 6.7: The extracted optical parameters of NiO and ZnO, (a) and (b) refractive index (n) and (c) and (d) extinction coefficient (k) for different quantities of solution.

As can be seen from Figure 6.7, the refractive index values increased from 1.4 to 2.4 for the NiO and for ZnO from 1.6 to 2 with increasing of solution quantities. It is seen also that the extinction coefficient decreases with an increase in wavelength and it is minimum in visible wavelength region which explains the transparent property of NiO and ZnO prepared films.

Eg, d, n and k determined from experimental results are used in simulation under dark and illumination conditions to evaluate the I-V characteristics and the responsivity of the photodiode.

6.3 Effect of material properties on design of a NiO/ZnO heterojunction photodiode

Using the software Silvaco TCAD, the simulation aims to understand the relationship between NiO and ZnO thin films properties and NiO/ZnO photodiode performance. Results are generated by numerical simulation of the studied photodiode at different quantity of solution by changing the experimental parameters. Then, we investigated the effects of tail and gaussian defect density in NiO and ZnO on photodiode performance (I-V characteristics and responsivity).

6.3.1 Device structure

The proposed NiO/ZnO photodiode structure is shown in Figure 6.8. It consists, from bottom to top, of an ITO conductive layer, followed by an n-type ZnO layer and a p-type NiO. The anode contact is made of gold (Au). The photodiode is illuminated from the p-side of the structure. The parameters of each material used to simulate NiO/ZnO photodiode are presented in Table 6.4.

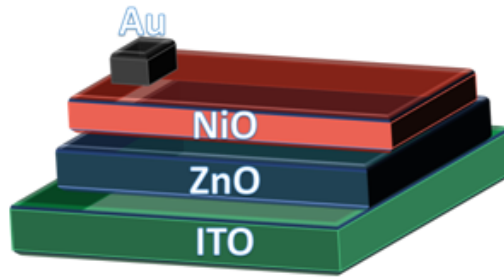


Figure 6.8: Simulated NiO/ZnO heterojunction photodiode structure.

Table 6.4: Basic structure design parameters (Elseman et al., 2018; Chala et al., 2018).

Parameters	Units	ZnO	NiO
Electron affinity	eV	4.6	1.64
Effective density of states, (NC)	cm^{-3}	2.2×10^{18}	1.6×10^{19}
Effective density of states, (NV)	cm^{-3}	1.8×10^{19}	1.1×10^{19}
Dielectric constant	-	9	11
Electron and hole Mobility	$cm^2/V.s$	10/5	0.1/0.53

6.3.2 Electrical characteristics

The photodiode is illuminated with 3 mW.cm^{-2} of optical power density at a 365 nm wavelength. Figure 6.9 (a), (b), and (c) show the variation of the I–V characteristics under illumination as a function of the quantities of solution of NiO, ZnO, and for the two materials together respectively.

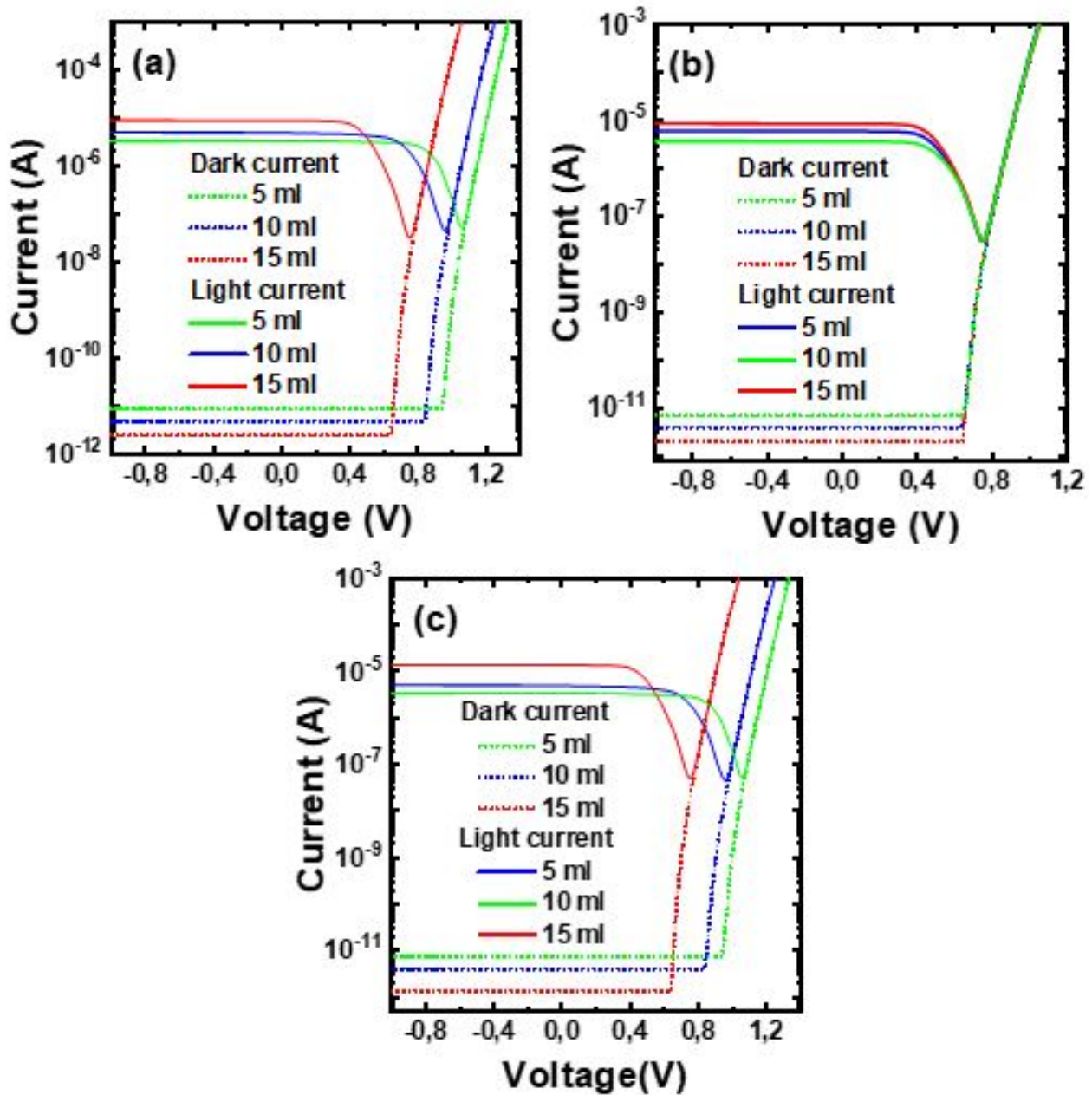


Figure 6.9: Dark and light I–V characteristics of NiO/ZnO heterojunction photodiode for different solutions of (a) NiO, (b) ZnO, and (c) NiO and ZnO together.

The first observation is that as the quantities of solution increase the photogenerated current increases which confirm high photodetection and the dark current is decreasing due to reduce the generate current. The second observation is that the parameters of NiO have a more pronounced effect on the

I-V characteristics than those of ZnO although its thickness is smaller especially the turn-on voltage which rises with decreasing quantity of solution for NiO thin films. This may be due to the decrease in the bandgap of NiO. The thickness and optical parameters bandgap, n and k parameters have an impact on the I-V characteristics of NiO/ZnO heterojunction device.

6.3.3 Optical response characteristics

Figure 6.10 (a), (b), and (c) show the variation of the responsivity under illumination as a function of the quantities of solution of NiO, ZnO, and for the two materials together respectively. The device is illuminated with 3 mW.cm^{-2} of optical power density at a 365 nm wavelength at a reverse bias of 0.5 V.

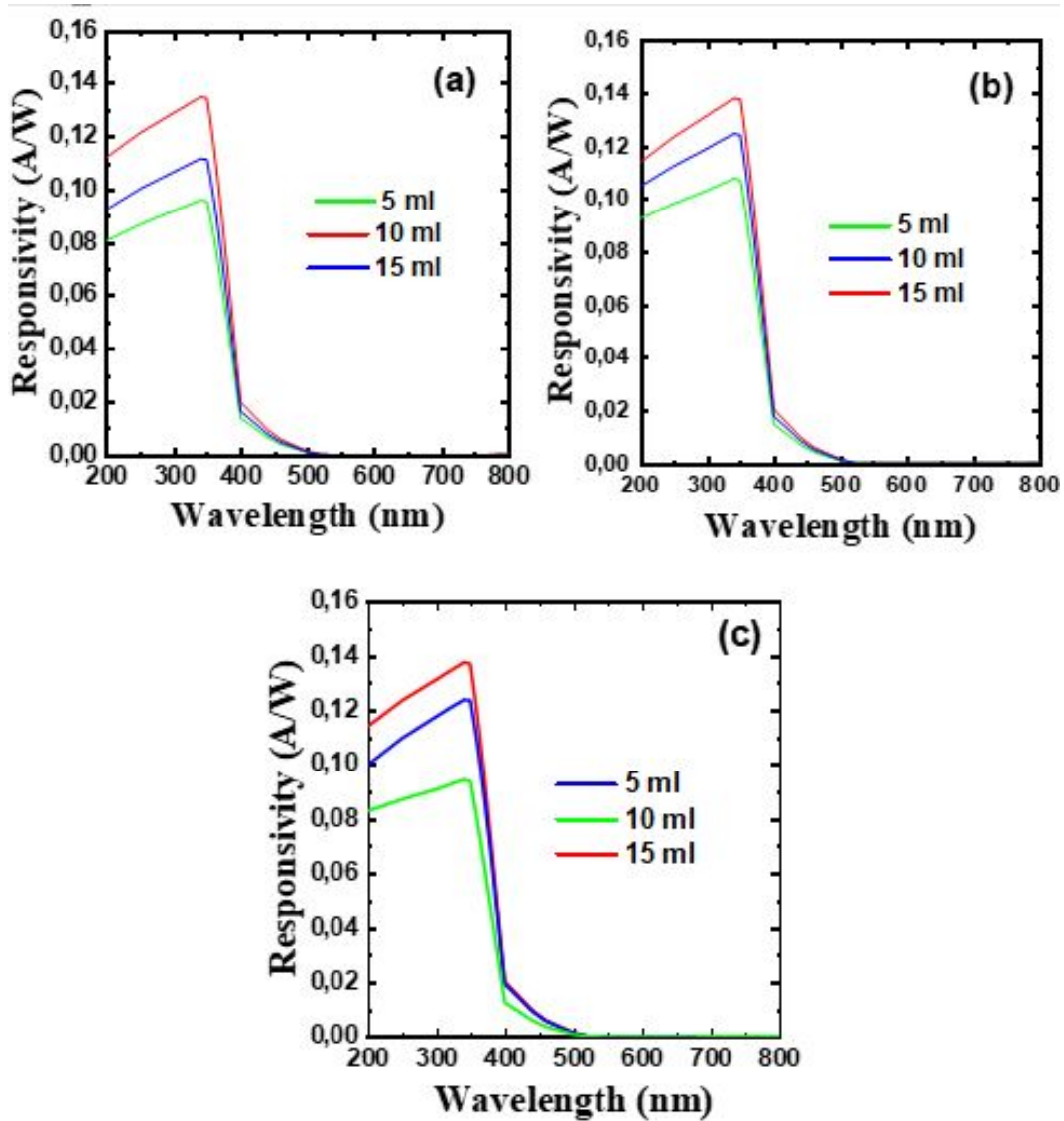


Figure 6.10: Responsivity of NiO/ZnO heterojunction photodiode for different quantities of solution of (a) NiO, (b) ZnO and (c) that of NiO and ZnO together.

It has been observed that as quantities of solution of the ZnO layer increase, the responsivity also increases. It can also be seen that the effects converge in all cases (a), (b) and (c) which proves how important it is to choose both materials NiO and ZnO to obtain high responsivity. The simulated responsivity has been compared with previously reported findings.

The simulated results are a bit less than experimental results as reported in Table 6.5. This may be due to the fact that the structure is not exactly the same (as carrier concentration) or some other effects that are not taken into account in the simulation such as defects.

Table 6.5: Comparative responsivity of different structures to NiO/ZnO heterostructure photodiode.

Structure Device	Conditions			Responsivity (A/W)	Ref
	Voltage applied (V)	Wavelength (nm)	Intensity mW/cm^2		
Au/P-NiO/n-ZnO/ITO	- 0.5	365	3	0.14	This work
Cu/NiO/ZnO/ITO/glass	- 5	365	varied from 10 to 80 Lux.	0.2-1.2	(Alzahrani et al., 2018)
Ti-Au/ZnO/NiO/FTO	1	365	-	0.28	(Debnath et al., 2015)
Ag/ZnO nanorod /NiO film/FTO	zero-bias	355	0.4	0.44 mA/W	(Shen et al., 2015)
Ni/NiO/ZnO/ITO	-5	365	-	2.1×10^{-2}	(Hwang et al., 2018)

6.3.4 Simulation of the effects of ZnO and NiO defects on the performance of NiO/ ZnO photodetectors

Disordered materials contain a large number of defect states within the bandgap of the material. To accurately model devices made of polycrystalline or amorphous materials, use a continuous density of states. The recombination at the bulk is taken into consideration. Recombination through defect levels in semiconductors is usually described by the Shockley–Read–Hall theory. Figure 6.11 shows a schematic of band tails and localized energy levels in NiO and ZnO bandgaps. The parameters of the DOS used to simulate the ZnO and NiO bulk of the NiO/ZnO photodiode are presented in Table 6.6. Furthermore, the default values of capture cross-sections for a majority and minority carriers are 1×10^{-14} and $1 \times 10^{-16} \text{ cm}^2$ respectively.

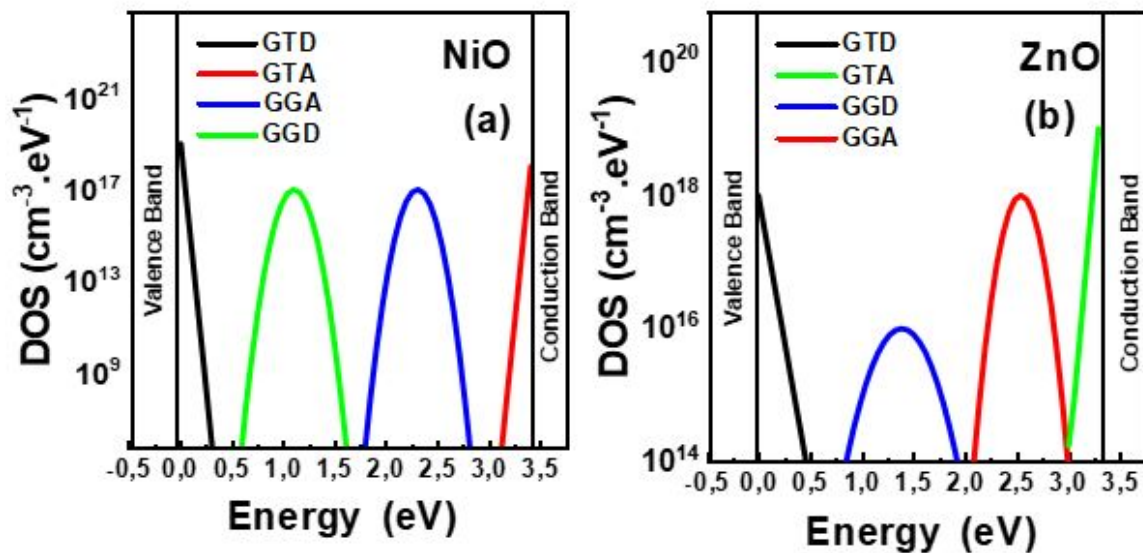


Figure 6.11: Acceptor and donor Tail States and Gaussian Distributions function energy for (a) NiO and (b) ZnO.

The density of states (DOS) is composed of two tail bands a donor-like valence band (GTD) and an acceptor-like conduction band (GTA) and two deep level bands one acceptor-like (GGA) and the other donor-like (GGD) which are modeled using a Gaussian distribution. Concerning the illumination conditions are the incident light power density of 3 mW/cm^{-2} at 365 nm wavelength.

Table 6.6: The parameters of the DOS used to simulate the NiO and ZnO bulk of the NiO/ZnO photodiode (Elseman et al., 2018; Chala et al., 2018).

Parameters	Unis	ZnO	NiO
Peak energy (EGA)/ peak distribution	eV	1.5	1.1
Peak energy (EGD)	eV	0.75	1.1
Gaussian distribution/ decay energy (WGA)	eV	0.025	0.1
Gaussian distribution/ decay energy (WGD)	eV	0.05	0.1
Decay energy/stand for tail (WTA)	eV	0.1	0.01
Decay energy/stand for tail (WTD)	eV	0.1	0.01

6.3.4.1 Defects in NiO bulk

The first case was studying the effect of the tail states in NiO bulk on the photodiode performance by varying, acceptor/donor densities. The density deep states were kept at low value $NGA=NGD=1 \times 10^{10} cm^{-3}.eV^{-1}$. The values of the tail donor density (NTD) and tail acceptor density (NTA) were varied from 1×10^{16} to $1 \times 10^{21} cm^{-3}.eV^{-1}$. We have used the extracted generation rate and recombination rate from simulations to understand the behavior of the dark and light currents. The influence of different NiO tail densities on J-V characteristics (dark and light conditions) and responsivity are shown in Figure 6.12 (a) and (b) respectively.

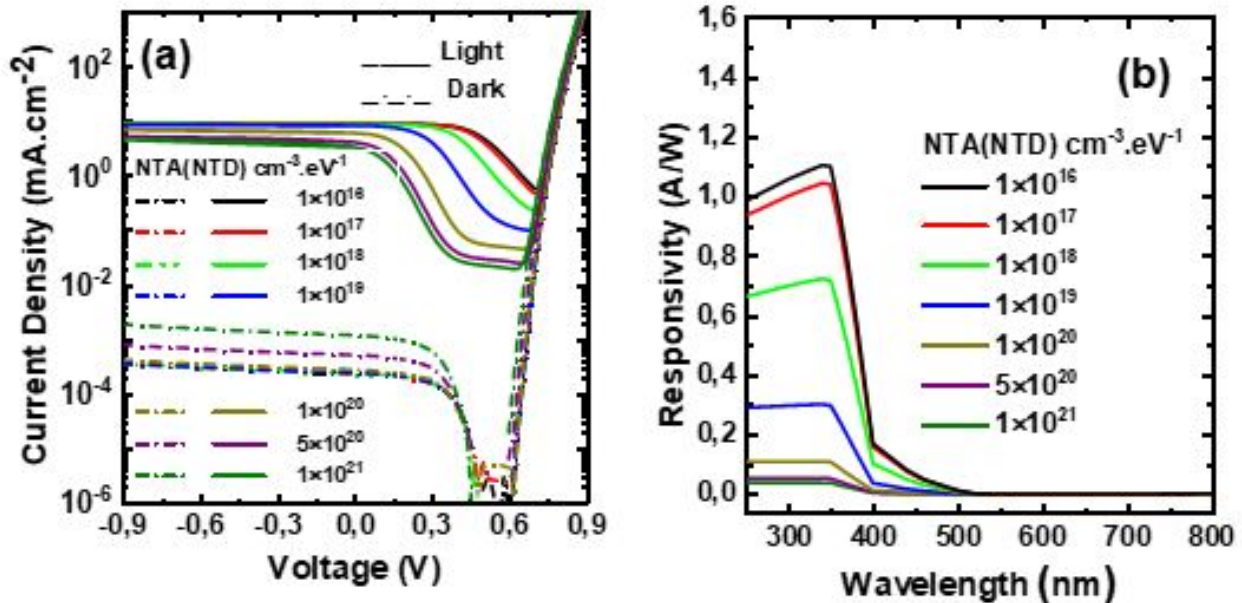


Figure 6.12: (a) Dark current and photocurrent and (b) Responsivity of the NiO/ZnO heterojunction under different tail densities in NiO bulk.

It can be seen that by increasing NiO tail densities, the dark current increases. This can be explained by carrier transport mechanisms. The recombination rate due to the presence of defects increased from 5.07×10^{12} to $1.4 \times 10^{17} \text{ cm}^{-3} \cdot \text{s}^{-1}$. The generation rate increases from 1.34×10^{18} to $8.1 \times 10^{18} \text{ cm}^{-3} \cdot \text{s}^{-1}$ from the tunneling mechanism which means increases the number of carriers that tunnels. The dark current, as results, increased strongly at a high tail density from 5×10^{-4} to $4 \times 10^{-3} \text{ mA} \cdot \text{cm}^{-2}$. Increasing the dark current confirms that the transport of carriers' tunneling and recombination limits current transport. Also, it limits the photodetection parameters under illumination. The responsivity reduced from 1.14 to 0.03 A/W which means that NiO tail states have an impact on the photodiode behavior where the defects act as recombination centers. The observation directly informs that reducing NiO tail states density can dramatically enhance the photodiode performance.

In the second step, the tail state density was kept at a low value $\text{NTA}=\text{NTD}=1 \times 10^{10} \text{ cm}^{-3} \cdot \text{eV}^{-1}$. The values of the gaussian donor density (NGD) and gaussian acceptor density (NGA) were varied from 1×10^{14} to $1 \times 10^{18} \text{ cm}^{-3} \cdot \text{eV}^{-1}$. The effect of different NiO gaussian densities on J-V characteristics and responsivity are shown in Figure 6.13 (a) and (b) respectively.

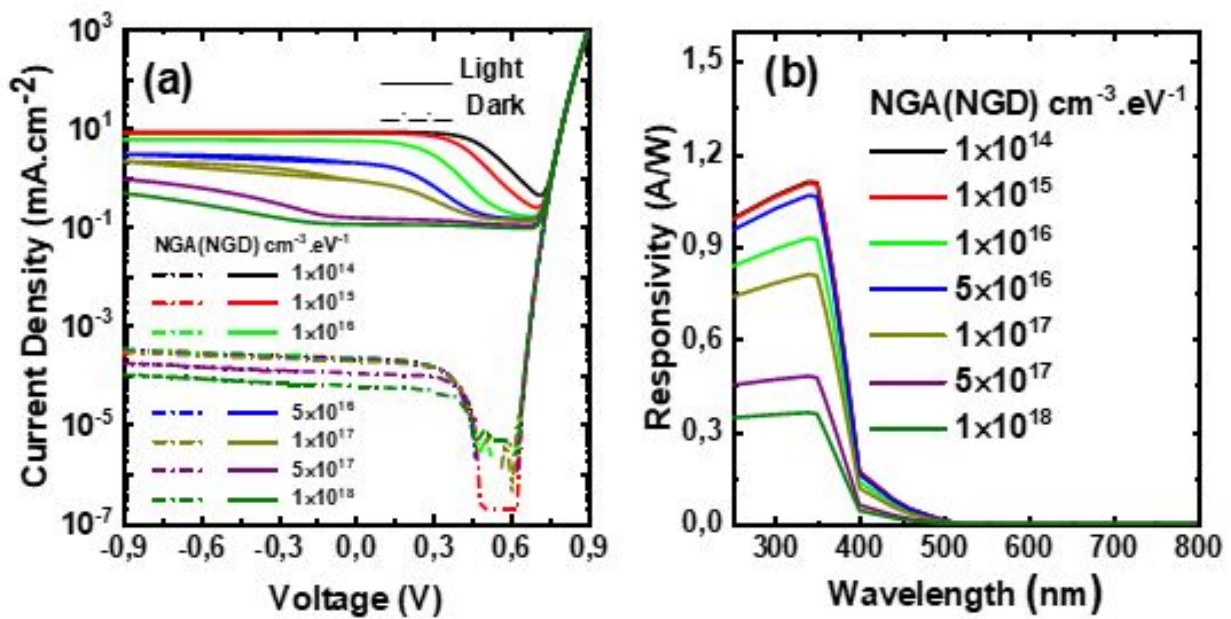


Figure 6.13: (a) Dark current and photocurrent and (b) Responsivity of the NiO/ZnO heterojunction under different Gaussian densities in NiO bulk.

It can be seen that the dark current decreased at high NiO Gaussian states to $1 \times 10^{-4} \text{ mA} \cdot \text{cm}^{-2}$. With increasing Gaussian states, the recombination rate increased to $7 \times 10^{13} \text{ cm}^{-3} \cdot \text{s}^{-1}$, noticing that tunneling rate decreased from 1.34×10^{18} to $2.56 \times 10^{17} \text{ cm}^{-3} \cdot \text{s}^{-1}$. Increasing NiO Gaussian states results in a small decrease of dark current from a high recombination rate which limit the photodetection parameters. The photocurrent was reduced to $0.5 \text{ mA} \cdot \text{cm}^{-2}$. The responsivity was reduced from

1.11 to 0.36 A/W. Those defects state act as recombination centers.

6.3.4.2 Defects in ZnO bulk

In order to understand the effect of ZnO tail defects densities on the NiO/ZnO device performance, Figure 6.14 illustrates the J-V characteristics and responsivity (a) and (b) respectively. Using the same previous steps, The values of NTD and NTA were varied from 1×10^{16} to $1 \times 10^{20} \text{ cm}^{-3} \cdot \text{eV}^{-1}$. The NGD and NGA were kept at a low value $1 \times 10^{10} \text{ cm}^{-3} \cdot \text{eV}^{-1}$.

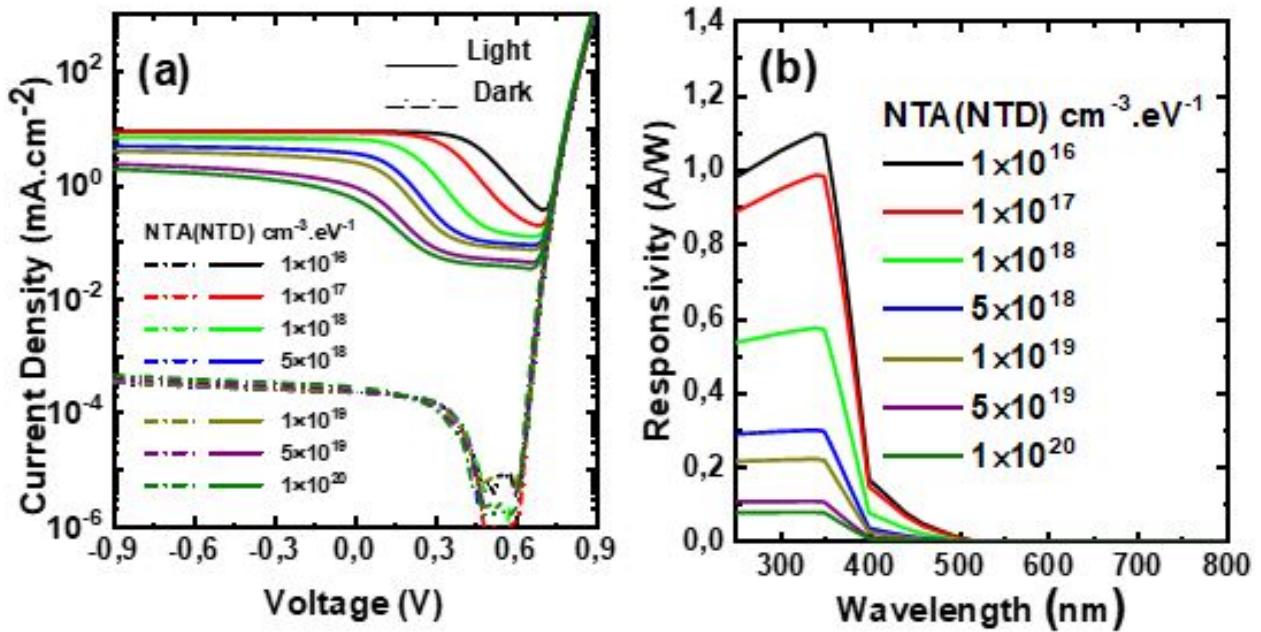


Figure 6.14: (a) J-V characteristics and (b) Responsivity of the NiO/ZnO photodiode under different ZnO tail defects.

As can be seen in Figure 6.14, the dark current increased very slightly at high ZnO tail defects. The carrier transport mechanisms are affected due to the presence and increasing of ZnO tail defects. Noticing, there are slight effects on the generation rate and tunneling which increased from 1.3×10^{18} to $1.9 \times 10^{18} \text{ cm}^{-3} \cdot \text{s}^{-1}$. Also, increasing these tail states results in a high recombination rate from 1.7×10^{12} to $1.04 \times 10^{16} \text{ cm}^{-3} \cdot \text{s}^{-1}$ which limit the photodetection mechanisms. The responsivity reduced from 1.1 to 0.07 A/W and the photocurrent also decreased.

The influence of ZnO gaussian density on J-V characteristics and responsivity is shown in Figure 6.15 (a) and (b) under conditions $\text{NTD} = \text{NTA} = 1 \times 10^{10} \text{ cm}^{-3} \cdot \text{eV}^{-1}$.

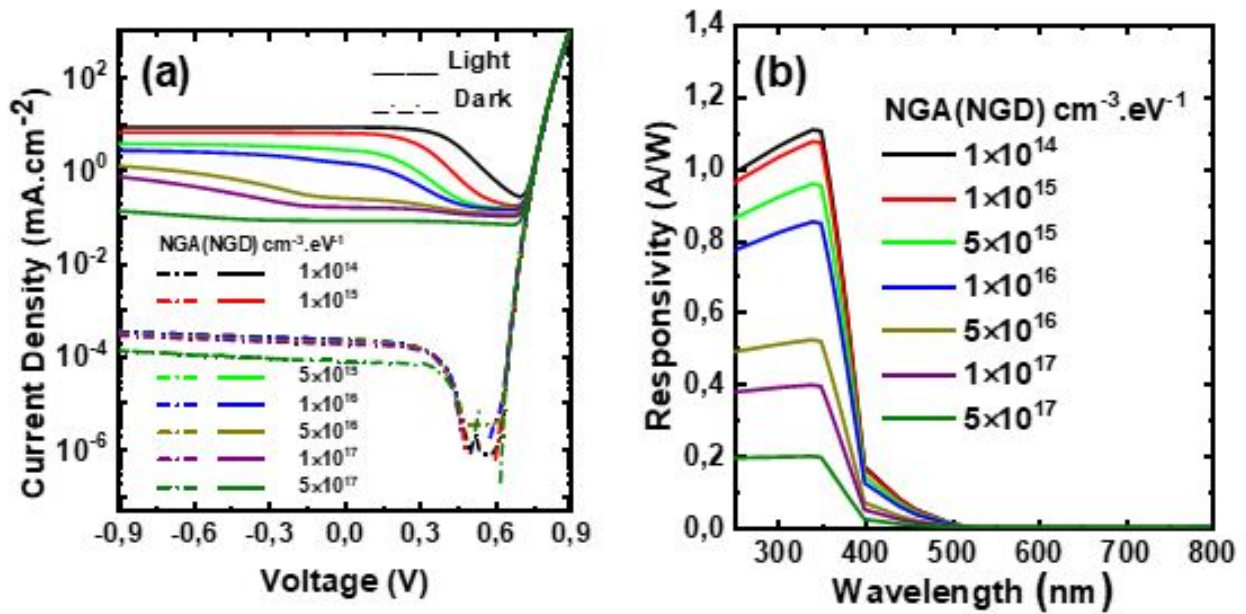


Figure 6.15: (a) J-V characteristics and (b) Responsivity of the NiO/ZnO photodiode under different ZnO gaussian defects.

As a result of increasing NGA (NGD), the recombination rate increased from 9×10^{11} to $3.3 \times 10^{14} \text{ cm}^{-3} \cdot \text{s}^{-1}$. The dark current decreased which confirms that the recombination limits the dark current. Also, in turn, decreases tunneling rate to $3.5 \times 10^{17} \text{ cm}^{-3} \cdot \text{s}^{-1}$. Under illumination, We observed an influence on the photodetection performance.

6.4 NiO/ZnO heterojunction fabrication and characterization

Based on the results of Chapter 6. We choose to fabricate NiO/ZnO heterojunction by NiO and ZnO thin films under 15 ml quantity of solution conditions deposited by chemical spray pyrolysis technique. Under the same deposition conditions presented in Table 6.1. We fabricated a NiO/ZnO heterojunction following the steps indicated in Figure 6.16.

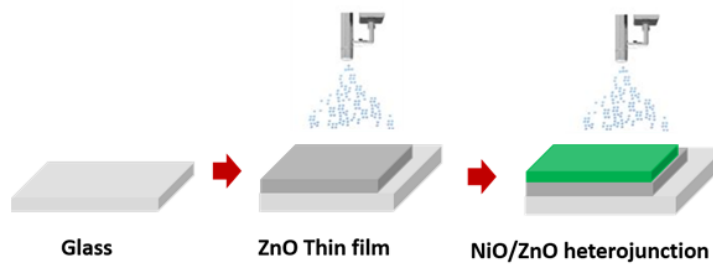


Figure 6.16: Fabrication process of NiO/ZnO heterojunction deposited by spray pyrolysis.

6.4.1 Structural properties

Figure 6.17 represents the X-ray diffraction pattern of NiO/ZnO heterostructure. The deposition of NiO/ZnO was performed using the condition that showed the best structural properties (15 ml as a quantity of solution). Figure 6.18 shows the Raman spectra of NiO /ZnO heterostructure.

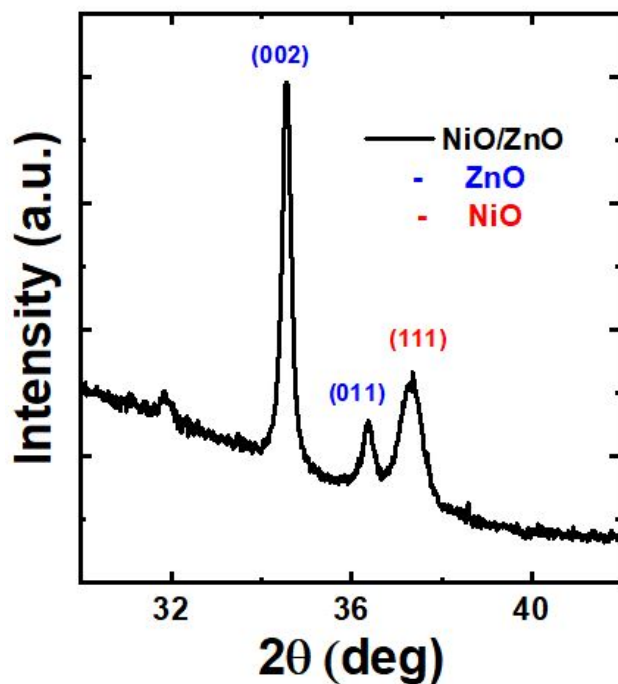


Figure 6.17: XRD patterns of NiO/ZnO heterostructure.

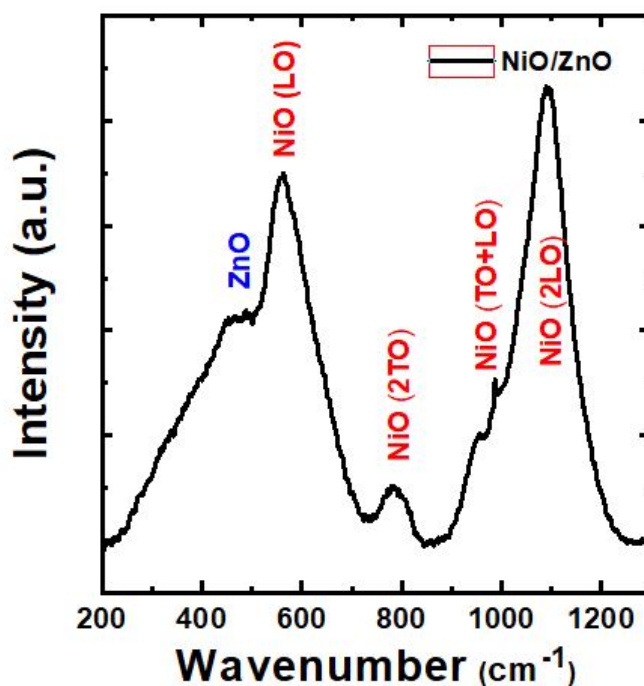


Figure 6.18: Raman spectra of NiO/ZnO heterostructure.

The pattern clearly shows the presence of peaks belonging to ZnO and NiO. The coexistence of those peaks confirms the heterostructure formation without any impurities. Raman spectroscopy has been performed in order to demonstrate the hetero-structural composite formation. As can be seen, the Raman active modes of both materials are deconvoluted into broad bands representing different vibrations modes. the NiO/ZnO junction formation is proved by the shift (50 cm^{-1}) from the standard Raman modes of NiO and ZnO. The band centered at 450 cm^{-1} correspondings to first-order TO (E1TO) is representative of ZnO wurtzite structure of good crystalline quality. The vibrational modes present at $550, 782, 952$ and 1090 cm^{-1} describes the Longitudinal Optical (LO), two Transverse Optical (2TO), TO+LO and two Longitudinal Optical (2LO) vibration modes, respectively, correspond to Raman modes of NiO. The slight shift has been reported in several studies for NiO/ZnO composite and it is attributed to the diminution in the coupling of Ni–O oscillation after the formation of heterojunction (Qiao et al., 2013; Sandana et al., 2015; Luo et al., 2014). As well as the confirmation of NiO/ZnO heterostructure, Raman results confirm the purity of both NiO and ZnO thin films without secondary phases as indicated in XRD results.

6.4.2 Optical properties

Figure 6.19 shows the optical transmission of three prepared structures, NiO thin film, ZnO film and NiO/ZnO heterojunction.

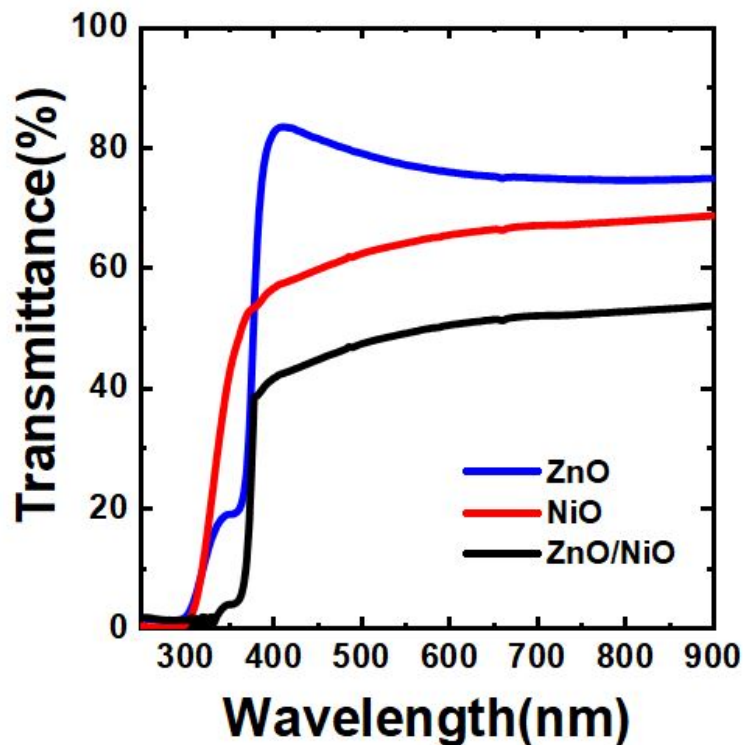


Figure 6.19: Transmittance spectra of ZnO, NiO thin films and ZnO/NiO heterojunction.

The average transmittance rate of ZnO thin films is about 78% in the 450- to 900 nm range, and the average transparency of the NiO thin film is about 60% in the 450- to 900 nm range which indicates that the films could be used as transparent windows or UV photodetectors. The transmission through heterojunction decreased to less than 50% in the visible region probably due mainly to the presence of interface traps. However, the transmittance fell rapidly in the UV region near the absorption edge, which indicated that the NiO/ZnO heterojunction could be a good candidate for the fabrication of UV detectors.

6.4.3 Morphology properties

The prepared NiO and ZnO thin films were further analyzed using FESEM to get information about surface morphology. Figure 6.20 (a, b, c, d, e, f and g) shows the morphology of ZnO and NiO as well as cross-section taken for the ZnO/NiO heterostructure sample.

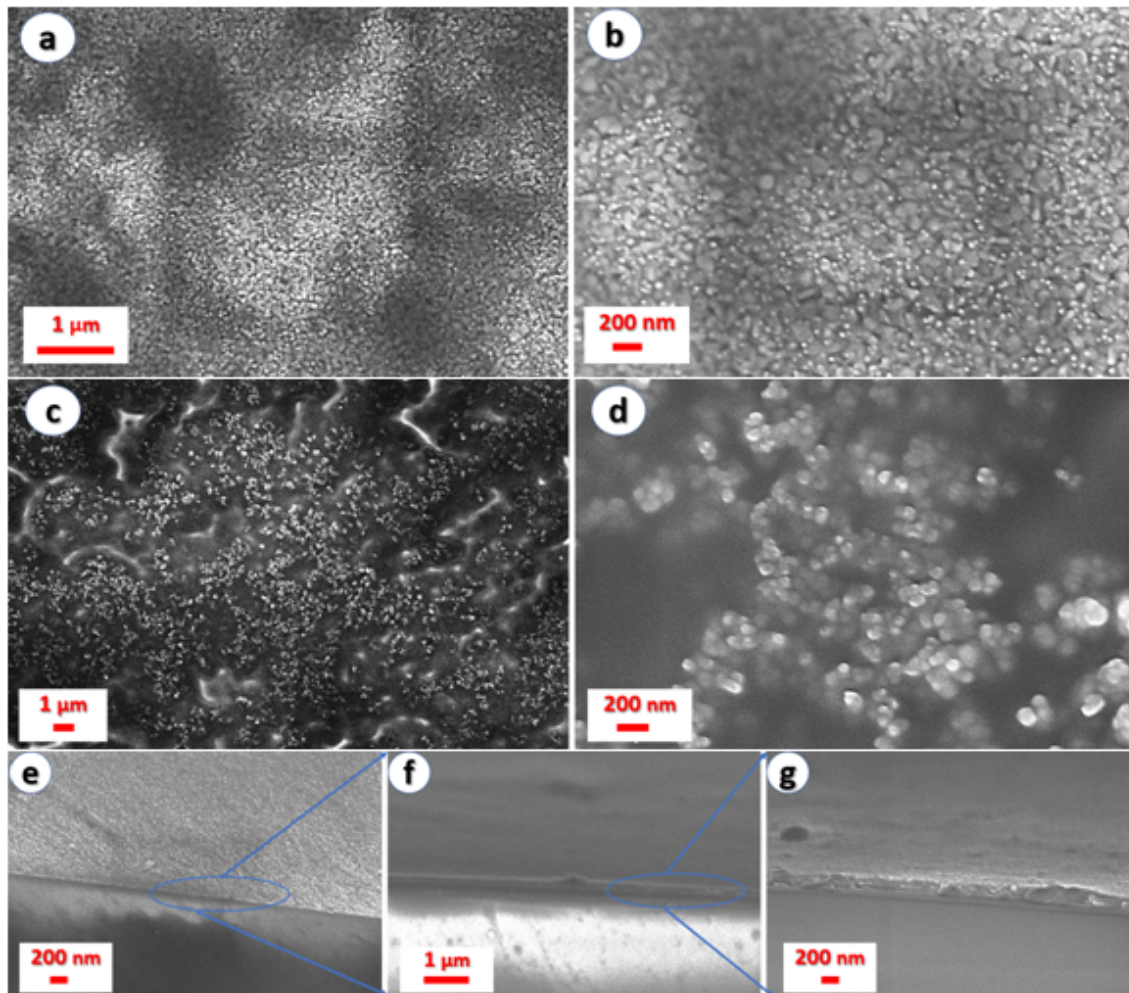


Figure 6.20: SEM images of (a) and (b) ZnO thin films with different magnifications. (c) and (d) NiO with different magnifications and (e), (f) and (g) Cross-sectional visualizing the NiO/ZnO heterostructure with different magnifications.

As shown in Figure 6.20 (a) and (b), the obtained ZnO film is dense, has a good homogeneity with a smooth surface and comprises small rod-shaped and nanograins with an average size of around 150 nm length and 80 nm diameter, respectively. A similar result has been obtained by Muchuweni et al. (2017) who produced a film consisting of rod-shaped and spherical nanoparticles for optoelectronic applications. Figure 6.20 (c) and (d) shows the NiO morphology. In contrary to ZnO, NiO thin films shows dense and small spherical nanoparticles have been produced. Taking into account the same quantity of solution for the deposition both films, the less density observed for NiO nanoparticles could be explained by the slow growth rate of NiO in comparison with ZnO (Tsai et al., 2011). Moreover, as can be seen in Figure 6.20 (e) and (g) the surface of heterostructure NiO/ZnO is smooth and completely covered without any pinholes.

The heterojunction analysis results are similar to the literature. There are a large number of published studies (Sultan et al., 2017; Karsthof et al., 2020; Grundmann et al., 2014) describing the link between the presence of interface traps in NiO/ZnO heterojunctions and the low quality of these devices. Some of the authors were mainly concerned with the questions regarding the effects of interface quality on the performance of the NiO/ZnO device. However, these studies were not able to determine how the interface parameters affect the device characteristics which indicates the failure of the experiments. Before addressing the experimental study of our fabricated NiO/ZnO device, what is required is to use simulations to obtain precise information about the NiO/ZnO heterojunction photodiode behavior, dark current transport mechanism and how the interface traps controlling the quality of the device. The set of material parameters which are required for simulation of the value of bandgap, thickness, n and k optical parameters are extracted from our experimental study.

6.5 Study of NiO/ZnO heterojunction interface

It becomes essential to gain in-depth knowledge about charge transport mechanisms involved in the p-type NiO/n-type ZnO heterojunction devices. We performed a numerical simulation based on SILVACO ATLAS to investigate the effects of interface traps on the performance of NiO/ZnO heterojunction photodiode. NiO/ZnO photodiode is modeled and is carefully examined by analysis of the band diagram, J-V characteristics and responsivity. The structure of the simulated device is shown in Figure 6.21.

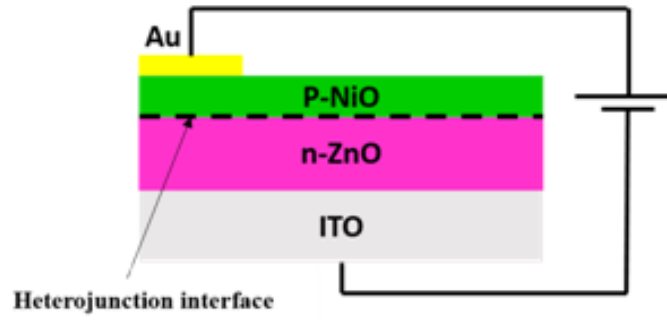


Figure 6.21: NiO/ZnO heterojunction photodiode structure.

6.5.1 NiO/ZnO heterojunction behavior

The band alignment of heterojunction under thermal equilibrium is ultimately determined by band offsets (Zheng et al., 2020). Figure 6.22 shows the band diagram of a typical type-II heterojunction before contact.

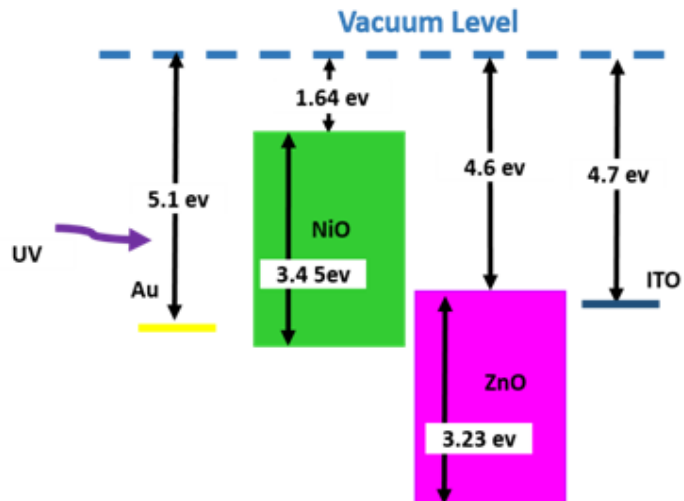


Figure 6.22: Energy band diagram of the NiO/ZnO heterojunction before contact.

The top Gold electrode has a high work function of 5.1 eV, and its Fermi level pins on NiO at approximately 4.7 eV, which approximately matches the Fermi level (E_F) of p-NiO, and the work function of the 4.7 eV bottom ITO is low enough that it approximately matches the E_F of n-ZnO (Hassan et al., 2020). When a heterojunction is formed, The conduction band offset (ΔE_c) between NiO and ZnO is found to be 2.96 eV. On other hand, the valence band offset (ΔE_v) between NiO and ZnO was determined to be 2.74 eV. The magnitudes of the respective offsets have been determined by various researchers and are summarized in Table 6.7.

Table 6.7: Comparative values for the valence and conduction band offsets for NiO/ZnO heterojunction.

(ΔE_c)	(ΔE_v)	Ref
2.96	2.74	This work
2.54	2.04	(Karsthof et al., 2020)
2.74	2.71	(Wu et al., 2015)
2.80	2.41	(Tyagi et al., 2015)
2.93	2.6	(Deng et al., 2009)
2.82	2.65	(Sultan et al., 2017)

After an external voltage of 1.1 V is applied (Figure 6.23), thin barrier spikes at the interface and a reduction of the offsets of the band levels some nanometers away from the junction are observed due to band bending. A similar shape of the band diagram of a biased NiO/ZnO junction has been published in references (Jung et al., 2013; Felbier, 2015).

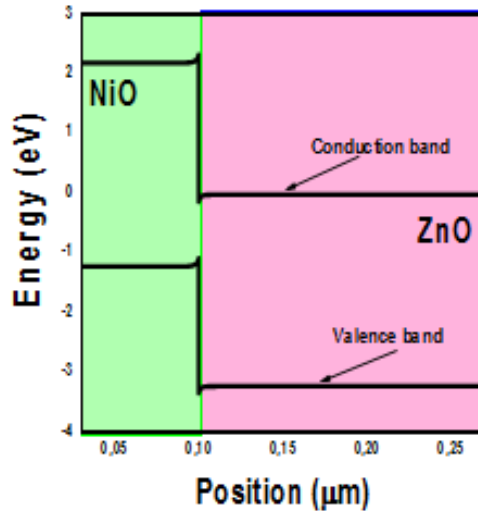


Figure 6.23: band levels at the external bias of 1.1V.

Another important feature of the band structure in the NiO/ZnO heterojunction is the built-in potential, which was determined by the interface position of the Fermi levels $E_{F_{NiO}}$ and $E_{F_{ZnO}}$. The band bending resulted from the built-in potential on both sides of the interface to the extent that the Fermi levels in two semiconductors eventually line up to be constant and flat. In heterojunction, the barrier height has become much larger potential is much larger too. Figure 6.24 shows if an external bias is applied in the forward direction, the built-in potential is decreased. In contrast, with increasing the reverse voltage, the potential increases.

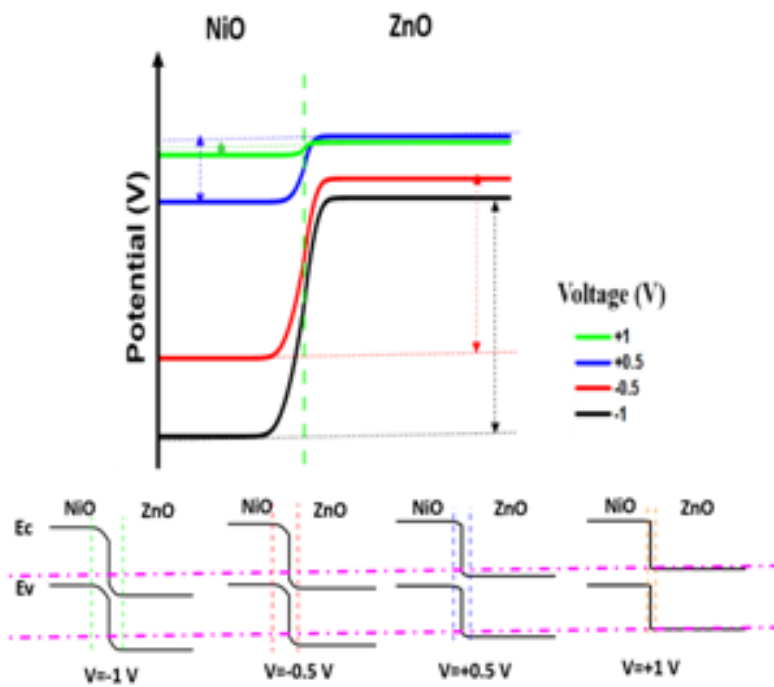


Figure 6.24: Simulated potential of the NiO/ZnO heterojunction under different applied voltages.

Figure 6.25 shows an electric field distribution was simulated when a reverse bias was applied. The reverse-biased condition leads to more electrons and holes generation and more effective separation due to the expanded depletion width and enhanced electric field.

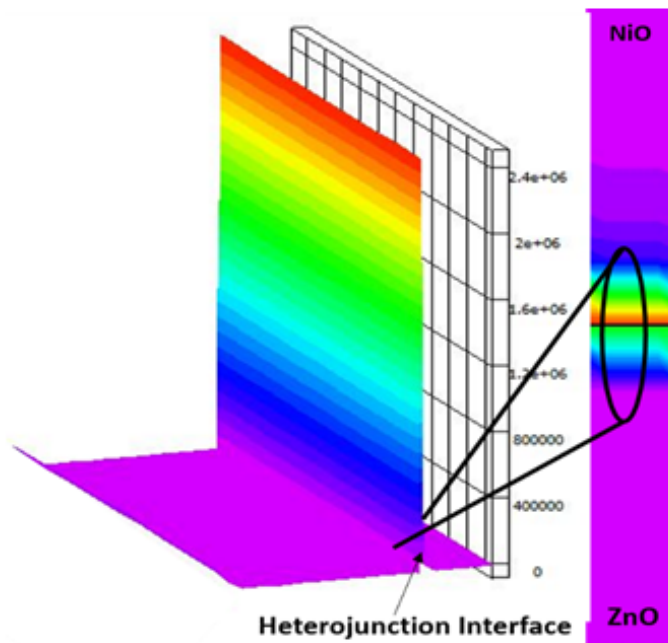


Figure 6.25: Simulated electric field of the NiO/ZnO heterojunction.

6.5.2 Modeling J-V characteristics of the photodiode

Figure 6.26 shows the comparison of simulated J-V characteristics with and without using tunneling model.

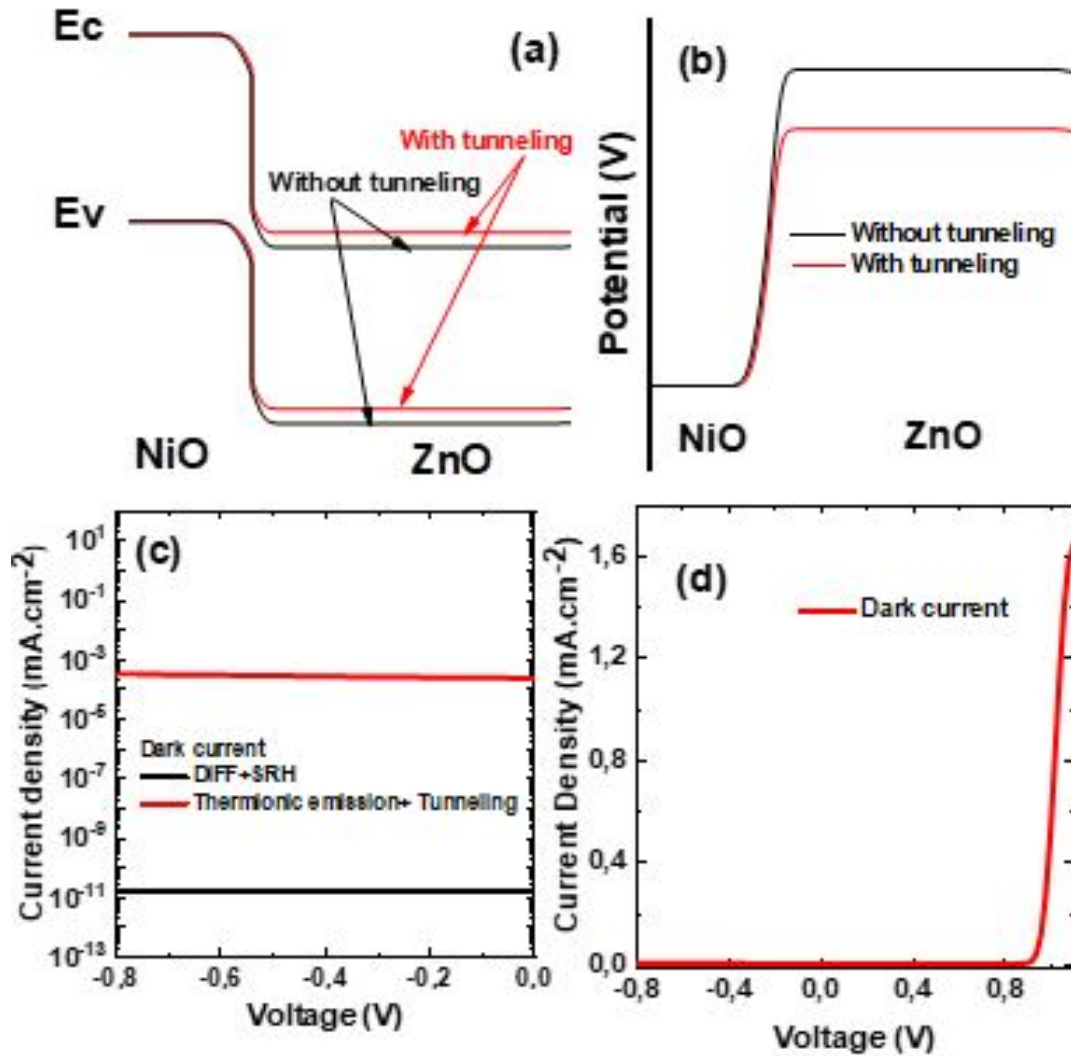


Figure 6.26: (a) Energy band diagram (b) Potential of the NiO/ZnO heterojunction without and with using tunneling model (c) Dark current considering the contributions of SRH, thermionic emission and band to band tunneling under reverse bias. (d) J-V characteristics for NiO/ZnO heterojunction photodiode.

It is seen that the model provides a good description of dark current. The simulation results reveal that the major dark current flowing in reverse bias range is due to SRH generation and tunneling component. The diffusion current is lower than 10^{-11} mA.cm⁻². Table 6.8 confirms that the carrier transport mechanism should not be described by diffusion only, and other transport mechanisms need to be incorporated as thermionic emission theory and tunneling mechanisms in semiconductor/semiconductor interface.

While the drift-diffusion charge carrier transport is the dominant one in bulk semiconductors, homojunction and smoothly graded heterojunctions, two fundamental mechanisms exist that describe charge carrier transport across steep barriers at abrupt heterojunction interfaces: thermionic emission and tunneling (Felbier, 2015; Deveaud, 2007). A charge carrier moving over a potential barrier by thermionic emission. Tunneling mechanisms allow charge carriers to leak through a finite zone with a potential higher than the carrier's total energy. It becomes dominant over thermionic emission at very high barriers. If a sufficiently high electric field exists within a device local band bending may be sufficient to allow electrons to the tunnel, by internal field emission, from the valence band into the conduction band. An additional electron is therefore generated in the conduction band and a hole in the valence band. This generation mechanism is implemented into the right-hand side of the continuity equations (Manual, 2008).

Table 6.8: The light and dark current constitution under reverse bias 0.8V.

Structure	Dark current ($mA.cm^{-2}$)	Light Current ($mA.cm^{-2}$)	Ref
Au/NiO/ZnO/ITO	6.3×10^{-4} (Thermionic+Tunneling)	2.6	This work
Au/NiO/ZnO/ITO	1.9×10^{-11} (Diff+SRH)	-	This work
Au/NiO/ZnO	10^{-4}	10^1	(Karsthof et al., 2020)
NiO/ZnO pn-diode	10^{-7}	5×10^{-1}	(Grundmann et al., 2014)
Au/NiO/ZnO/Au	10^{-5}	2	(Karsthof et al., 2016)
NiO/ZnO nanorods	10^{-2}	10^{-1}	(Echresh et al., 2015)

6.5.2.1 Photocurrent modeling

In such a device, under the light exposure and reverse bias conditions, the exposed neutral region and the depletion region, both absorb the light, consequently, the hole-electron pairs are photogenerated (Figure 6.27 (a)). The device is simulated using monochromatic UV excitation with intensity of $3 mW.cm^{-2}$. Each material is modeled using appropriate material parameters and nk file, using real part of refractive index and the photogenerated carriers due to the absorption light (Figure 6.27(b)) at each grid point is calculated from the imaginary component of refractive index (Vallisree et al., 2018).

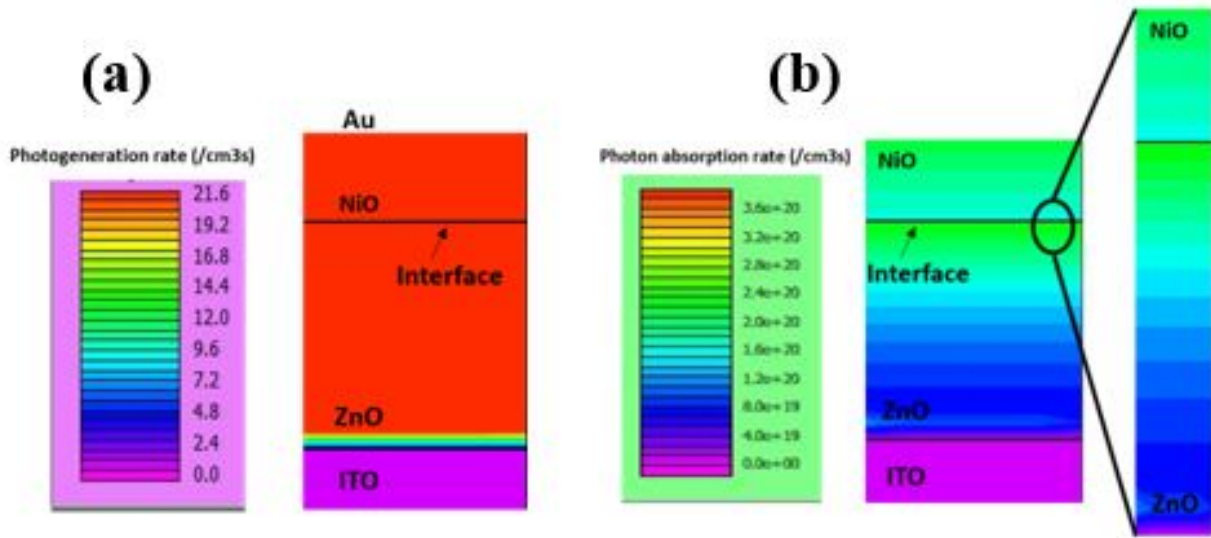


Figure 6.27: (a) Photogeneration rate (b) Photon absorption rate at the NiO/ZnO heterojunction photodiode.

Under UV illumination, electron-hole pairs are generated in the depletion region of the device. At the interface of NiO and ZnO films, the built-in electric field across the depletion region separates the photogenerated electron-hole pairs and drives them out of the depletion region. drifted electrons then diffuse through the ZnO layer to be collected at the ITO cathode. Similarly, the photogenerated holes reach the Au anode through the NiO layer (Vallisree et al., 2018; Hassan et al., 2020).

6.5.3 Modeling of the interface traps parameters effect

We investigated the effects of the interface trap parameters as interface trap density (D_{it}), electron capture cross-section (σ_n), Acceptor interface trap density and donor interface trap density on the performance of NiO/ZnO heterojunction photodiode, We considered the effects of the above-mentioned parameters individually, while maintaining other parameters constant.

6.5.3.1 Trap density

We varied the interface trap density from 8×10^{10} to $8 \times 10^{12} \text{ cm}^{-2}$ in steps of one order to see its influence on band diagram, potential, trap recombination rate, dark current, photocurrent and responsivity. The capture cross-section for electrons $\sigma_n = 7.24 \times 10^{-16} \text{ cm}^2$ and the capture cross-section for holes $\sigma_p = 7.24 \times 10^{-15} \text{ cm}^2$. The band diagram and potential of the simulated photodiode versus D_{it} are shown in Figure 6.28.

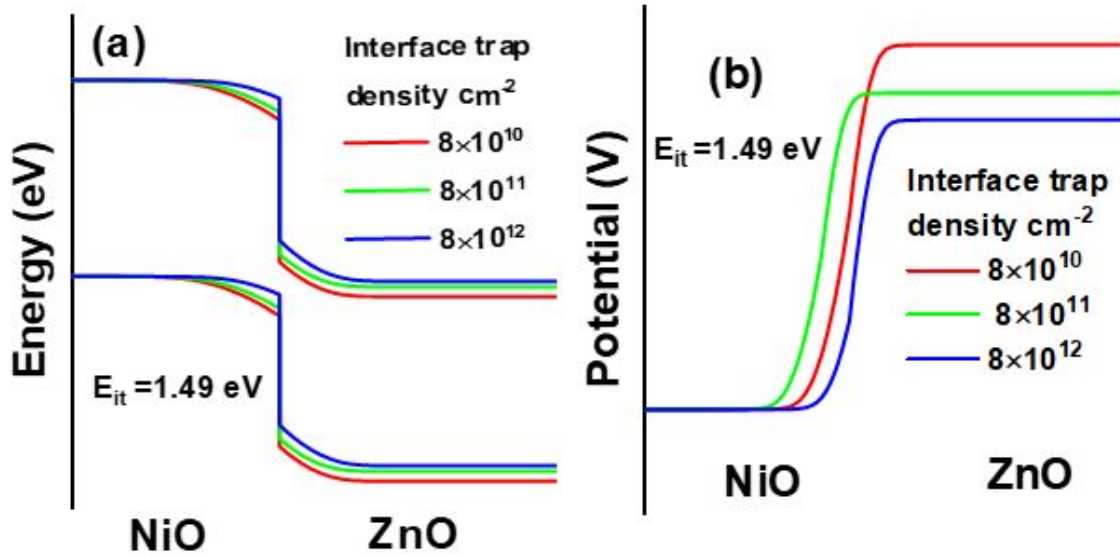


Figure 6.28: (a) Simulated energy band diagram and (b) Simulated potential of the NiO/ZnO heterojunction under different interface trap density (-0.5V).

The band diagram behavior has changed by increasing the interface traps, and Also these traps affect build-in potential in the heterojunction. From Table 6.9, we can understand the behavior of band bending with increasing the interface strap states. Recombination rate, generation rate and tunneling rate increased by increasing interface traps density which means the interface recombination and the transport to the interface limiting process in type II heterojunction.

Table 6.9: Extracted parameters were used to describe carrier transport mechanisms at the NiO/ZnO interface under different interface trap densities (-0.5V).

Interface trap density (cm^{-2})	Recombination rate ($\text{cm}^{-3} \cdot \text{s}^{-1}$)	Generation rate ($\text{cm}^{-3} \cdot \text{s}^{-1}$)	Tunneling rate ($\text{cm}^{-3} \cdot \text{s}^{-1}$)
8×10^{10}	4.5×10^{16}	1.4×10^{18}	1.2×10^{16}
8×10^{11}	7.1×10^{16}	2×10^{18}	1.6×10^{17}
8×10^{12}	1.4×10^{19}	4×10^{20}	2.4×10^{20}

To further identify the influence of interface trap on the J-V characteristics and responsivity, Figure 6.29 presented (a) The trap recombination rate, (b) dark current, (c) photocurrent and (d) responsivity respectively.

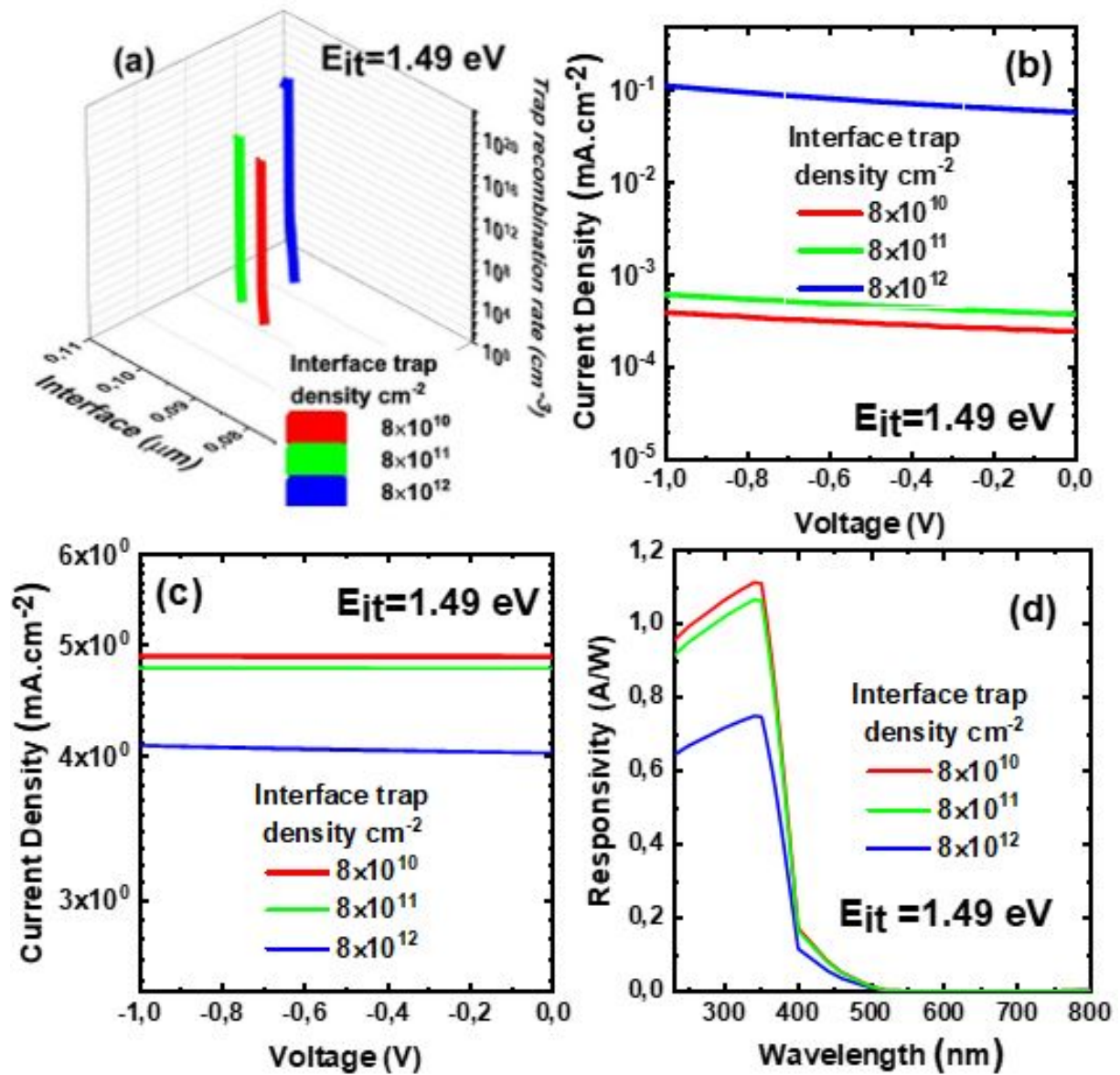


Figure 6.29: (a) Trap recombination rate (-0.5V), (b) Dark current, (c) Photocurrent and (d) Responsivity of the NiO/ZnO heterojunction under different interface trap density.

As a result of increasing interface trap density, the trap recombination rate increased. The dark current increased also from 10^{-4} to 10^{-1} mA.cm⁻² which confirms that the transport of free carriers to interface and interface recombination limits the dark current. It is found that there is a significant band bending in the NiO/ZnO heterojunction that decreases the barrier near the NiO to ZnO region. This, in turn, increases the number of carriers that tunnels, and increasing the dark current. Under illumination, We observed low influence on the photodetection performance photocurrent and responsivity.

6.5.3.2 Electron cross-section

The influence of electron capture cross sections of interface traps on the J-V characteristics (dark and light conditions) and responsivity are shown in Figure 6.30 (a) (b) and (c). The values of σ_n was varied from $\sigma_n = 2.84 \times 10^{-12}$ to $2.84 \times 10^{-15} \text{ cm}^2$ by step of a decade. The interface trap states density was kept at a value of $5 \times 10^{12} \text{ cm}^{-2}$.

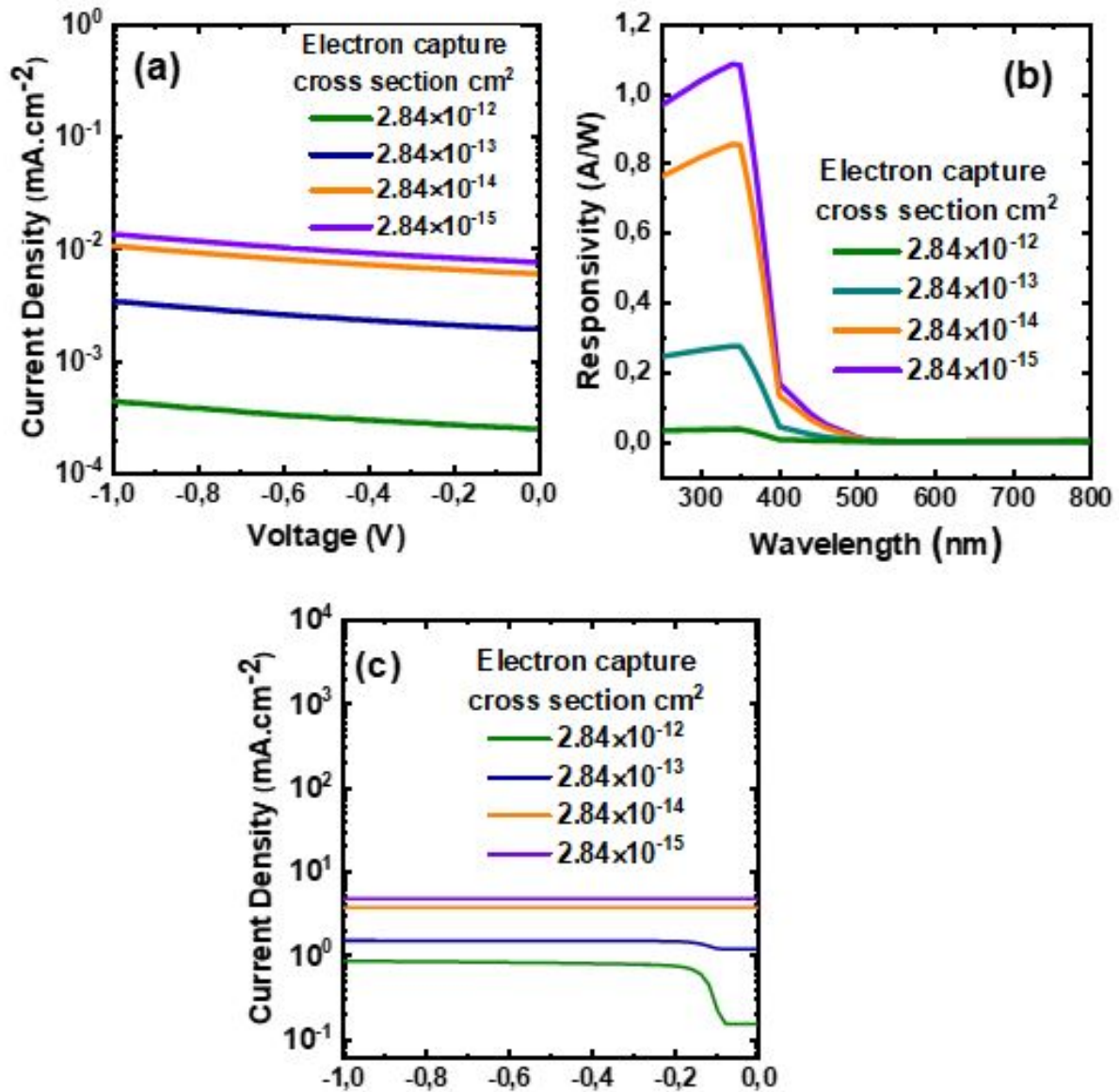


Figure 6.30: (a) Dark current, (b) Responsivity, (c) Photocurrent of the NiO/ZnO heterojunction under different electron capture cross-sections of interface traps.

It can be seen that the J-V characteristic of the NiO/ZnO heterojunction photodiode depends strongly on the recombination rate associated with increasing electron capture cross-section as presented in Table 6.10. The trap state acts as a recombination center. Under illumination, the photocurrent and responsivity strongly decrease when electron cross-section increases.

Table 6.10: Extracted parameters were used to describe carrier transport mechanisms at the NiO/ZnO interface under different electron capture cross-sections of interface traps (-0.5V).

Electron capture cross section (cm^2)	Trap Recombination rate ($cm^{-3}.s^{-1}$)	Generation /recombination ($cm^{-3}.s^{-1}$)	Tunneling rate ($cm^{-3}.s^{-1}$)
2.84×10^{-12}	8.7×10^{19}	$4.66 \times 10^{19} / 4.2 \times 10^{19}$	4.5×10^{19}
2.84×10^{-13}	6.9×10^{19}	$4.5 \times 10^{19} / 2.4 \times 10^{19}$	4.5×10^{19}
2.84×10^{-14}	2.1×10^{19}	$4.5 \times 10^{19} / -$	4.5×10^{19}
2.84×10^{-15}	2.7×10^{19}	$4.5 \times 10^{19} / -$	4.5×10^{19}

6.5.3.3 Acceptor trap density

We examined the impact of the acceptor interface trap density on the performance of the device, described by the electrical (dark and light J-V), and optical (responsivity) characteristics. This study sheds light on the influence of the acceptor density on the photodiode performance (trap energy level=0.6 eV, it is equal to the energy distance between conductance band and trap level, the capture cross-section for electrons $\sigma_n = 2.84 \times 10^{-13} cm^2$). The donor trap states density was kept at a low value of $5 \times 10^8 cm^{-2}$. The values of the acceptor trap density were varied from 5×10^{10} to $5 \times 10^{12} cm^{-2}$. (a) The band diagram, (b) J-V dark, (c) J-V light characteristics and (d) Responsivity of the designed NiO/ZnO heterojunction photodiode under different acceptor trap density states are shown in Figure 6.31.

Table 6.11: Extracted parameters were used to describe carrier transport mechanisms at the NiO/ZnO interface under different acceptor interface trap densities (-0.5V).

Acceptor trap density (cm^{-2})	Trap Recombination rate ($cm^{-3}.s^{-1}$)	Generation /recombination ($cm^{-3}.s^{-1}$)	Tunneling rate ($cm^{-3}.s^{-1}$)
5×10^{10}	8.27×10^{16}	$1.37 \times 10^{18} / -$	3.02×10^{18}
5×10^{11}	1.8×10^{18}	$1.8 \times 10^{18} / -$	1.8×10^{18}
1×10^{12}	2×10^{18}	$2.6 \times 10^{18} / -$	2.5×10^{18}
5×10^{12}	1.6×10^{20}	$4.5 \times 10^{19} / 2.34 \times 10^{19}$	4.5×10^{19}

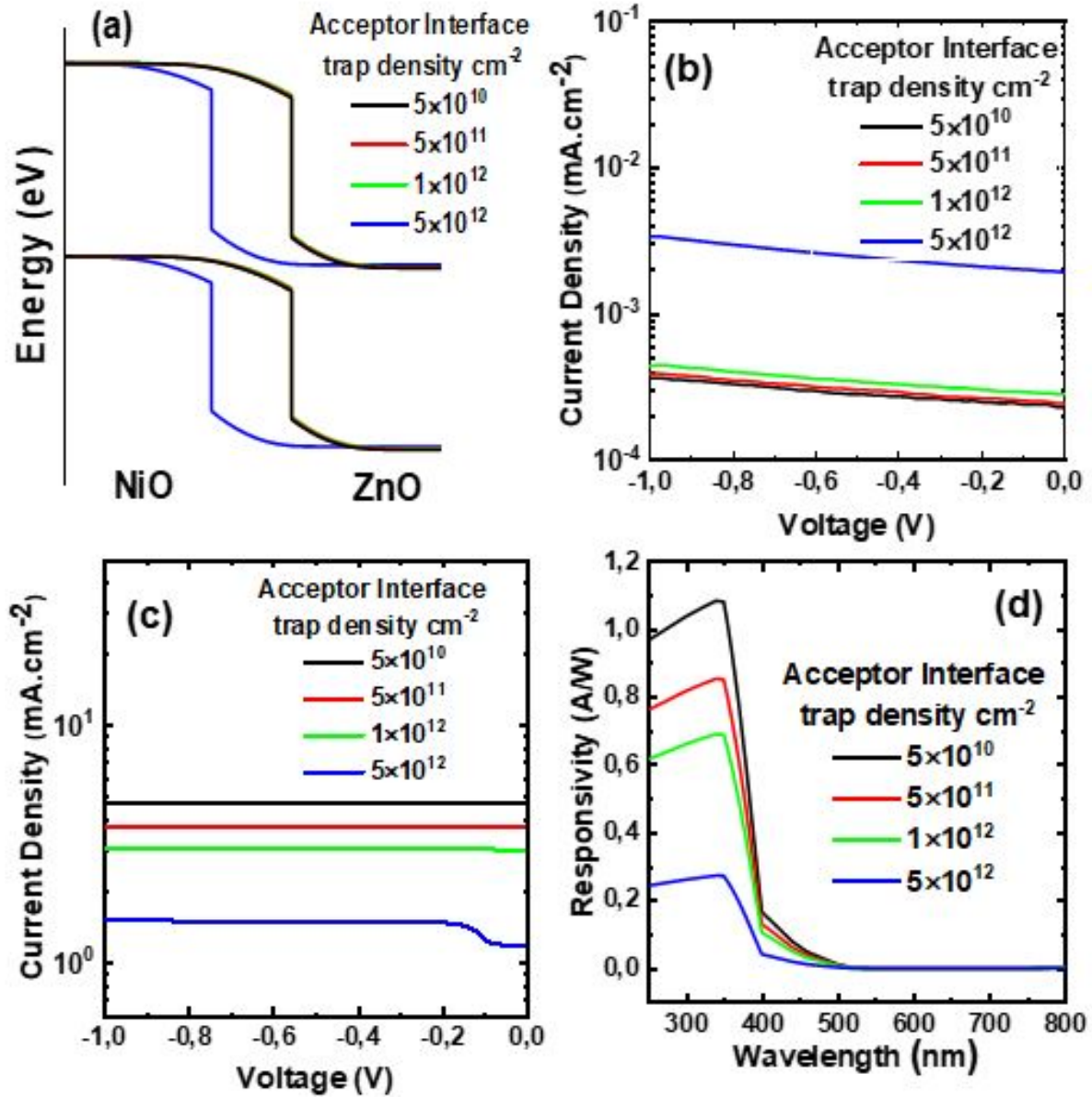


Figure 6.31: (a) Band diagram (-0.5V), (b) J-V dark, (c) J-V light characteristics and (d) Responsivity of the designed NiO/ZnO photodiode under different acceptor interface trap density.

As can be seen in Figure 6.31, due to the presence and increasing acceptor trap density, the band bending reduced at NiO/ZnO junction. The influence of different acceptor trap densities on the trap state recombination rate, generation and recombination rate and tunneling rate of the photodiode are summarized in Table 6.11. We can see that acceptor interface traps affect carrier transport mechanisms by increasing the recombination rate due to the presence of traps and high generation rate from tunneling mechanism, which results in the dark current increased strongly at high acceptor trap density. Also, increasing acceptor traps results in a high recombination rate at the interface which limit the photodetection parameters. The responsivity reduced from 1.1 A/W to 0.3 A/W which means that acceptor traps have an impact on the photodiode behavior where the traps act as recombination cen-

ters. The observation directly informs that reducing interface trap density can dramatically suppress the photodiode performance.

6.5.3.4 Donor trap density

In this step, the acceptor trap state density was kept at a low value of $5 \times 10^8 \text{ cm}^{-2}$. The donor density was varied from 5×10^{10} to $5 \times 10^{12} \text{ cm}^{-2}$. (Trap energy Level=0.5 eV, it is equal to the energy distance between trap level and valence band for donor trap, the capture cross-section for electrons $\sigma_n = 1 \times 10^{-13} \text{ cm}^2$). The band bending, J-V characteristics of the NiO/ZnO photodiode under dark and UV light conditions, and responsivity for different donor trap densities are shown in Figure 6.32.

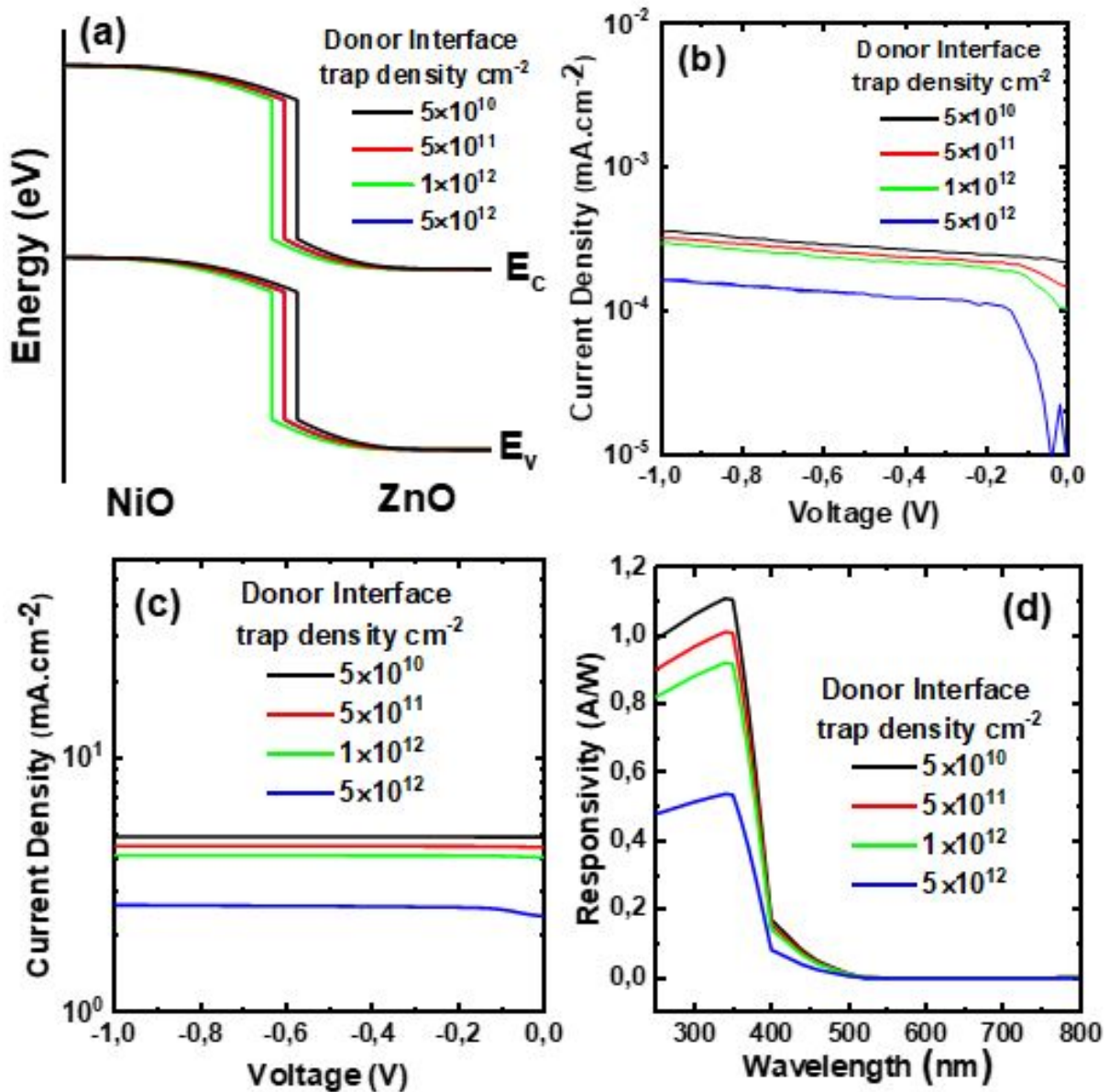


Figure 6.32: (a) Band diagram (-0.5V), (b) Dark current, (c) Photocurrent and (d) Responsivity of the NiO/ZnO heterojunction under different donor interface trap density.

Table 6.12: Extracted parameters were used to describe carrier transport mechanisms at the NiO/ZnO interface under different donor interface trap densities (-0.5V).

Donor trap density (cm^{-2})	Trap Recombination rate ($cm^{-3}.s^{-1}$)	Generation /recombination ($cm^{-3}.s^{-1}$)	Tunneling rate ($cm^{-3}.s^{-1}$)
5×10^{10}	2.8×10^{16}	$1.33 \times 10^{18} / -$	1.33×10^{18}
5×10^{11}	2.62×10^{17}	$1.33 \times 10^{18} / -$	1.33×10^{18}
1×10^{12}	4.7×10^{17}	$1.33 \times 10^{18} / -$	1.33×10^{18}
5×10^{12}	1.3×10^{17}	$1.29 \times 10^{18} / 3 \times 10^{16}$	1.27×10^{18}

According to Figure 6.32 (a), the band bending is repositioned by increasing the trap density. The dark current decreased at high donor trap $2.3 \times 10^{-4} mA.cm^{-2}$. The influence of different donor trap densities on the trap state recombination rate, generation and recombination rate and tunneling rate of the photodiode are summarized in Table6.12. We can see that with increasing donor interface traps, the recombination rate increased due to the presence of donor traps noticing that tunneling mechanism did not affect. Increasing donor traps results in a small decrease of dark current from a high recombination rate at the interface witch limit the photodetection parameters too. The responsivity was reduced from 1.11 to 0.5 A/W. The interface donor traps have a low impact on the photodiode behavior comparing with acceptor traps. Those traps act as recombination centers.

Interface traps at the NiO/ZnO interface are a major determinant of the performance of the hetero-junction for optoelectronic applications. The traps at the NiO/ZnO interface degraded the device performance by enhancing generation and recombination. As a result, it is important to develop techniques to reduce the interface trap density (Alnuaimi et al., 2013).

6.6 Semi-transparent NiO/ZnO heterojunction growth and characterization

Silicon substrates were used as support for growing NiO, ZnO thin films and NiO/ZnO heterojunction for material characterization. Substrates were ultrasonically cleaned in acetone solvent for 20 min and then dried in synthetic air to remove any dust or contamination. The condition of thin film deposition are summarized in Table 6.13.

Table 6.13: The experimental conditions for deposition of NiO/ZnO thin films.

Conditions	NiO	ZnO
Target NiO	(purity, 99.99%)	ZnO (purity, 99.99%)
Substrate temperature	300 °C	300 °C
Power	150 W	75 W
Pressure	$4,9 \times 10^{-3}$ Torr	$4,9 \times 10^{-3}$ Torr
Deposition time	30 min	15 min

6.6.1 Structural properties

Figure 6.33 shows spectra of NiO, ZnO and NiO/ZnO heterojunction. The diffraction patterns of films and heterojunction were recorded by varying diffraction angle (2θ) in the range of 33° to 50° . Microstructural parameters such as crystallite size (D), dislocation density (δ) and microstrain (ϵ) were calculated using Equations (6.1) (6.2) and (6.3) and tabulated in Table 6.14

Table 6.14: Crystallite size, dislocation density and microstrain of NiO and ZnO thin films extracted from XRD analysis.

Material	(hkl)	2theta (degree)	Crystalline size (nm)	Dislocation density ($10^{15}/m^2$)	Micro strain (10^{-3})
NiO	(111)	36.1	14.54	4.727	2.489
ZnO	(002)	34.05	17.70	3.189	2.044

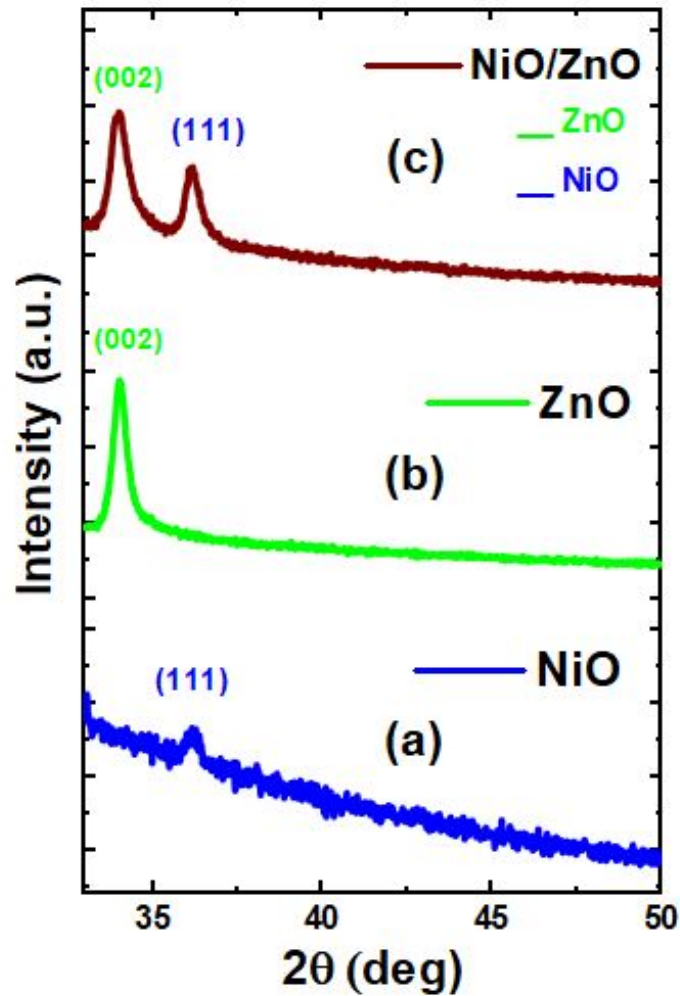


Figure 6.33: XRD spectra of (a) NiO (b) ZnO thin film and (c) NiO/ZnO heterojunction.

XRD spectrum of NiO is shown in Figure 6.33 (a). One peak appears at the angle of 36.1° and is assigned to (111) plane of the NiO cubic phase (JCPD:00-047-1049) (Alzahrani et al., 2018; Huang et al., 2013b). Figure 6.33 (b) shows XRD pattern of ZnO film, the main peak that corresponds to (002) plane at the diffraction angle 34.05° much with JSPD: 98-008-1576. The identified peak reveals that ZnO has a hexagonal structure. XRD pattern of NiO/ZnO heterojunction is shown in Figure 6.33 (c). The pattern exhibited the (002) diffraction peak of ZnO crystallization at angle 34.05° . The diffraction peak revealed that (2θ) value of 36.1° corresponded to the (111) plane of the NiO thin film which was similar to the results in Figure 6.33(a) and (b). However, The intensity of (111) X-ray reflection increases which means the crystalline structure quality of the NiO thin film will be controlled by ZnO thin film.

6.6.2 Morphology properties

Figure 6.34 shows the morphology of NiO thin film (Figure 6.34 a and b), ZnO thin film (Figure 6.34 c and d) and NiO/ZnO heterojunction (Figure 6.34 e - g).

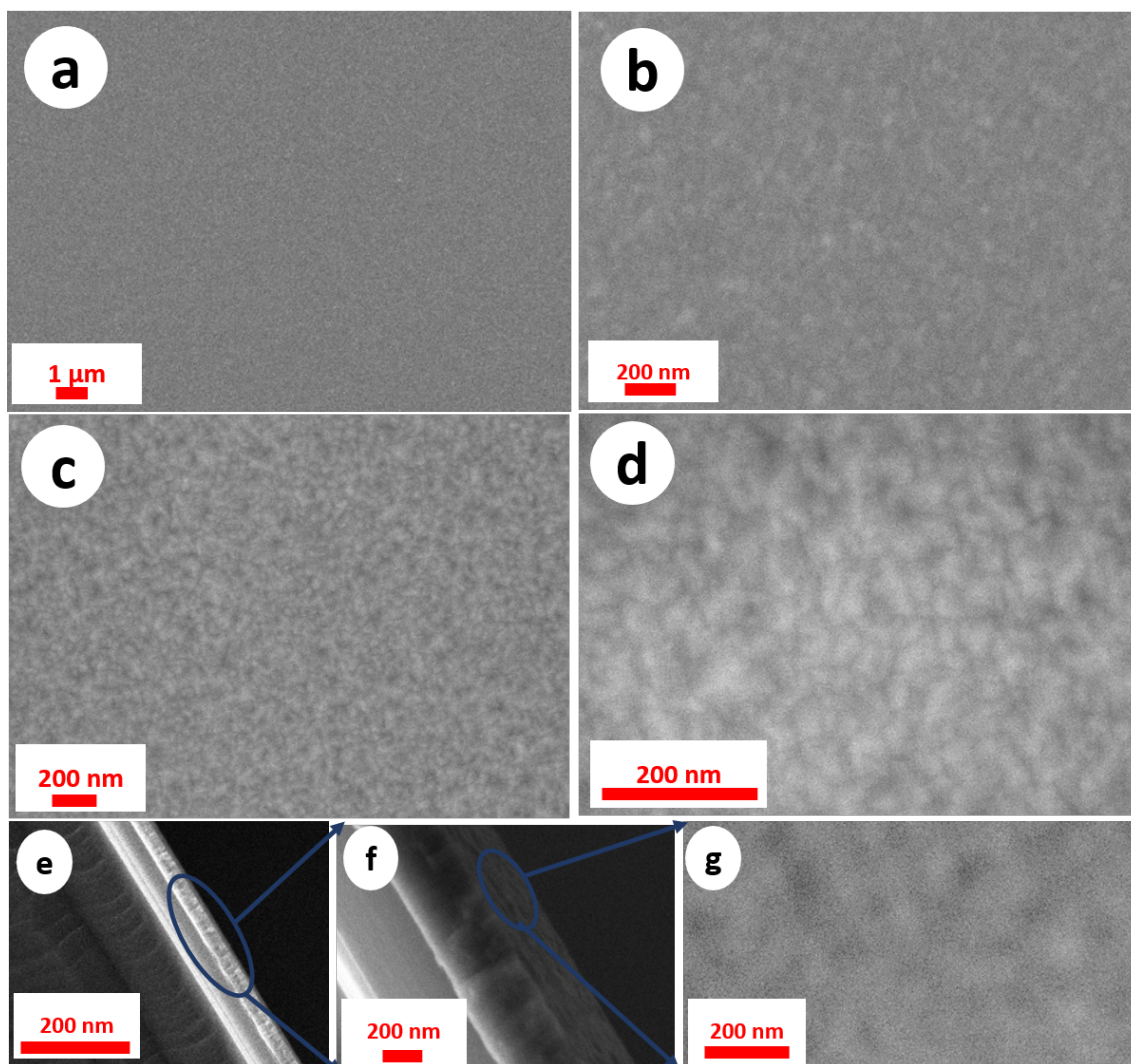


Figure 6.34: SEM images of (a) and (b) NiO thin films with different magnifications. (c) and (d) ZnO with different magnifications and (e), (f) (g) Cross-sectional visualizing the NiO/ZnO heterostructure with different magnifications.

The ZnO film is densely packed and almost pinholes free which is a characteristic of the sputtering technique. The obtained NiO film is relatively smooth with fine grain structures. The cross-sectional SEM images show that a planar and dense interface exists in NiO/ZnO heterojunction (Figure 6.34 e-g). The thickness of NiO and ZnO thin films was estimated to be 130 nm and 240 nm respectively.

6.6.3 Optical properties

The optical properties are important factors to define semiconductor materials. Figure 6.35 shows (a) the transmittance and (b) absorbance spectra of ZnO, NiO thin films, and NiO/ZnO heterojunction prepared with by sputtering were recorded in the wavelength range (300 nm -800 nm).

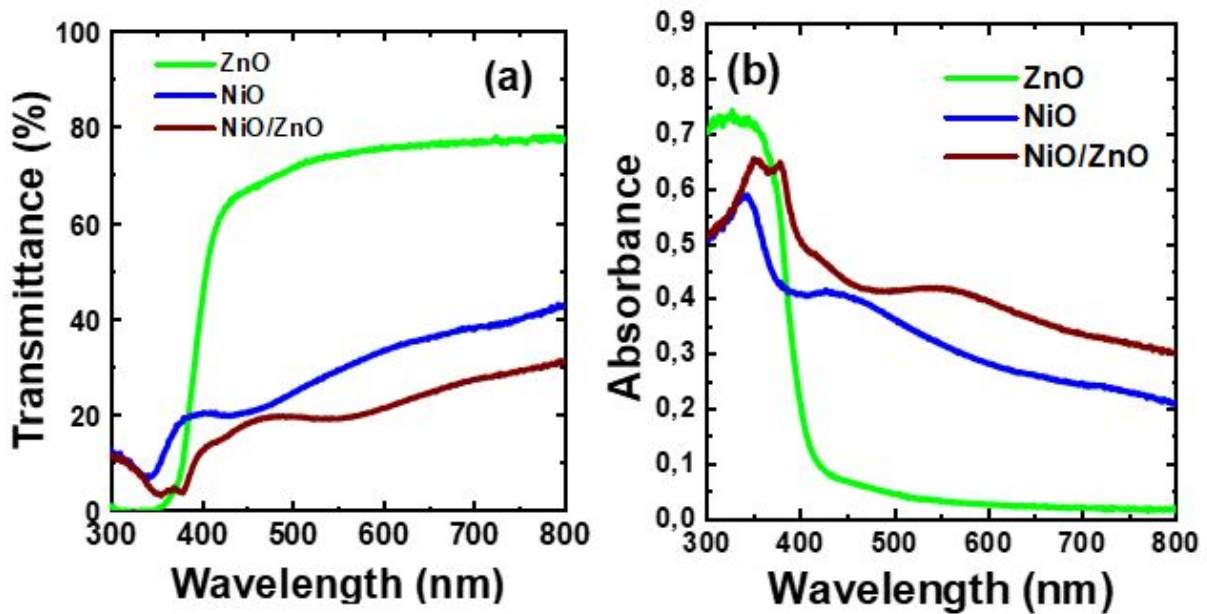


Figure 6.35: (a) Optical transmittances and (b) absorbance spectra of NiO, ZnO thin films, and NiO/ZnO heterojunction.

It is seen that ZnO thin film has a good absorbance in the ultraviolet range and high transmittance in the visible range when it is rich in 80%. Besides, NiO shows small transparency and high absorbance in the visible region. The average transmission value less than 45%. The transmission through complete heterojunction is near to 30% in the visible region.

The data from the transmission spectrum are used to calculate the absorption coefficient (α) by Equation 6.4. The optical band gap (E_g) of the films was extracted from the plots of $(\alpha h\nu)^2$ versus photon energy ($h\nu$) using Tauc's relation (Equation 6.5). The real part of the refractive index (n) and imaginary part (k) are calculated by Equation 6.6 and 6.7. Figure 6.36 shows (a) absorption coefficient (b) The optical band gap (c) refractive index and (d) extinction coefficient of NiO and ZnO films.

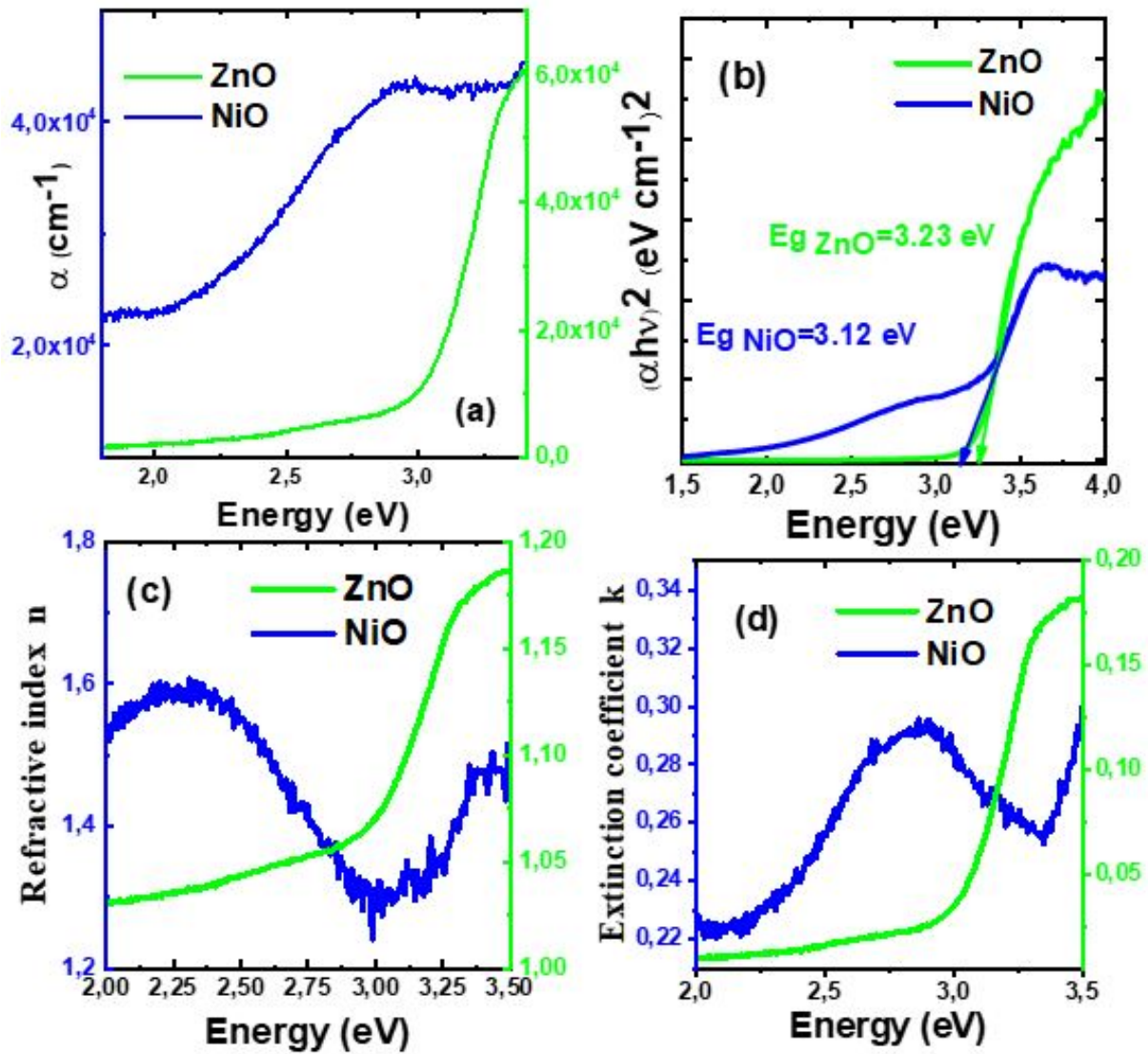


Figure 6.36: (a) Absorption coefficient (α) (b) $(\alpha h\nu)^2$ and energy $h\nu$ (c) The extracted refractive index and (d) the extinction coefficient of NiO and ZnO films deposited by RF sputtering.

For ZnO, it was observed that the coefficient of absorption (α) increases gradually with the decrease in photon energy ($h\nu$) and the value of the absorption coefficient is $6 \times 10^4 \text{ cm}^{-1}$, The bandgap of ZnO thin film is 3.23 eV. The refractive index was observed to decrease exponentially from about 1.18 to 1.07 between 3.5 and 3 eV, after which it became nearly constant. NiO thin film shows a good absorption coefficient demonstrating the direct electronic transitions (Mezher et al., 2020). The deposited NiO film has a small bandgap of 3.12 eV. This value is in agreement with those obtained in the literature (Hwang et al., 2017; Reddy et al., 2012a) for the NiO phase under vacuum conditions.

6.6.4 Influence of oxygen flow on optical properties of NiO thin film

We investigated the transmittance of NiO thin films deposited by the RF sputtering technique at 25% oxygen flow. The transmittance of NiO thin films as a function of the wavelength plotted at different

oxygen flow is reported in Figure 6.37. NiO films had a similar thickness of about 130 nm which was achieved by controlling the deposition time, to avoid thickness effect on the transmittance.

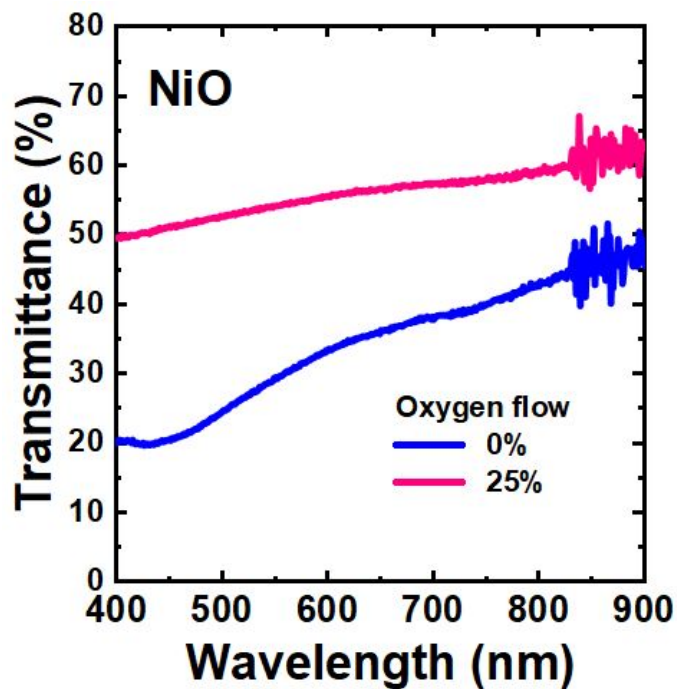


Figure 6.37: Transmittance spectra of NiO thin films at different oxygen flow.

The 0%- O_2 -deposited NiO film shows a small transmittance ($< 45\%$). In contrast, the transmittance exceeds 60% in the visible range (wavelength > 460 nm) for 25%- O_2 -deposited NiO film. The improvement in the transmittance at 25% oxygen flow may be due to the improvement of crystallinity in the films (Reddy et al., 2012b; Hwang et al., 2017). The transmittance and bandgap of the NiO thin films have been compared with previously reported findings. (see Table 6.15).

Table 6.15: Comparative studies of the experimental results of NiO with previous findings.

Target	Sputtering gas	Temperature (°C)	Thickness (nm)	Transmittance (%)	Bandgap (eV)	Ref
NiO	Ar/O ₂ (0 -25%)	300	130	45-60	3.1-3.6	This work
Ni	N ₂ /O ₂ P _{O₂} (0 to 100%)	room temperature	250-300	0.2-70-51.2	1.8-3.72-3.69	(Wang et al., 2017)
NiO	(Ar+O ₂) P _{O₂} (0 to 100%)	200	Fixed 90	50-60-40	3.08-3.18-3.12	(Hwang et al., 2017)
NiO	(Ar+O ₂) (10 to50%)	350	300	60-80-50	3.58-3.95	(Cheemadan et al., 2018)

6.7 Discussion

We studied the effect of source solution quantity on the properties of NiO and ZnO thin films and consequently NiO/ZnO photodiode performance. The results indicate that the thickness of thin films increases by increasing the quantity of solution for both NiO and ZnO films. This explains the improvement of structural properties at high quantity of solution. According to Alzahrani et al. (2018), the increase of the thickness reduces structural defects. Concerning the optical properties, the NiO transparency decreases because of the increasing of the thickness. The slight increasing of the reflectance of NiO indicates that it is better to place NiO in front of any light-absorbing device. The decrease of the bandgap of NiO might be due to an increase in thickness which may be related to the structural modification of the films. According to Godse et al. (2011), the decrease in the bandgap of NiO could be due to an increase in crystallinity and reduction of defects. It is consistent with our results of the improvement of the characteristics of the NiO structure by an increase in the quantity of solution. It is worth noting that although the same quantity of solution has been used for deposition of ZnO and NiO, the thickness of NiO is less than ZnO which seems to be due to the low growth rate due to the NiO large bandgap. Larger bandgap materials require high energy to be formed (Akyuzlu et al., 2017). Concerning ZnO thin films, the decrease of transparency ZnO is due to the increase in thickness (Yadav et al., 2009). It has been found that with increased quantities of solution for ZnO thin films, the optical bandgap increases marginally. In agreement with (Alzahrani et al., 2018), the small increase observed in the optical bandgap may originate from the films disorder that decreases with the thickness. Our Results for optical bandgap are in good agreement with those reported by Sharma et al. (2015). The obtained NiO and ZnO thin films are suitable for transparent device applications such as NiO/ZnO photodetectors in the present case. The different extracted parameters of NiO and ZnO (thickness, bandgap, refractive index and extinction coefficients) with quantity of solution variation are used for numerical simulation using ATLAS software to simulate the photodiode and clarify the effects of these parameters on the NiO/ZnO heterojunction photodiode performance. The designed NiO/ZnO heterojunction photodiode shows a good responsivity by increasing thickness of the ZnO and NiO layers. The thickness is the probable reason for increment in the I-V characteristics and responsivity of the heterojunction photodetector (Sharma et al., 2017). The simulation findings clearly demonstrate that the importance of choosing the thickness and optical parameters to improve the quality of the device. The photodetector mechanism depends on the quality of the material parameters. This can explain the reason for low performance in the case of 5 ml. In our study of the NiO and ZnO structural properties experimentally, it has been proven that when the quantity of solution is reduced, the material has defects. Which made us study, through simula-

tions, how defects affect the quality of the device. Considering the effects of the different constituents of the DOS, acceptor/ donor tail and Gaussian states in NiO and ZnO thin films. Defects begin to make a noticeable contribution to controlling photocurrent as well as the dark current. The former is due to the defect density that provides recombination which increases the losses under illumination (Fallahpour et al., 2017). By studying the defects in NiO and ZnO materials, we found that defects have a strong contribution to the electrical transport of the device. NiO tail states increasing causes an increase of tunneling current. In the contrast, there are slight effects on tunneling at high ZnO tail defects. The deep defects density in ZnO or even NiO affects the photodetection characteristics that the responsivity and photocurrent decrease with the increasing of Gaussian states. The electrical and optical characteristics of NiO/ZnO photodiode are dependent on the material structural properties. We found that by reducing the defects, the recombination rate reduced beside low tunneling current which means low dark current and high photodetection.

As reported in Wager (2017), band tail states are localised electronic states existing just below the conduction band or right above the valence band. They arise as a consequence disorder. Thermal, structural, impurity and or compositional disorder can all lead to formation of band tail states. In short, tail states are formed by disorder in structure (Labad et al., 2019). The electrical transport in NiO is dominated by hole carriers, generated by nickel vacancies with shallow defect levels (Sun et al., 2016; Zhang et al., 2008). According to Sun et al. (2016), According to Alzahrani et al. (2018), Increasing the film thickness reduces the defects. Therefore, a reduction in ZnO thickness may result in formation of large density of defect states and reduced recombination through higher crystallinity (Benhamida et al., 2017) which enhancing the photodetection.

We assumed that the model provides a good description of dark current by using Shockley-Read-Hall model while the bulk defects present. NiO tail states increasing causes an increase of tunneling current. The high tail and Gaussian states of thin films are the dominant cause of the low performance of the device. Therefore, the transport models and the heterojunction behavior will be discussed in detail.

The second study reports the growth of NiO, ZnO thin films and NiO/ZnO heterojunction on glass substrates at a temperature of 350°C prepared by spray pyrolysis method. Based on chapter 6 results, we fabricated NiO/ZnO junction with a 15 ml quantity of solution conditions.

Structural characterization suggested that the presence of both NiO and ZnO peaks indicates the formation of NiO and ZnO phases with orientation. The structure of the ZnO thin films is hexagonal of the wurtzite type and the NiO films crystallize in the cubic structure. The micro-Raman study confirms the XRD results showing the presence of the characteristics of the vibrational mode of both thin film structures.

The morphology of the obtained ZnO film is dense, has good homogeneity with a smooth surface. NiO thin film shows dense and small spherical nanoparticles. Taking into account the same spraying quantity for the deposition for both films, the less density observed for NiO nanoparticles which could be explained by the slow growth rate of NiO in comparison with ZnO. The surface of heterostructure NiO/ZnO is smooth and completely covered without any pinholes. Recently, Akyuzlu et al. (2017) reported that the NiO film processes smaller crystalline size and smoother surface when compared to that of ZnO. Therefore regardless of deposition method, surface smoothness seems to be an intrinsic property of NiO which might be from its low growth rate due to its large bandgap. Alzahrani et al. (2018) reported that larger bandgap material required higher energy formation.

The obtained NiO and ZnO films have an optical transmission of less than 60% and 78% respectively. The transmission through NiO/ZnO heterojunction is up to 50 %. In the visible region. It is worth mentioning that the optical transmission decrease in heterojunction as compared to the pure materials. According to Sultan et al. (2017), the contribution from the interfacial defects states may exist when the junction between NiO and ZnO forms. These interfacial defects can form due to a lattice mismatch between NiO and ZnO and can contribute to the absorbance of the device in the visible range.

We propose a numerical simulation which is an unavoidable tool to model the device behavior. The extracted parameters from the experimental study are used to design, characterize a NiO/ZnO photodiode structure, and to explain the influence of donor and acceptor interface traps on the performance of the device. The results of this study indicate also that NiO/ ZnO heterojunction exhibiting large band offsets in both valence and conduction bands. This will cause the so-called type-II band alignment where two materials share a gap of reduced size at the interface. The discontinuity of the band levels together with the barriers due to the build-in potential, define the fine structures of the heterojunction band diagram and determine the carrier transportation in the heterojunction devices. Zheng et al. (2020) has demonstrated that results the band alignment of heterojunction may cause some spikes and/or notches at the interface and acting as barriers or trapping sites for carrier transfer. Those unique features may possess a great influence on the performance of optoelectronic devices. According to authors, The performance of the type-II nano-heterojunctions largely relies on intrinsic properties of the semiconductor materials like chemical composition and crystal structure, interface characteristics such as band alignment and strain. Regarding the carrier transport mechanisms in the NiO/ZnO heterojunction photodiode, we found that to simulate NiO/ZnO heterojunction photodiode accurately, both the thermionic emission and band to band tunneling mechanisms must be considered when calculating transport across NiO/ZnO heterojunctions. Drift-diffusion descriptions of carrier mobility are incomplete at abrupt heterointerfaces such as NiO/ZnO contact. According to

Kanevce et al. (2009), modeling carrier transport using the drift-diffusion model does not take into account hopping transport or nonideal interfaces. Descriptions of the tunneling and thermionic emission across a heterojunction interface were suggested by Yang et al. (1993). Sultan et al. (2017) who developed a thermionic-field emission boundary condition. These models for thermionic emission and tunneling across a heterointerface have been incorporated into ATLAS. Ji et al. (2014) reported that the smaller bandgap results in the enhancement of the diffusion current in the depletion region. It is the opposite in wide bandgap, tunneling and thermionic emission have a significant effect in the interface, while the mismatch-induced defects can give rise to the energy levels in the bandgap, leading to the increasing Shockley-Read-Hall generation.

Direct recombination due to the states at the PN junction interface appears to be an important route of transport in many heterojunctions as well as NiO/ZnO because of the large mismatch which leads to the high density of interface states. These interface states have a pivotal role in determining the parameters of the current-voltage relationship (Karsthof et al., 2020). For a comprehensive interface traps description, we have considered the effect of interface traps parameters (trap density, electron capture cross-section, donor trap density, acceptor trap density). The results shows that the rise of interface trap density results in a high trap recombination rate which affects the current density under dark and illumination conditions and also optical properties. Other important findings were that the interface recombination itself and the transport to the interface affect the band bending of NiO/ZnO heterojunction and the performance of photodiode, This effect varies according to the type of traps donor or acceptor. The interface trap density variation has an impact on the band bending of the band diagram in NiO/ZnO heterojunction photodiode which is of importance when visualizing the possibility of carrier transport. Under high acceptor trap densities, tunneling rate and trap recombination rate are the important contributors for the current under the assumption of infinitely fast recombination at the interface. In the contrast, the high donor trap states result in a high recombination rate causing reducing photodetection of the device which means low responsivity and weak photocurrent.

In the third study, The magnetron-sputtered NiO, ZnO thin films and NiO/ZnO heterojunction are well described using XRD, SEM and UV-VIS spectroscopies. This work demonstrates that the NiO/ZnO heterojunction could play an important role in many applications, such as broadband photodetection devices, semi-transparent optoelectronics.

X-ray diffraction confirmed that ZnO has the hexagonal crystal symmetry with preferential growth in (002) direction. This confirms the formation of crystalline ZnO. The NiO film deposited by RF sputtering has a cubic structure with (111) orientation and small grain size. Recently, Potlog et al. (2019) claimed that the (111) preferred orientation of p-type NiO films seems to be under-stoichiometric. In this case, the presence of oxygen vacancies and exhibits a higher valence of Ni^{2+} and Ni^{3+} ions. Ac-

According to Chen et al. (2005) the (111) will be the preferred orientation under the low ratio of oxygen at high temperatures. The XRD results of NiO/ZnO heterojunction proved that, as NiO thin film is deposited on ZnO thin film, the intensity is changed which means the crystalline structure of the NiO is controlled by ZnO thin films. The SEM images of the surface morphologies where a smooth NiO film and dense ZnO film were formed. The same observation has been outlined for Patel et al. (2017). The optical properties of ZnO thin film possess an excellent transmittance profile and it confirms the UV absorption. Also, we reported the bandgap value of ZnO which was found equal to 3.23 eV. In the contrast, the NiO film shows a small bandgap of 3.1 eV and transmittance less than 45% due to the random structure of NiO film. Similar results have been obtained by Wang et al. (2017); Hwang et al. (2017). The low transmittance could be related to the defects in NiO. Potlog et al. (2019) reported that the origin of the observed high absorption in the visible region for this film is due to the charge-transfer process being more pronounced between Ni^{2+} and Ni^{3+} in the lattice due to the presence of oxygen vacancies which could result from the current deposition conditions, i.e., NiO grown in a vacuum atmosphere limited oxygen supply. According to Yang et al. (2020), the optical bandgap value of such film based on the morphology and structural changes through the film surface. The electron-hole recombination is generated due to the vacancies and defects. Gandhi et al. (2017) attributed that most metal oxide semiconductors are limited to the UV region. However, the properties of metal oxide semiconductors are tailored by introducing defects like bandgap energy which will narrow down to the visible region. They reported that the UV emission originated from excitonic recombination corresponding to near-band-edge transition of NiO, while deep-level-emission in the visible region due to various structural defects like oxygen vacancies and interstitial defects. The decrease in the transmittance in heterojunction as compared to the pure materials, from our work and some reports from other research groups, we know that the possible reason could be a contribution from the interfacial defects states which may exist due to the nickel intrinsic defects. It has been reported that the nickel intrinsic defects such as nickel vacancies V_{Ni} which tend to form Ni^{3+} and thereby absorb light from UV and visible range (Sultan et al., 2017; Karsthof et al., 2016). Therefore, in the first place, our findings suggest that NiO/ZnO heterojunction is suitable for designing broadband photodetectors which could be interesting for the development of broadband optoelectronic devices based on wide-bandgap materials of transparent photonics. In agreement with Patel et al. (2019b) results. The authors attributed that the Optical absorption through various processes, such as intermediate band, bound exciton, first-order exciton, free exciton, and band to band free charge generation in ZnO/NiO heterostructure. The ZnO/NiO photovoltaic response from the intermediate band optical transition ($h\nu < E_g$) and appropriate control of intermediate band states within the ZnO results in intermediate band photovoltaic and self-biased visible photodetection at high optical intensities (Patel et al., 2019a). This finding offers

appreciated information for the research community that the RF-sputtered NiO and ZnO thin films are beneficial for broadband photovoltaic applications. Further research will include the impact of oxygen flow on the structural properties of NiO and the performance of NiO/ZnO photodiode.

CONCLUSION

CONCLUSION

This research aimed to identify the most important factors that control the performance of NiO/ZnO photodiode. Based on the experimental methods for thin films and heterojunctions fabrication besides simulation tools for designing the photodetectors. In order to optimize the device performance proficiently and to provide a clear understanding of NiO/ZnO photodiode performance limits, we developed a comprehensive simulation that gives the correct description of the device operation. By performing several sets of simulations over main physical parameters extracted from experimental analysis. We have identified the importance of device structure optimization, the modification of metal oxide material properties, and the design and synthesis of defects and trap-free structure toward enhancing device performance.

Firstly, the study reports the growth of NiO and ZnO thin films prepared by spray pyrolysis technique with different quantities of solution 5, 10 and 15 ml. The thickness (d) of NiO and ZnO films increased by an increase in the quantity of solution. Although the same quantity of solution has been used for the deposition of both materials, the thickness of NiO is less than ZnO which seems to be due to the low growth rate due to the larger bandgap. The XRD analysis indicates that the relatively increasing thickness of films has a preferable growth orientation (111) and (002)/(011) for NiO and ZnO respectively. The transparency of NiO and ZnO films decreased. The NiO bandgap (E_g) decreased and ZnO increased slightly. The optical absorption coefficients (α), reflective indexes (n) and extinction coefficients (k) obtained from transmittance and reflectance. They indicate high quality for both metal oxide films. The extracted parameters d , α , n and k are used for the design and simulation of NiO/ZnO heterojunction photodiodes. The simulations prove the importance of choosing the optimum thickness and optical parameters to improve the work of the device. The simulation study of the effect of defects on the quality of the device indicates that NiO tail states increasing causes an increase of tunneling current. In the contrast, there are slight effects on tunneling at high ZnO tail defects. The deep defects density in ZnO or even NiO affects the photodetection characteristics that the responsivity and photocurrent decrease with the increasing of Gaussian states. Under illumination, the J-V characteristics and responsivity behavior are strongly dependent on the detailed material properties which can be expected to depend strongly flowing in such a situation on the recombination

rate associated with the defects states. We assumed that increasing the film thickness reduces the defects and reduced recombination through higher crystallinity which enhancing the photodetection.

Secondly and based on the previous results, we have fabricated the NiO/ZnO junction with a 15 ml quantity of solution conditions. Structural and morphological characterizations suggest cubic (111) and hexagonal (002)/(011) planes for NiO and ZnO respectively. Raman results confirm the purity of both NiO and ZnO thin films without secondary phases as indicated in XRD results. The surface of a heterostructure of NiO/ZnO is smooth and completely covered without any pinholes. Optical characterization shows that the decrease in the transmission in heterostructure as compared to the pure materials which be attributed to interface trap states. There is a lack of information on interface traps of NiO/ZnO heterojunction. Therefore, we performed a simulation to clarify the effects of heterojunction behavior and interface trap on the performance of NiO/ZnO photodiode. The band alignment of heterojunction is determined by band offsets We found that the conduction band offset between NiO and ZnO over 2 eV is known as a type-II heterojunction. In wide-bandgap heterojunctions, We found that the origin of the enhanced dark current has been attributed to both the band to band tunneling and thermionic emission in the interface, while the mismatch-induced defects can give rise to the energy levels in the bandgap, leading to the increase of the Shockley-Read-Hall generation. Under illumination, the J-V characteristics and responsivity behavior are strongly dependent on the interface properties. the J-V characteristic of the NiO/ZnO can be expected to depend strongly on density, electron capture cross section, acceptor or donor type of interface trap states.

As a third study, radiofrequency sputtering was used to deposit NiO, ZnO thin films to form NiO/ZnO heterojunction under vacuum (0 % oxygen flow condition). The structural, morphological and optical properties were investigated. The NiO film crystallized in the cubic phase and present (111) orientation results in small grain size. The deposited ZnO layer has a hexagonal structure with a growth orientation (002) plane. The same orientation peaks of both materials were observed in NiO/ZnO heterojunction. The surface morphology of NiO film consists of nanocrystalline file grains with uniform coverage of the substrate surface with randomly oriented morphology. SEM images confirm that the ZnO film is densely packed and pinhole-free. In contrast, NiO/ZnO heterojunction is smooth and completely covered without any pinholes. Optical characterization showed that NiO film is partially transparent. The low transparency and small bandgap are due to the presence of oxygen vacancies in the thin film. In contrast, ZnO film has large transparency in the visible region. the NiO/ZnO heterojunction had average transparency of over 25% in the visible range which makes

this heterojunction suitable for broadband photodetection applications. This study demonstrates that NiO/ZnO heterojunction could play an important role in many applications such as broadband photodetection (UV and Visible), and solar cells.

As perspective studies, we can be done the device characterization under the effect of various optical excitations. In addition, further research after suggesting the influence of the 25 % oxygen flow rate on the film behavior of RF sputtered NiO thin films.

BIBLIOGRAPHY

- (2013a). Physics and Radio-Electronics. "https://www.physics-and-radio-electronics.com/electronic-devices-and-circuits/semiconductor-diodes/photodiodesymboltypes.html.
- (2013b). rp-photonics. "https://www.rp-photonics.com/p_i_n_photodiodes.html.
- Akyuzlu, A. M., Dagdelen, F., Gultek, A., Hendi, A., and Yakuphanoglu, F. (2017). Electrical characterization of zno/nio pn junction prepared by the sol-gel method. *The European Physical Journal Plus*, 132(4):1–7.
- AL-Rashdi, K., Mohsin, M., Rabbani, G., and Farooqui, M. (2016). Metal oxide thin films: A mini review. *Journal of Advanced Scientific Research*, 7(1).
- Alnuaimi, A., Islam, K., and Nayfeh, A. (2013). Reduction of interface traps at the amorphous-silicon/crystalline-silicon interface by hydrogen and nitrogen annealing. *Solar Energy*, 98:236–240.
- Alzahrani, A. O. M., Abdel-wahab, M. S., Alayash, M., and Aida, M. (2018). Effect of zno layer thickness upon optoelectrical properties of nio/zno heterojunction prepared at room temperature. *Journal of Materials Science: Materials in Electronics*, 29(19):16317–16324.
- Anderson, AC, O., and DE (1982). Rf magnetron sputtering of zno for saw: Effects of magnetic field strength and configuration. In *1982 Ultrasonics Symposium*, pages 329–333. IEEE.
- Arfan, M., Shahid, T., Taj, M. K., et al. (2018). A facile composite-hydroxide-mediated route for preparation of composite fe³⁺-nio nanostructures. *Nanotechnology Letters*, 2.
- Armstrong, B. K., Cust, and E, A. (2017). Sun exposure and skin cancer, and the puzzle of cutaneous melanoma: A perspective on fears et al. mathematical models of age and ultraviolet effects on the incidence of skin cancer among whites in the united states. *american journal of epidemiology* 1977; 105: 420–427. *Cancer epidemiology*, 48:147–156.

- Atlas, D. S. (2005). Atlas user's manual. *Silvaco International Software, Santa Clara, CA, USA*.
- Barir, R., Benhaoua, B., Benhamida, S., Rahal, A., Sahraoui, T., and Gheriani, R. (2017). Effect of precursor concentration on structural optical and electrical properties of nio thin films prepared by spray pyrolysis. *Journal of Nanomaterials*, 2017.
- Benhamida, S., Benhaoua, B., Barir, R., Rahal, A., and Benhaoua, A. (2017). Effect of sprayed solution volume on structural and optical properties of nickel oxide thin films.
- Bhuiyan, MRA, R., and MK (2014). Synthesis and characterization of ni doped zno nanoparticles. *International Journal of Engineering and Manufacturing*, 4(1):10–17.
- Campbell, J. C. (2016). Recent advances in avalanche photodiodes. *Journal of Lightwave Technology*, 34(2):278–285.
- Chala, S., Sengouga, N., Yakuphanoglu, F., Rahmane, S., Bdirina, M., and Karteri, İ. (2018). Extraction of zno thin film parameters for modeling a zno/si solar cell. *Energy*, 164:871–880.
- Cheemadan, Saheer, K., and Santhosh, M. (2018). Effect of substrate temperature and oxygen partial pressure on rf sputtered nio thin films. *Materials Research Express*, 5(4):046401.
- Chen, H.-L., Lu, Y.-M., Wu, J.-Y., and Hwang, W.-S. (2005). Effects of substrate temperature and oxygen pressure on crystallographic orientations of sputtered nickel oxide films. *Materials transactions*, 46(11):2530–2535.
- Choudhary, S., Sarma, J., and Gangopadhyay, S. (2016). Growth and characterization of single phase cu₂o by thermal oxidation of thin copper films. In *AIP Conference Proceedings*, volume 1724, page 020116. AIP Publishing LLC.
- Chu, S. (2011). *Optoelectronics Devices Based on Zinc Oxide Thin Films and Nanostructures*. PhD thesis, UC Riverside.
- Debnath, R., Xie, T., Wen, B., Li, W., Ha, J. Y., Sullivan, N. F., Nguyen, N. V., and Motayed, A. (2015). A solution-processed high-efficiency p-nio/n-zno heterojunction photodetector. *Rsc Advances*, 5(19):14646–14652.
- Deng, R., Yao, B., Li, Y., Zhao, Y., Li, B., Shan, C., Zhang, Z., Zhao, D., Zhang, J., Shen, D., et al. (2009). X-ray photoelectron spectroscopy measurement of n-zno/p-nio heterostructure valence-band offset. *Applied physics letters*, 94(2):022108.

- Deveaud, B. (2007). The physics of semiconductor microcavities.
- Dolega, U. (1963). Theorie des pn-kontaktes zwischen halbleitern mit verschiedenen kristallgittern. *Zeitschrift für Naturforschung A*, 18(5):653–666.
- Echresh, A., Abbasi, M. A., Shoushtari, M. Z., Farbod, M., Nur, O., and Willander, M. (2014). Optimization and characterization of nio thin film and the influence of thickness on the electrical properties of n-zno nanorods/p-nio heterojunction. *Semiconductor Science and Technology*, 29(11).
- Echresh, A., Chey, C. O., Shoushtari, M. Z., Khranovskyy, V., Nur, O., and Willander, M. (2015). Uv photo-detector based on p-nio thin film/n-zno nanorods heterojunction prepared by a simple process. *Journal of alloys and compounds*, 632:165–171.
- Elseman, A., Ji, J., Dou, S., Huang, H., Cui, P., Wei, D., Li, M., et al. (2018). Novel hole transport layer of nickel oxide composite with carbon for high-performance perovskite solar cells. *Chinese Physics B*, 27(1):017305.
- Falcony, C., Aguilar-Frutis, M. A., and García-Hipólito, M. (2018). Spray pyrolysis technique; high-k dielectric films and luminescent materials: a review. *Micromachines*, 9(8):414.
- Fallahpour, A., Kienitz, S., and Lugli, P. (2017). Origin of dark current and detailed description of organic photodiode operation under different illumination intensities. *IEEE Transactions on Electron Devices*, 64(6):1–6.
- Farahmandjou, Majid, S., and Farzane (2015). Synthesis and characterization of α -fe₂o₃ nanoparticles by simple co-precipitation method. *Physical Chemistry Research*, 3(3):191–196.
- Felbier, P. (2015). All-inorganic heterostructure light-emitting devices based on zno nanoparticles.
- Firat, Y. and Peksoz, A. (2019). Efficiency enhancement of electrochromic performance in nio thin film via cu doping for energy-saving potential. *Electrochimica Acta*, 295:645–654.
- Fotis, K. (2012). Modeling and simulation of a dual-junction cigs solar cell using silvaco atlas. Technical report, NAVAL POSTGRADUATE SCHOOL MONTEREY CA.
- Galstyan, V., Poli, N., and Comini, E. (2019). Selective gas sensor based on metal oxide nanostructure. *Multidisciplinary Digital Publishing Institute Proceedings*, 14(1):21.
- Gandhi, Ashish Chhaganlal, W., and Yun, S. (2017). Strong deep-level-emission photoluminescence in nio nanoparticles. *Nanomaterials*, 7(8):231.

- Ghoughali, M. (2019). *Elaboration and characterization of nanostructuring NiO thin films for gas sensing applications*. PhD thesis, University of Mohamed Khider, BISKRA.
- Godse, P., Sakhare, R., Pawar, S., Chougule, M., Sen, S., Joshi, P., Patil, V. P., et al. (2011). Effect of annealing on structural, morphological, electrical and optical studies of nickel oxide thin films. *Journal of Surface Engineered Materials and Advanced Technology*, 1(02):35.
- Grundmann, M., Karsthof, R., and von Wenckstern, H. (2014). Interface recombination current in type ii heterostructure bipolar diodes. *ACS applied materials & interfaces*, 6(17):14785–14789.
- Gungor, Ebru, G., and Tayyar (2016). Optical properties of al: ZnO thin film deposited by different sol-gel techniques: Ultrasonic spray pyrolysis and dip-coating. *Journal of the Turkish Chemical Society Section A: Chemistry*, 3(3):175–184.
- Hao, S., Hetzl, M., Schuster, F., Danielewicz, K., Bergmaier, A., Dollinger, G., Sai, Q., Xia, C., Hoffmann, T., Wiesinger, M., et al. (2019). Growth and characterization of β -Ga₂O₃ thin films on different substrates. *Journal of Applied Physics*, 125(10):105701.
- Hasan, M. R., Xie, T., Barron, S. C., Liu, G., Nguyen, N. V., Motayed, A., Rao, M. V., and Debnath, R. (2015). Self-powered p-niO/n-zno heterojunction ultraviolet photodetectors fabricated on plastic substrates. *APL materials*, 3(10).
- Hassan, Alaa K, A., and M, G. (2020). Thin film niO/batio₃/zno heterojunction diode-based uvc photodetectors. *Superlattices and Microstructures*, 147:106690.
- Hu, Z., Chen, D., Yang, P., Yang, L., Qin, L., Huang, Y., and Zhao, X. (2018). Sol-gel-processed yttrium-doped niO as hole transport layer in inverted perovskite solar cells for enhanced performance. *Applied Surface Science*, 441:258–264.
- Huang, C.-C., Wang, F.-H., Wu, C.-C., Huang, H.-H., and Yang, C.-F. (2013a). Developing high-transmittance heterojunction diodes based on niO/tzo bilayer thin films. *Nanoscale Research Letters*, 8(1):1–8.
- Huang, C.-C., Wang, F.-H., Wu, C.-C., Huang, H.-H., and Yang, C.-F. (2013b). Developing high-transmittance heterojunction diodes based on niO/tzo bilayer thin films. *Nanoscale Research Letters*, 8(1):1–8.
- Huang, Y. (2018). *Modeling of Perovskite Solar Cells, III-V Optoelectronic Devices and Kelvin Probe Microscopy*. PhD thesis, INSA de Rennes.

- Husain, A. A., Hasan, W. Z. W., Shafie, S., Hamidon, M. N., and Pandey, S. S. (2018). A review of transparent solar photovoltaic technologies. *Renewable and sustainable energy reviews*, 94:779–791.
- Hwang, JD, H., and TH (2017). Effects of oxygen content on the structural, optical, and electrical properties of nio films fabricated by radio-frequency magnetron sputtering. *Materials Science in Semiconductor Processing*, 71:396–400.
- Hwang, Jun Dar, F., and Wei, C. (2019). High-performance organic/inorganic hybrid ultraviolet p-nio/pvk/n-zno heterojunction photodiodes with a poly (n-vinylcarbazole) insertion layer. *Journal of Materials Chemistry C*, 7(12):3529–3534.
- Hwang, Jun-Dar, L., and Wei-Ming (2018). Enhancing the photoresponse of p-nio/n-zno heterojunction photodiodes using post zno treatment. *IEEE Transactions on Nanotechnology*, 18:126–131.
- Inamdar, SI, R., and KY (2014). High-performance metal–semiconductor–metal uv photodetector based on spray deposited zno thin films. *Journal of alloys and compounds*, 595:55–59.
- Ji, X., Liu, B., Tang, H., Yang, X., Li, X., Gong, H., Shen, B., Han, P., and Yan, F. (2014). 2.6 μm mbe grown ingaas detectors with dark current of srh and tat. *AIP Advances*, 4(8):087135.
- Jilani, A., Abdel-Wahab, M. S., and Hammad, A. H. (2017). Advance deposition techniques for thin film and coating. *Modern Technologies for Creating the Thin-film Systems and Coatings*, 2:137–149.
- Jlassi, M., Sta, I., Hajji, M., Haoua, B. B., and Ezzaouia, H. (2014). Effect of annealing atmosphere on the electrical properties of nickel oxide/zinc oxide p–n junction grown by sol–gel technique. *Materials science in semiconductor processing*, 26:395–403.
- Jung, B. O., Kwon, Y. H., Seo, D. J., Lee, D. S., and Cho, H. K. (2013). Ultraviolet light emitting diode based on p-nio/n-zno nanowire heterojunction. *Journal of crystal growth*, 370:314–318.
- Kadam, A., Kim, T. G., Shin, D. S., Garadkar, K., and Park, J. (2017). Morphological evolution of cu doped zno for enhancement of photocatalytic activity. *Journal of Alloys and Compounds*, 710:102–113.
- Kanevce, Ana, M., and K, W. (2009). The role of amorphous silicon and tunneling in heterojunction with intrinsic thin layer (hit) solar cells. *Journal of Applied Physics*, 105(9):094507.

- Kappertz, O., Drese, R., Ngaruiya, J., and Wuttig, M. (2005). Reactive sputter deposition of zinc oxide: Employing resputtering effects to tailor film properties. *Thin Solid Films*, 484(1-2):64–67.
- Karsthof, R., Racke, P., Von Wenckstern, H., and Grundmann, M. (2016). Semi-transparent nio/zno uv photovoltaic cells. *physica status solidi (a)*, 213(1):30–37.
- Karsthof, R., Von Wenckstern, H., Zuniga-Perez, J., Deparis, C., and Grundmann, M. (2020). Nickel oxide-based heterostructures with large band offsets. *physica status solidi (b)*, 257(7):1900639.
- Khan, K. (2016). *NiO x Based Device Structures*. PhD thesis, University of Toledo.
- Khan, Z. R., Aziz, A., Khan, M. S., Khandaker, M. U., et al. (2017). Influence of zinc concentration on band gap and sub-band gap absorption on zno nanocrystalline thin films sol-gel grown. *Materials Science Poland*, 35.
- Klochko, N., Kopach, V., Tyukhov, I., Zhadan, D., Klepikova, K., Khrypunov, G., Petrushenko, S., Lyubov, V., Kirichenko, M., Dukarov, S., et al. (2018). Metal oxide heterojunction (nio/zno) prepared by low temperature solution growth for uv-photodetector and semi-transparent solar cell. *Solar Energy*, 164:149–159.
- Ko, Y. H., Nagaraju, G., and Yu, J. S. (2015). Fabrication and optimization of vertically aligned zno nanorod array-based uv photodetectors via selective hydrothermal synthesis. *Nanoscale research letters*, 10(1):1–7.
- Kumar, V., Kumar, S., Kumar, D., et al. (2017). Synthesis and characterization of cadmium doped zno nanoparticles. In *Recent Trends in Materials and Devices*, pages 211–215. Springer.
- Labeled, M., Sengouga, N., Kim, K. H., and Rim, Y. S. (2019). Numerical simulation on thickness dependency and bias stress test of ultrathin igzo thin-film transistors via a solution process. *physica status solidi (a)*, 216(7):1800987.
- Luo, C., Li, D., Wu, W., Zhang, Y., and Pan, C. (2014). Preparation of porous micro–nano-structure nio/zno heterojunction and its photocatalytic property. *RSC advances*, 4(6):3090–3095.
- Luo, Y., Yin, B., Zhang, H., Qiu, Y., Lei, J., Chang, Y., Zhao, Y., Ji, J., and Hu, L. (2016). Fabrication of p-nio/n-zno heterojunction devices for ultraviolet photodetectors via thermal oxidation and hydrothermal growth processes. *Journal of Materials Science: Materials in Electronics*, 27(3):2342–2348.

- Magyari-Köpe, Blanka, P., Seong Geon, L., Hyung-Dong, N., and Yoshio (2012). First principles calculations of oxygen vacancy-ordering effects in resistance change memory materials incorporating binary transition metal oxides. *Journal of Materials Science*, 47(21):7498–7514.
- Manual, A. U. (2008). Device simulation software. *Silvaco Int., Santa Clara, CA*.
- Meyer, B. K., Alves, I., Hofmann, D., Kriegseis, W., Forster, D., Bertram, F., Christen, J., Hoffmann, A., Straßburg, M., Dworzak, M., et al. (2004). Bound exciton and donor–acceptor pair recombinations in zno. *physica status solidi (b)*, 241(2):231–260.
- Mezher, S. J., Dawood, M. O., Beddai, A. A., and Mejbil, M. K. (2020). Nio nanostructure by rf sputtering for gas sensing applications. *Materials Technology*, 35(1):60–68.
- Mohammadi, Shima, Z., and Mahdi (2017). High performance n-zno/p-metal-oxides uv detector grown in low-temperature aqueous solution bath. *Thin Solid Films*, 626:173–177.
- Mrabet, C., Amor, M. B., Boukhachem, A., Amlouk, M., and Manoubi, T. (2016). Physical properties of la-doped nio sprayed thin films for optoelectronic and sensor applications. *Ceramics International*, 42(5):5963–5978.
- Muchuweni, E., Sathiaraj, T., and Nyakoty, H. (2017). Synthesis and characterization of zinc oxide thin films for optoelectronic applications. *Heliyon*, 3(4):e00285.
- Nagaraju, G., Ko, Y. H., and Yu, J. S. (2014). Facile fabrication and characterization of in 2 o 3 nanorods on carbon fibers. *Applied Science and Convergence Technology*, 23(4):187–191.
- Özgür, Ü., Alivov, Y. I., Liu, C., Teke, A., Reshchikov, M., Doğan, S., Avrutin, V., Cho, S.-J., and Morkoç, H. (2005). A comprehensive review of zno materials and devices. *Journal of applied physics*, 98(4):1–103.
- Pardakhty, A., Foroughi, M. M., and Ranjbar, M. (2017). Synthesis and characterization of cdo/gro nanolayer for in vivo imaging. *Nanomedicine Journal*, 4(3):191–196.
- Patel, Malkeshkumar, K., and Joondong (2017). Transparent nio/zno heterojunction for ultra-performing zero-bias ultraviolet photodetector on plastic substrate. *Journal of Alloys and Compounds*, 729:796–801.
- Patel, M., Ban, D.-K., Ray, A., and Kim, J. (2019a). Broadband photoresponse data of transparent all-oxide photovoltaics of zno/nio. *Data in brief*, 25:104095.

- Patel, M., Ban, D.-K., Ray, A., and Kim, J. (2019b). Transparent all-oxide photovoltaics and broadband high-speed energy-efficient optoelectronics. *Solar Energy Materials and Solar Cells*, 194:148–158.
- Patel, M., Kim, H.-S., and Kim, J. (2015). All transparent metal oxide ultraviolet photodetector. *Advanced Electronic Materials*, 1(11):1500232.
- Patil, G. E., Kajale, D. D., Gaikwad, V. B., and Jain, G. H. (2012). Preparation and characterization of SnO_2 nanoparticles by hydrothermal route. *International Nano Letters*, 2(1):1–5.
- Patnaik, P. (2003). *Handbook of inorganic chemicals*, volume 529. McGraw-Hill New York.
- Phokha, S., Pinitsoontorn, S., Chirawatkul, P., Poo-Arporn, Y., and Maensiri, S. (2012). Synthesis, characterization, and magnetic properties of monodisperse CeO_2 nanospheres prepared by pvp-assisted hydrothermal method. *Nanoscale research letters*, 7(1):1–13.
- Potlog, T., Ghimpu, L., Suman, V., Pantazi, A., and Enachescu, M. (2019). Influence of rf sputtering power and thickness on structural and optical properties of NiO thin films. *Materials Research Express*, 6(9):096440.
- Qiao, L., Wang, X., Sun, X., Li, X., Zheng, Y., and He, D. (2013). Single electrospun porous NiO-ZnO hybrid nanofibers as anode materials for advanced lithium-ion batteries. *Nanoscale*, 5(7):3037–3042.
- Quimby, R. S. (2006). *Photonics and lasers: an introduction*. John Wiley & Sons.
- Rani, B. J., Ravi, G., Yuvakkumar, R., Ravichandran, S., Ameen, F., and Al-Sabri, A. (2019). Efficient, highly stable Zn -doped NiO nanocluster electrocatalysts for electrochemical water splitting applications. *Journal of Sol-Gel Science and Technology*, 89(2):500–510.
- Rao, K. G., Ashok, C., Rao, K. V., Chakra, C. S., and Rajendar, V. (2014). Green synthesis of TiO_2 nanoparticles using hibiscus flower extract. In *Proceedings of the International Conference on Emerging Technologies in Mechanical Sciences*, pages 79–82.
- Reddy, Y., Reddy, A. M., Reddy, A. S., and Reddy, P. S. (2012a). Preparation and characterization of NiO thin films by dc reactive magnetron sputtering.
- Reddy, Y. A. K., Reddy, A. S., and Reddy, P. S. (2012b). Influence of oxygen partial pressure on the structural, optical and electrical properties of Cu -doped NiO thin films. *Physica Scripta*, 87(1):015801.

- Renker, D. (2006). Geiger-mode avalanche photodiodes, history, properties and problems. *Nuclear Instruments and Methods in Physics Research Section A: Accelerators, Spectrometers, Detectors and Associated Equipment*, 567(1):48–56.
- Samanta, Pijus Kanti, C., and Roy, P. (2011). Substrate effect on morphology and photoluminescence from zno monopods and bipods. *Frontiers of Optoelectronics in China*, 4(2):130–136.
- Sandana, V., Rogers, D., Teherani, F. H., Bove, P., Sedrine, N. B., Correia, M., Monteiro, T., McClintock, R., and Razeghi, M. (2015). Structural, optical, electrical and morphological study of transparent p-nio/n-zno heterojunctions grown by pld. In *Oxide-based Materials and Devices VI*, volume 9364, page 93641O. International Society for Optics and Photonics.
- Schuler, L. P. (2008). Properties and characterisation of sputtered zno.
- Sharma, S., Periasamy, C., and Chakrabarti, P. (2015). Thickness dependent study of rf sputtered zno thin films for optoelectronic device applications. *Electronic Materials Letters*, 11(6):1093–1101.
- Sharma, S., Sumathi, A., and Periasamy, C. (2017). Photodetection properties of zno/si heterojunction diode: A simulation study. *IETE Technical Review*, 34(1):83–90.
- Shen, Y., Yan, X., Bai, Z., Zheng, X., Sun, Y., Liu, Y., Lin, P., Chen, X., and Zhang, Y. (2015). A self-powered ultraviolet photodetector based on solution-processed p-nio/n-zno nanorod array heterojunction. *Rsc Advances*, 5(8):5976–5981.
- Shimada, R., Urban, B., Sharma, M., Singh, A., Avrutin, V., Morkoç, H., and Neogi, A. (2012). Energy transfer in zno-anthracene hybrid structure. *Optical Materials Express*, 2(5):526–533.
- Singh, R., Kumar, M., and Chandra, S. (2007). Growth and characterization of high resistivity c-axis oriented zno films on different substrates by rf magnetron sputtering for mems applications. *Journal of materials science*, 42(12):4675–4683.
- Soleimanpour, A. M. (2013). *Synthesis, fabrication and surface modification of nanocrystalline nickel oxide for electronic gas sensors*. The University of Toledo.
- Steirer, K. X., Ou, K. L., Armstrong, N. R., and Ratcliff, E. L. (2017). Critical interface states controlling rectification of ultrathin nio–zno p–n heterojunctions. *ACS applied materials & interfaces*, 9(36):31111–31118.
- Studenikin, S., Golego, N., and Cocivera, M. (1998). Optical and electrical properties of undoped zno films grown by spray pyrolysis of zinc nitrate solution. *Journal of Applied Physics*, 83(4):2104–2111.

- Sultan, M., Mumtaz, S., Ali, A., Khan, M. Y., and Iqbal, T. (2017). Band alignment and optical response of facile grown nio/zno nano-heterojunctions. *Superlattices and Microstructures*, 112:210–217.
- Sun, Z., Zhao, Y., He, M., Gu, L., Ma, C., Jin, K., Zhao, D., Luo, N., Zhang, Q., Wang, N., et al. (2016). Deterministic role of concentration surplus of cation vacancy over anion vacancy in bipolar memristive nio. *ACS applied materials & interfaces*, 8(18):11583–11591.
- Tsai, S.-Y., Hon, M.-H., and Lu, Y.-M. (2011). Fabrication of transparent p-nio/n-zno heterojunction devices for ultraviolet photodetectors. *Solid-State Electronics*, 63(1):37–41.
- Tyagi, M., Tomar, M., and Gupta, V. (2015). Trap assisted space charge conduction in p-nio/n-zno heterojunction diode. *Materials Research Bulletin*, 66:123–131.
- Ukoba, K., Eloka-Eboka, A., and Inambao, F. (2018). Review of nanostructured nio thin film deposition using the spray pyrolysis technique. *Renewable and Sustainable Energy Reviews*, 82:2900–2915.
- Ungula, J. (2015). *Growth and characterization of ZnO nanoparticles by sol-gel process*. PhD thesis, University of the Free State (Qwaqwa Campus).
- Vadgama, V., Vyas, R., Jogiya, B., and Joshi, M. (2017). Synthesis and characterization of cdo nano particles by the sol-gel method. In *AIP Conference Proceedings*, volume 1837, page 040016. AIP Publishing LLC.
- Vallisree, S., Thangavel, R., and Lenka, I. T. (2018). Modelling, simulation, optimization of si/zno and si/znmgo heterojunction solar cells. *Materials Research Express*, 6(2):025910.
- Wager, J. F. (2017). Real-and reciprocal-space attributes of band tail states. *AIP Advances*, 7(12):125321.
- Wang, M., Thimont, Y., Presmanes, L., Diao, X., and Barnabé, A. (2017). The effect of the oxygen ratio control of dc reactive magnetron sputtering on as-deposited non stoichiometric nio thin films. *Applied Surface Science*, 419:795–801.
- Wang, Y., Cheng, J., Yu, S., Alcocer, E. J., Shahid, M., Wang, Z., and Pan, W. (2016). Synergistic effect of n-decorated and mn 2+ doped zno nanofibers with enhanced photocatalytic activity. *Scientific reports*, 6(1):1–10.

- Wei, C., Xu, J., Shi, S., Bu, Y., Cao, R., Chen, J., Xiang, J., Zhang, X., and Li, L. (2020). The improved photoresponse properties of self-powered nio/zno heterojunction arrays uv photodetectors with designed tunable fermi level of zno. *Journal of Colloid and Interface Science*, 577:279–289.
- Wu, C.-H., Wang, S.-J., Lin, T.-H., Tu, Y.-C., Hung, C.-H., Liu, P.-Y., Chin, Y.-H., Uang, K.-M., and Chen, T.-M. (2015). Hydrothermal growth of single-crystalline zno thin films and theirs application on uv photodetectors. In *2015 International Conference on Solid State Devices and Materials (SSDM'15)*.
- Xu, Y. (2015). *Fabrication and characterization of photodiodes for silicon nanowire applications and backside illumination*. PhD thesis, University of Dayton.
- Yadav, A., Masumdar, E., Moholkar, A., Rajpure, K., and Bhosale, C. (2009). Effect of quantity of spraying solution on the properties of spray deposited fluorine doped tin oxide thin films. *Physica B: Condensed Matter*, 404(12-13):1874–1877.
- Yang, F., Fan, Y., Li, J., Fu, H., Xiang, G., Peng, W., Zhou, Y., Zhao, Y., Zhen, Z., Deng, G., et al. (2020). Effects of oxygen flow rates on the physical characteristics of magnetron sputtered single-phase polycrystalline cu₂o films. *Materials Research*, 23(6).
- Yang, K., East, J. R., and Haddad, G. I. (1993). Numerical modeling of abrupt heterojunctions using a thermionic-field emission boundary condition. *Solid-State Electronics*, 36(3):321–330.
- Yang, Z. (2009). *Doping in zinc oxide thin films*. University of California, Riverside.
- Yang, Z.-G., Zhu, L.-P., Guo, Y.-M., Tian, W., Ye, Z.-Z., and Zhao, B.-H. (2011). Valence-band offset of p-nio/n-zno heterojunction measured by x-ray photoelectron spectroscopy. *Physics Letters A*, 375(16):1760–1763.
- Yu, X., Marks, T. J., and Facchetti, A. (2016). Metal oxides for optoelectronic applications. *Nature materials*, 15(4):383–396.
- Zhang, J., Li, W., Hoyer, R., MacManus-Driscoll, J., Budde, M., Bierwagen, O., Wang, L., Du, Y., Wahila, M., Piper, L., et al. (2018). Electronic and transport properties of li-doped nio epitaxial thin films. *Journal of Materials Chemistry C*, 6(9):2275–2282.
- Zhang, W.-B., Yu, N., Yu, W.-Y., and Tang, B.-Y. (2008). Stability and magnetism of vacancy in nio: A gga+ u study. *The European Physical Journal B*, 64(2):153–158.

Zheng, Z., Zu, X., Zhang, Y., and Zhou, W. (2020). Rational design of type-ii nano-heterojunctions for nanoscale optoelectronics. *Materials Today Physics*, page 100262.

Zou, Y., Zhang, Y., Hu, Y., and Gu, H. (2018). Ultraviolet detectors based on wide bandgap semiconductor nanowire: A review. *Sensors*, 18(7):1–25.

APPENDIX A

PUBLICATIONS AND CONFERENCES

Publication:

Hakkoum, H., Tibermacine, T., Sengouga, N., Belahssen, O., Ghougali, M., Benhaya, A., Moumen, A. and Comini, E., 2020. Effect of the source solution quantity on optical characteristics of ZnO and NiO thin films grown by spray pyrolysis for the design NiO/ZnO photodetectors. *Optical Materials*, 108, p.110434. <https://doi.org/10.1016/j.optmat.2020.110434>.

Conference:

American Algerian Foundation (AAF) Summer University. July 2019- August 2020- August 2021.

5th international conference on energy, materials, applied energetics and pollution (icemaep'2019), 22-24 October 2019, Constantine, Algeria.

International Conference on Advanced Materials Science and engineering and high tech device applications (ICMATSE) 2020October 02-04, 2020, Ankara, Turkey.